Report for the ILC Detector R & D Panel Instrumentation of the Very Forward Region

The Forward Calorimetry Collaboration (FCAL)

May 20, 2007

Spokesman of the Fcal Collaboration: Wolfgang Lohmann, wlo@ifh.de

Editors:
Ch. Grah, M. Idzik, R. Ingbir, W. Lange, A. Levy, K. Mönig, W.M. Morse,
U. Nauenberg, B. Pawlik, C. Rimbault, W. Wierba, L. Zawiejski, M. Zeller

See next page for list of authors

- Belarus

  K. Afanaciev[a], V. Drugakov, I. Emeliantchik, A. Ignatenko[b], A. Litomin, N. Shumeiko, A. Solin, P. Starovoitov
  NC PHEP, Minsk

- Czech Republic

  P. Mikes, J. Popule, L. Tomasek, M. Tomasek, P. Ruzicka, V. Vrba
  Institute of Physics, Academy of Science, Prague[g,g1]

- France

  P. Bambade, C. Rimbault
  Laboratoire de l Accélérateur Linéaire, Orsay[h]

- Germany

  C. Grah, U. Harder, H. Henschel, W. Lange, W. Lohmann, K. Mönig, M. Ohlerich, R. Schmidt
  Deutsches Elektronensynchrotron Desy, Zeuthen[g,h]

- Great Britain/United Kingdom

  G. Blair, J. Carter
  Centre for Particle Physics, Royal Holloway University of London[h]

- Israel

  H. Abramowicz, R. Ingbir, S. Kananov, A. Levy, I. Sadeh, O. Smith, A. Stern
  School of Physics & Astronomy, Tel Aviv University[d,g]

- Poland

  W. Dabrowski, M. Idzik, D. Kisielewska, S. Koperny, Sz. Kulis, J. Lukasik, J. Pieron, K. Swientek, L. Suszycki, P. Wiacek
  Faculty of Physics & Applied Computer Science, AGH University of Science and Technology, Cracow[e,g]

  J. Blocki, W. Daniluk, E. Kielar, A. Moszczynski, K. Oliwa, B. Pawlik, W. Wierba, L. Zawiejski
  Institute of Nuclear Physics, Polish Academy of Sciences, Cracow[e,g]

- Russia

  S. Erine, A. Rybine
  Institute of High Energy Physics, Protvino

- Serbia

  I. Bozovic-Jelisavcic, M. Mudrinic, I. Smiljanic, M. Pandurovic
  VINCA Institute of Nuclear Science, Belgrade[f]

- USA

  S. Chen, T. Dunn, J. Gill, M. Persson-Gulda, U. Nauenberg, G. Oleinik, J. Proulx, P. Steinbrecher, J. Zhang[k]
  Physics Department, University of Colorado, Boulder[i]

  W.M. Morse, B. Parker
  Brookhaven National Laboratory, Upton, New York[i]

  G. Atoian, V. Issakov, A. Poblaguev, M. Zeller
  Yale University, New Haven, Connecticut[i]

  A. Abusleme, M. Breidenbach, D. Freytag, G. Haller
  SLAC/Stanford University, Palo Alto, California[i]

- International Laboratory

  G. Chelkov, A. Elagin, Z. Krumstein, I. Minashvili, A. Olshevski, A. Sapronov[a]
  Joint Institute of Nuclear Research, Dubna, Russia[c]

Abstract

The current status of the research work of the Forward Calorimetry Collaboration (FCAL) is described. Three sub-detectors are addressed: BeamCal, LumiCal and GamCal. BeamCal is planned to be positioned just adjacent to the beam-pipe and ensures detector hermeticity to polar angles above about 5 mrad. Of particular importance is the detection of high energy electrons at low polar angles. In addition, it assists beam-tuning to maximum luminosity by detecting incoherent pairs from beamstrahlung. LumiCal, at larger polar angles, serves for the precise measurement of the luminosity and improves the detector hermeticity as well. GamCal is positioned about 180 m downstream and delivers information on the energy, the energy spectrum and the intensity of beamstrahlung photons, improving substantially the luminosity optimization.

For BeamCal and LumiCal, detailed simulations are done to optimize the design of these detectors. Both are planned as compact and highly segmented sandwich calorimeters. Tungsten disks of one X_0 thickness are interspersed with sensor planes. For LumiCal, silicon pad sensors will be used. BeamCal will work in a harsh radiation environment, hence radiation hard sensors are needed. Since the occupancy of LumiCal is relatively large and BeamCal must be readout after each bunch crossing, a fast readout electronics is necessary.

We present the motivation for the high accuracy requirement on the luminosity measurement, better then 10^{-3}, and study systematic effects identified to have impact on the accuracy goal. Monte Carlo simulations with realistic assumptions on several sensor parameters show the feasibility of a high precision luminosity measurement if certain requirements are fulfilled. These requirements, like the accuracy of the sensor position, the calorimeter position, and the dynamic range of the readout electronics are quantified.

Two concepts for a mechanical structure of LumiCal are under consideration. Engineering studies are done to estimate the impact of gravity on the structures. First exercises with a laser based position monitoring system for LumiCal show that the required position accuracy of a few μm can be reached.

BeamCal simulations have shown a strong impact of the crossing angle, of the detector magnetic field and of the accelerator parameter settings on the amount and the distribution of the depositions caused by beamstrahlung e^+e^- pairs. The performance to detect high energy electrons at small polar angles depends significantly on these settings. An optimization of the detector segmentation is done to reach the highest electron detection efficiency.

For the GamCal system a conceptual design is presented. First simulations and background estimates support the feasibility of the device.

Sensor studies on the linearity and radiation hardness are done for CVD diamond in test-beams at CERN and S-DALINAC. Good linearity of the response was found over a signal range of 10^6. CVD diamond sensors withstand doses up to 7 MGy, however the performance changes as a function of the dose and several other effects are not yet understood. Other materials like GaAs, radiation-hard silicon or SiC are potential alternatives, and systematic studies are just prepared.

The development of front-end chips for the readout of BeamCal and LumiCal is started and first prototypes are expected this summer.

Contents

1 Introduction

The purpose of the FCAL Collaboration is to develop the design for the instrumentation of the very forward region of the future detector at the International Linear Collider (ILC) and to prove the feasibility of detector technologies appropriate for this instrumentation [1]. Presently the following sub-systems are considered, in decreasing order of polar angle: the luminosity detector (LumiCal) for precise measurement of the Bhabha event rate; the beam calorimeter (BeamCal) and the beamstrahlung photons monitor (GamCal) for providing a fast feed-back in tuning the luminosity. BeamCal in addition supports the determination of beam parameters. Both LumiCal and BeamCal extend the angular coverage of the electromagnetic calorimeter to small polar angles. The requirement for LumiCal is to enable a measurement of the integrated luminosity with a relative precision of about 10^{-4}. The design is based on a tungsten/silicon sandwich calorimeter.

The sensor planes are subdivided into pads. The use of Bhabha scattering as the gauge process is motivated by the fact that the cross-section is large and dominated by electromagnetic processes and thus the cross-section can be calculated with very high precision.

The purpose of the BeamCal is to efficiently detect high energy electrons and photons produced e.g. in low transverse momentum QED processes such as Bhabha scattering and photon-photon events. The latter is important in order to suppress this dominant background in many searches for new particles predicted in scenarios for physics beyond the Standard Model. In the polar angle range covered by the BeamCal, typically 5 to 45 mrad, high energy electrons must be detected on top of wider spread depositions of low energy e^+e^- pairs originating from beamstrahlung photon conversions. The measurement of the total energy deposited by these pairs, bunch by bunch, can be used to monitor the variation in luminosity and provide a fast feedback to the beam delivery system. Moreover, the analysis of the shape of the energy flow can be used to extract the parameters of the colliding beams. This information can be further used to optimize the machine operation.

GamCal is used to analyze beamstrahlung photons. It will be positioned at a distance of about 180 m from the interaction point (IP). It will be sensitive to the energy of the beamstrahlung photon and to the size of the beamstrahlung photon cone, which in turn is sensitive to the beam parameters.

We are working with the Large Detector Concept (LDC) [2], which is a successor of the detector presented in the Tesla-TDR [3] and with the Silicon Detector Design study (SiD) [4]. The layout for a 14 mrad beam crossing angle is presented in Fig. 1 for the example of the LDC. The location of the LumiCal and BeamCal is of critical importance for the background in the main detector. BeamCal acts as a mask in front of the final quadrupole magnets reducing backscattering from pairs. The aperture of LumiCal is such that only a small amount of backscattered particles from the BeamCal reaches the inner detector while it is large enough to let pass the pairs from beamstrahlung. Note that for different beam crossing angles and different magnetic field configurations, the energy distributions of the pairs changes and the amount of backscattered particles is considerably different. The latter has implications on the optimal location of the very forward calorimeters and their polar angle coverage.

In the following, we report on the R&D efforts within the FCAL collaboration.
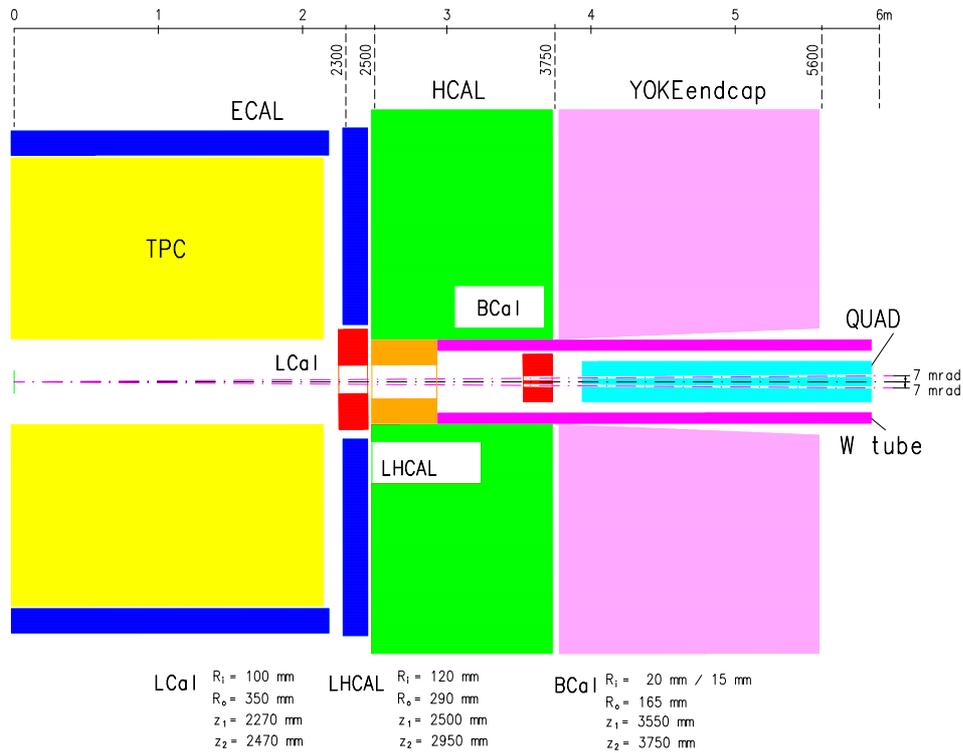
Figure 1: The layout of the forward region of the LDC detector, as considered in the presented studies. The angular coverage of LumiCal and BeamCal, as well as the distance from the IP are given in the figure. LCal is the LumiCal, BCal is the BeamCal, TPC is the Time Projection Chamber, ECAL is the Electromagnetic Calorimeter, HCAL is the Hadronic Calorimeter, QUAD is the final quadrupole of the beam delivery system and LHCAL is a possible low angle hadronic calorimeter, which is not part of this report.

2 The Luminosity Monitor - LumiCal

2.1 Motivation for Precision Luminosity Measurement

To measure the cross-section, σ, of a certain process we count the events, N, registered in the detector, and obtain the cross section using the corresponding integrated luminosity, $\mathcal{L}$, $\sigma = N/\mathcal{L}$. Neglecting other systematic uncertainties, the required precision on the luminosity measurement is given by the statistics of the highest cross-section processes we want to measure. At $\sqrt{s} = 340$ GeV the cross-section for $e^+e^- \to W^+W^-$ is about 10 pb and the one for fermion pairs, $e^+e^- \to q\bar{q}$, is about 5 pb, both scaling with $1/s$. In both processes one thus expects event samples of $\mathcal{O}(10^6)$ events in a few years of running, which would require a luminosity precision of $\Delta\mathcal{L}/\mathcal{L}$ of better than 10^{-3}.

W-pair production is given by neutrino t-channel exchange and Z or γ s-channel exchange. The t-channel part is strongly peaked in the forward region and dominates the total cross-section. If the $We\nu$ coupling is taken from the Standard Model, all information on anomalous gauge couplings can thus be obtained from a fit to the W angular distribution (combined with some decay angles) so that no luminosity measurement is needed. However, if there is a reason to re-measure the $We\nu$ coupling at the ILC, a precise luminosity determination is necessary.

The situation is completely different for fermion pair production. For $f \neq e$, only the interesting s-channel diagrams are present and the normalization has to be taken from an external luminosity measurement. As an example, Fig. 2 shows the expected exclusion limits on Z' bosons obtained from the two-fermion cross sections for different assumptions on the systematic uncertainties [5]. For the η model, only the cross-section error is important while for the other models the errors on the luminosity and the polarization are relevant. Similar requirements hold for the search for contact interactions or other indirect signatures for physics beyond the Standard Model.

In the GigaZ mode, more than 10^9 hadronic Z decays are expected which would in principle require a luminosity precision around 10^{-5}. However there are other systematic uncertainties, like the selection efficiency for hadronic events and the modification of the cross-section on top of the Breit-Wigner resonance due to the beam energy spread, that seem hard to get under control at this level. Hence a luminosity precision of $\Delta\mathcal{L}/\mathcal{L} \sim 10^{-4}$ seems sufficient. The goal of the GigaZ run is a test of the radiative corrections to the Z-fermion couplings with extremely high precision. In general these radiative corrections can be parameterized in terms of three parameters, e.g. $\varepsilon_{1,2,3}$ [6]. Figure 3 shows the expected precision on $\varepsilon_{1,3}$ under different assumptions [7]. These two parameters can be obtained from the Z-observables alone while ε_2 needs in addition a measurement of the W-mass. The narrow axis of the ellipse is given by the measurement of the effective weak mixing angle which is obtained from asymmetry measurements, and does not require an absolute luminosity measurement. For a limit on the Higgs boson mass, within the Standard Model, this measurement is sufficient. In most extensions of the Standard Model, ε_1 and ε_3 can vary in a wide range while ε_2 stays at its Standard Model value. The large axis of the ellipse can be constrained by a precise measurement of the W-mass, so that also in this case no absolute luminosity measurement is required. In the most general case, where also
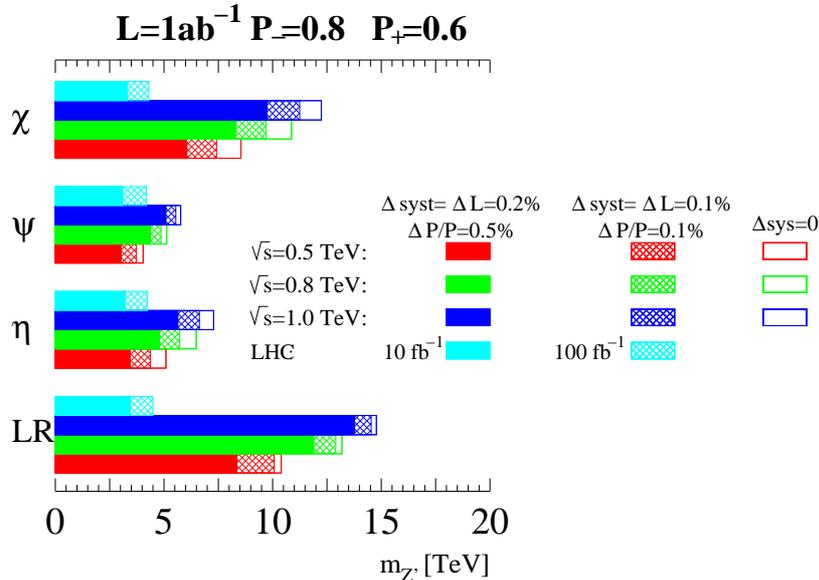
Figure 2: Sensitivity to different Z' models estimated for the ILC, for several centre-of-mass energies as denoted in the figure, and for the LHC.

ε_2 is allowed to deviate from its Standard Model value, the large axis is determined by the partial widths of the Z for which cross-section measurements are an essential input.

GigaZ is especially interesting when no direct evidence for physics beyond the Standard Model is found. In this case the structure of radiative corrections should be tested without artificial constraints so that the high precision on the luminosity is definitely required.

2.2 Theoretical Precision of the Bhabha Monte Carlo Generators

For the determination of the luminosity the precise calculation of the Bhabha cross section at small polar angles is needed. For the final LEP results, the theoretical cross-section uncertainty was the largest systematic uncertainty of the luminosity measurement [8]. Theorists are working currently in several laboratories to improve the accuracy of higher order corrections to the Bhabha cross-section [9, 10, 11, 12, 13]. In a recent report [14], the current theoretical uncertainty was estimated to be 5.3×10^{-4} on the Z resonance, with the prospect to reduce this uncertainty to 2×10^{-4}, matching the need of GigaZ. At higher energies, the contributions of higher order corrections increase by the order of 10%, however, with sufficient effort, an uncertainty similar to the one on the Z-resonance should be feasible.

2.3 Background to Bhabha Scattering

Four-fermion NC processes $e^- e^+ \rightarrow e^- e^+ f^- f^+$ (f=l,μ,q) are considered to be the main source of physics background for the luminosity measurement. They are dominated by the multiperipheral processes (2-photon exchange). The contributing Feynman diagrams are
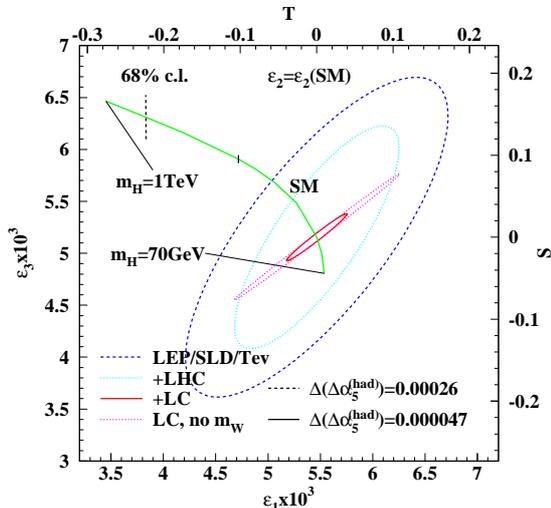
Figure 3: Presently known precision for $\varepsilon_{1,3}$, expected after the LHC and after the ILC measurements. All curves, apart from the one denoted "LC, no m_W", assume that ε_2 is equal to its SM value, which is true in most, but not all, extensions of the Standard Model.

given in Fig. 4. Outgoing e^+e^- pairs are emitted along the beam pipe carrying most of the energy, while low-energetic l^+l^- pairs are distributed over a wider polar angle range (Fig. 5). Due to the steep polar angle distribution of the produced particles, most of the energy is deposited in the beam calorimeter while low-energetic particles are mainly deposited in the luminosity calorimeter.

Both this study and an independent study [15] of two-photon processes ($2\gamma \rightarrow e^-e^+$), using the Vermasseren generator [16], found an occupancy in the luminosity calorimeter acceptance region of 10^{-3} particles per bunch crossing.

To simulate physics background, a sample of 10^6 four-lepton events $e^-e^+ \rightarrow e^-e^+l^-l^+$ (l=e,μ) and 10^5 corresponding hadronic events $e^-e^+ \rightarrow e^-e^+q^-q^+$ (q=u,d,c,s,b) have been generated with WHIZARD [17], with a total cross section of (1.68 ± 0.03) nb, assuming event generation through contributions of all neutral current tree-level processes. The simulation is performed in the full polar angle range, assuming that the invariant mass of the outgoing lepton pair is greater than 1 GeV and momentum transfer of the exchanged photon is also greater then 1 GeV.

The energy distributions of the hadronic and the leptonic background in the luminosity calorimeter are given in Fig. 6. In terms of the detector occupancy, physics background contributes approximately 10 times less then the signal. The maximal occupancy of a sensor plane is given per train, for signal and background, in Fig. 7. Though the rate of the background is about 10% of the signal, the kinematical characteristics of Bhabha events (colinearity, coplanarity, energies of the showers) allow isolation cuts to be applied.

Discrimination of signal from background is based on a set of cuts established to opti-
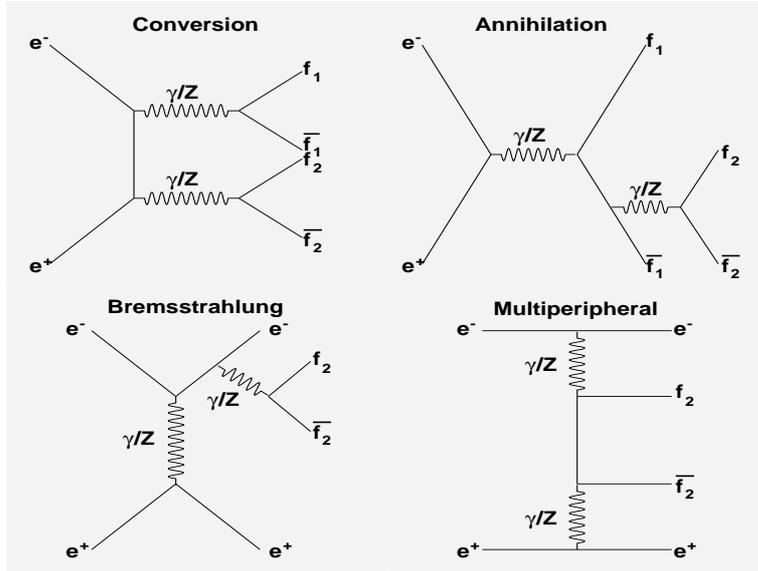
Figure 4: Feynman diagrams contributing to neutral current four-lepton production. The dominant fraction is described by the multi-peripheral diagram (bottom right).
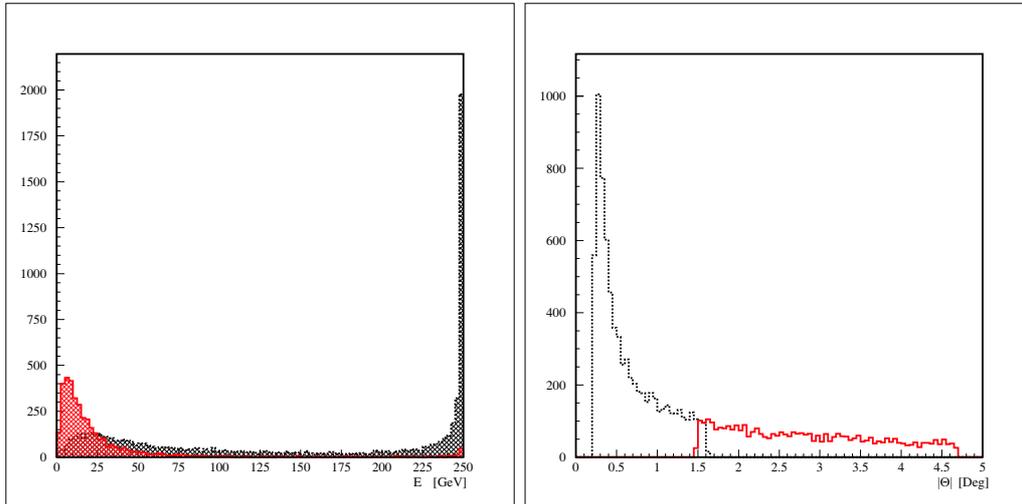
Figure 5: Energy and polar angle distributions of generated particles in the beam calorimeter (dashed line) and luminosity calorimeter (solid line) acceptance region.
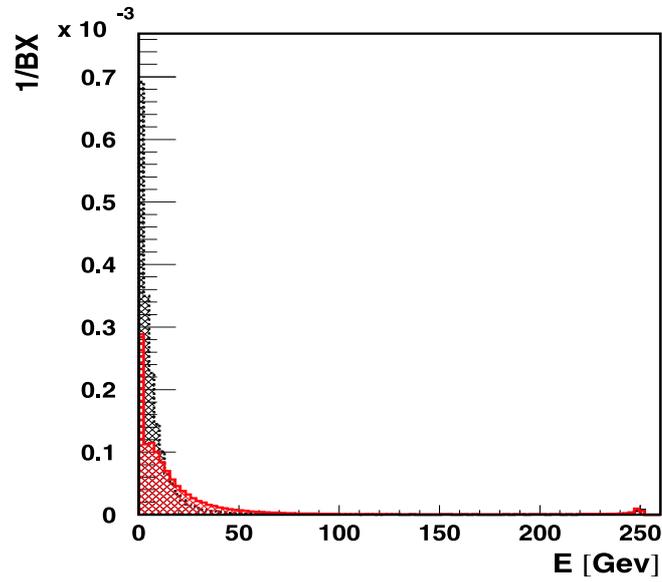
Figure 6: Energy distributions for leptonic (solid line) and hadronic (dashed line) background in the luminosty calorimeter.
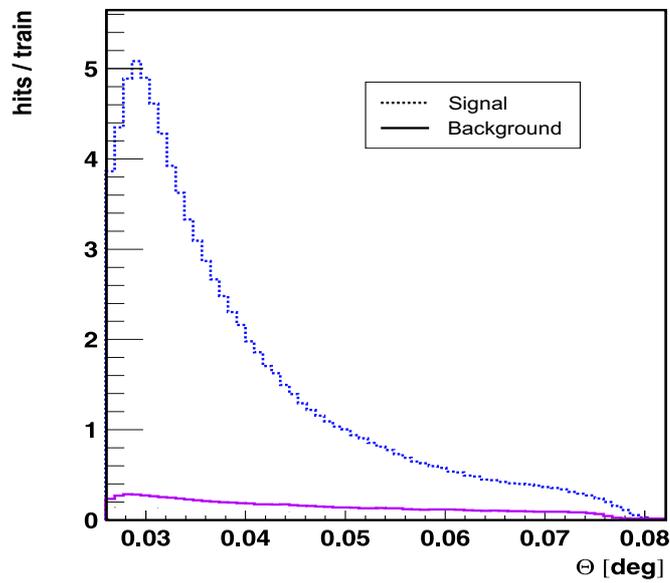
Figure 7: Occupancy in the luminosity calorimeter for signal (dashed line) and background (solid line).

7

	Bhabha selection efficiency		Leptonic background rejection efficiency	Hadronic background rejection efficiency
1. $|\Delta\theta| < 0.06\,\mathrm{deg}$	81.87 %		95.20 %	95.27 %
2. $|\Delta\Phi| < 5\,\mathrm{deg}$	97.96 %		89.53 %	90.42 %
3. $E_{bal} < 0.1E_{min}$	90.61 %		94.58 %	95.45 %
4. $E_{rel} > 0.75$	99.08 %		88.73 %	95.96 %
B/S(1,2,3)	**1.3 10^{-4}**	80.60 %	99.38 %	99.78 %

Table 1: Selection and rejection efficiency for signal and background.

mize the detector performance [18]:

- Acolinearity cut $|\Delta\theta| < 0.06\,\mathrm{deg}$;
- Acoplanarity cut $|\Delta\Phi| < 5\,\mathrm{deg}$;
- Energy balance cut $E_{bal} = |E_R - E_L| < 0.1E_{min}$,

$E_{min} = \min(E_R, E_L)$ and E_R, E_L being the total energy deposited on the right (front) and left side (back) of the luminosity calorimeter, respectively. All isolation cuts are applied assuming ideal reconstruction, since later it will be shown that detector resolution does not affect the suppression of background, and a 100 % reconstruction efficiency is assumed. It has been shown that Bhabha electrons can be detected very efficiently even in the regions with high beamstrahlung background [19].

Background rejection efficiency and signal efficiency are given in Table 1, for the proposed set of cuts. As illustrated in the Table, physics background is to be reduced to the level of 10^{-4}, with a loss of signal efficiency of about 20% with the set of cuts 1,2 and 3. The distribution of hits projected on the front plate of the luminosity calorimeter is given in Fig. 8, before and after cuts, for events that have at least a particle at each side of the luminosity calorimeter.

In order to maintain the background to signal ratio at the required level of 10^{-4}, the minimal required detector resolution in θ is about $1\,\mathrm{mrad}$. However from the detector performance study [20, 18] we obtain $0.03\,\mathrm{mrad}$, hence this quantity is uncritical. We can conclude that with the set of isolation cuts applied, the signal to background ratio is practically insensitive to detector resolution effects.

Signal and background will be additionally affected by the beam-beam interaction effects. They will modify both initial state, through beamstrahlung, and the final state, through electromagnetic deflection, resulting in a total suppression of the Bhabha cross-section of the order of 4.4 % [21]. In order to minimize the effect of beam-beam interaction, the following set of cuts can be applied [21]:

- $E_{rel} > 0.8$
- $30 < |\theta| < 75\,\mathrm{mrad}$,

where the second cut has been subsequently applied to the forward and the backward side of the detector, allowing to accept Bhabha events slightly asymmetric due to the beamstrahlung.
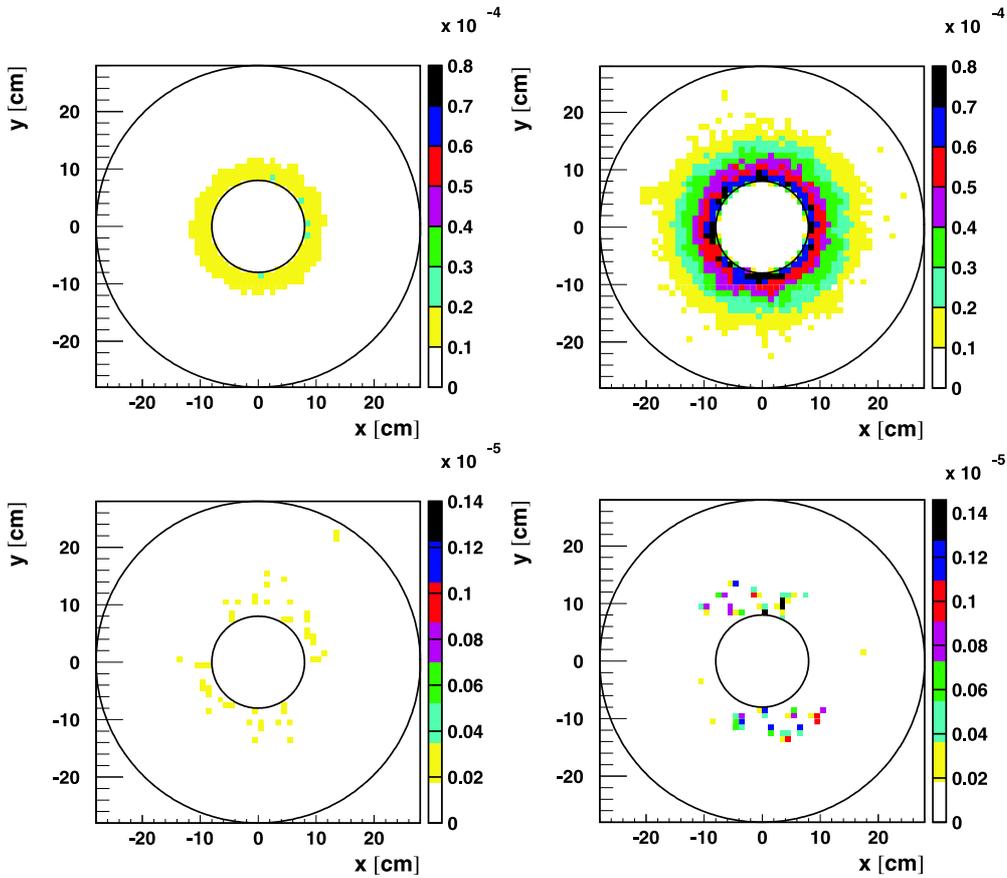
Figure 8: Projection of hits at the front plate of the luminosity calorimeter for leptonic (left) and hadronic (right) background, before (top) and after (bottom) applying the set of isolation cuts (1,2,3).

As shown in Table 2, these cuts are cutting-off more than one third of the signal, with the presence of background ten times larger than required. In principal, an annual Bhabha statistics of 10^9 events should allow a flexibility for 30% loss of the signal to still keep the statistical error of the order of 10^{-4}.

It has been shown that, due to the characteristic topology, Bhabha processes can be separated from physics background at the level of 10^{-4}. Physics background would occupy the read-out system approximately ten times less than the signal. In order to reach the required separation of signal from the physics background, there are no particular requirements on luminosity calorimeter performances. This study has been performed under certain assumptions that, however, should not significantly influence the validity of its conclusion. These are idealizations like a stand-alone luminosity calorimeter simulation and assumption on 100% reconstruction efficiency.

9

	Bhabha selection efficiency	Leptonic background rejection efficiency	Hadronic background rejection efficiency
1. $30 < |\theta| < 75\,\mathrm{mrad}$	64.99 %	42.11 %	41.95 %
2. $E_{rel} > 0.8$	98.50 %	90.74 %	96.57 %
(1,2)	64.33.61 %	93.69 %	97.48 %
B/S	**1.87 10^{-3}**		

Table 2: Selection and rejection efficiency for signal and background for cuts optimized for beam-beam interactions.

2.4 Impact of Beam-beam Effects on Precision Luminosity Measurements at the ILC

Besides theoretical uncertainties on the cross section of the Bhabha process and different experimental errors when identifying Bhabha events in the LumiCal, the very strong beam-beam space charge effects which characterize the ILC e^+e^- collisions can lead to large biases in the counting rate and thus on the luminosity measurement. These biases have been studied for the first time recently [22], using a sample of Bhabha events produced with BHLUMI 4.04 [23] in an angular range of $25 < \theta < 90\mathrm{mrad}$ at 500 GeV center-of-mass energy. The four-momenta of the two charged final state particles of a generated event are then read into the beam-beam interaction simulation GUINEA-PIG [24] and associated to one of the e^+e^- interactions occurring during the simulated bunch collision. GUINEA-PIG computes the subsequent electromagnetic transport through the remaining part of the colliding bunch and one obtains the distribution of the resulting deflections. Nominal ILC beam parameters [25] are used for the beam-beam simulation.

Prior to the hard Bhabha scattering, the interacting particles are likely to have been deflected by the space charge of the opposite bunch and their energies reduced due to the emission of beamstrahlung. To take into account the cross section dependence with s, the probability used to produce Bhabha scattering events during the beam-beam collision is rescaled by s/s', where s' is the effective centre-of-mass energy. The four-vectors of the Bhabha event particles are also rescaled by $\sqrt{s'/s}$, to satisfy energy and momentum conservation, as well as boosted from the centre-of-mass system of the two interacting particles to the laboratory frame. Finally the coordinate system is rotated to take into account the deflection angles of the interaction particles in the initial state.

The beamstrahlung emissions often occur asymmetrically, with either the electron or the positron loosing most of the energy. Hence the acolinearity of the final state can be significantly enhanced. This is illustrated in Fig. 9, where the distributions of the polar angles of the two final state particles are shown in the range of the LumiCal acceptance, both for the initial sample generated with BHLUMI and after the boosting procedure. As can be seen, this enhances the acolinearity such that many of the events, initially within an initial angular acceptance of 30-75 mrad, migrate outside, hence significantly reducing the counting rate.

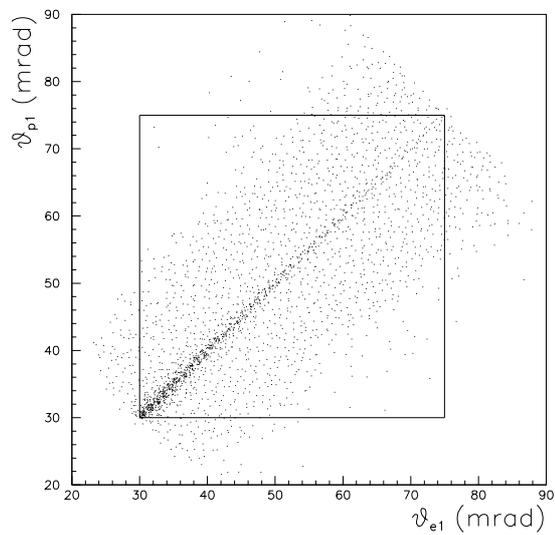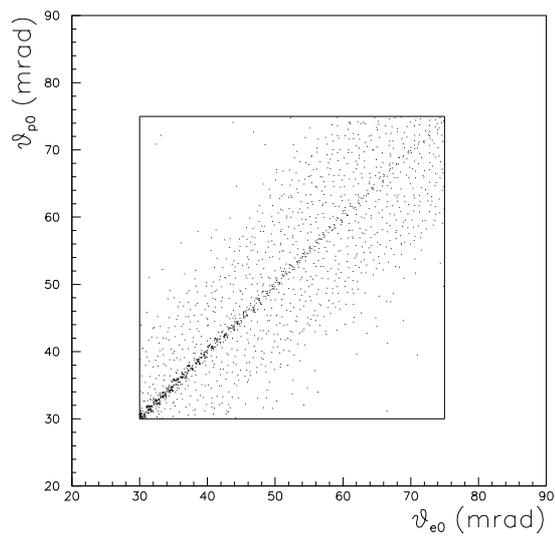The final state particles scattered in the acceptance of the LumiCal following a Bhabha

Figure 9: Polar angles of the final state positrons versus the electrons without including any beam-beam effects (top) and after accounting for beamstrahlung radiation of the interacting particles in the initial state (bottom).

interaction can typically cross a significant part of the opposite bunch. They can thus be focused by the electromagnetic field from the corresponding space charge. The resulting changes in scattering angles are displayed in Fig. 10, where the differences between the initial polar angles before including the electromagnetic deflection, θ_1, and the final ones including it, θ_2, are shown as a function of θ_1. The typical magnitudes of the induced electromagnetic deflections are a few 10^{-2} mrad, with the largest values at the lower edge of the LumiCal acceptance. Small energy losses due to radiation are also found.
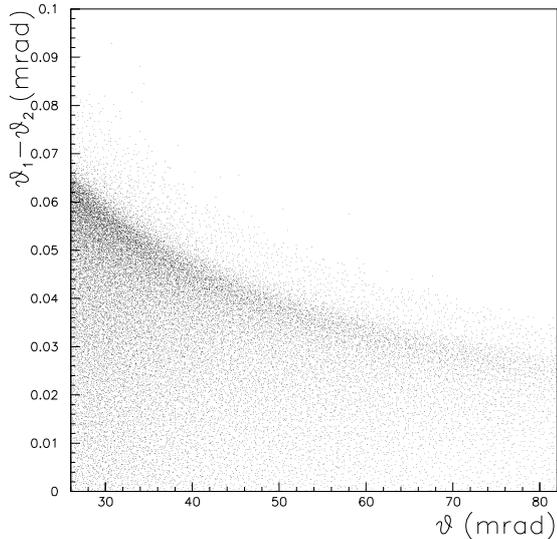

Figure 10: Change in Bhabha scattering final state polar angle due to the deflection induced by the space charge of the opposite bunch, as a function of the polar angle at production.

Both the beamstrahlung radiation and electromagnetic deflection effects lead to a suppression of the Bhabha counting rate in the defined experimental acceptance in comparison to the theoretically predicted one. This Bhabha Suppression Effect (BHSE) can be expressed as

$$BHSE = \frac{N_{final} - N_{init}}{N_{init}} \ , \tag{1}$$

where N_{init} and N_{final} are the numbers of Bhabha events selected within the specified cuts before and after including the different transformations to take into account effects from the beam space charge, respectively. Beamstrahlung radiation emitted prior to the hard Bhabha scattering enhances the acolinearity between the two final state charged particles. For this reason, assymetrical angular cuts, first introduced by the LEP experiments [26, 27, 28, 29] and later adapted for ILC [30], are advantageous to minimize the BHSE and the resulting biases. In the same line of thought, assymetrical cuts are also applied for the energies. As it is illustrated in Fig. 11, one can see that it is more natural to choose a global energy cut based on the sum of the final state energies rather than individual ones. The

following asymmetrical selection cuts for the angles and energies of the final state particles were applied:

$$30 < \theta_{+/-} < 75 \text{mrad} \quad \text{and} \quad 26.2 < \theta_{-/+} < 82 \text{mrad} \;, \tag{2}$$

$$E_- + E_+ > 0.8\sqrt{s} \;, \tag{3}$$

where the two sets of angular cuts are applied randomly, respectively to either the electron and positron, or vice-versa.
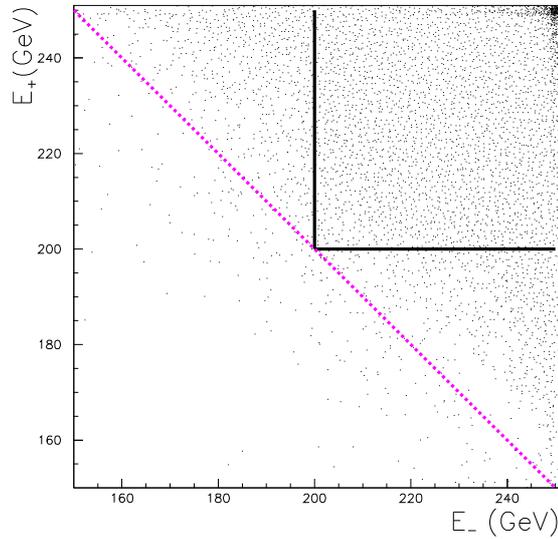

Figure 11: Energy of the positron versus energy of the electron for each final state particle of the Bhabha events passing the angular cuts defined in Equation 2.

The magnitude of BHSE is of the order of -0.015 for the ILC nominal beam parameter set, two thirds of this bias being due to beamstrahlung emissions. Both beamstrahlung emission and electromagnetic deflections vary with the bunch length, σ_z, the horizontal size, σ_x, and the energy of the collision, and thus also the corresponding bias on the integrated luminosity. The luminosity spectrum reconstruction based on the scattered Bhabha angles provides a good way to measure the amount of beamstrahlung and thus to predict the corresponding contribution to the bias, because the electromagnetic deflections do not modify significantly this spectrum. The expected experimental precision on polar angle measurements should enable reaching an accuracy of $5 \cdot 10^{-4}$ for the mean value of the luminosity spectrum. This is enough to control the luminosity bias from beamstrahlung at the 10^{-3} level. A fitting method, as the one suggested in [31], may allow to improve further on this. Once this is done, controlling σ_x and σ_z at the 20% level around the nominal values was found to be enough to limit the contribution to the luminosity bias from the deflections to 10^{-3}.

Unlike the beamstrahlung emission, there is no direct way to measure and quantify experimentally the electromagnetic deflections. Numerical simulations such as GUINEA-PIG [24] and CAIN [32] are then essential estimation tools. A practical implementation to compute all these effects is available at [33] and can be used for further studies.

2.5 Bhabha Scattering with Polarized Beams

To fully exploit the physics potential of the ILC, it is planned to equip it from the very beginning with a longitudinally polarized electron beam and, possibly, a polarized positron beam. The beam polarization is expected to be 80% for electrons and about 60% for the positrons.

For longitudinally polarized colliding beams, the purely electromagnetic (EM) part of the Bhabha cross-section can be expressed in the center of mass system as

$$\frac{d\sigma_{EM}}{d\theta d\phi} = \frac{d\sigma_{EM}^O}{d\theta d\phi} \left(1 + P_- P_+ A_{EM}^D\right), \tag{4}$$

where $P_-(P_+)$ is the electron (positron) beam polarization and A_{EM}^D is the double spin asymmetry. The superscript 0 indicates the cross-section for non-polarized beams. When the electroweak (EW) contribution to the Bhabha scattering cross-section is non-negligible, an additional term for single spin asymmetry A_{EW}^S appears,

$$\frac{d\sigma_{EW}}{d\theta d\phi} = \frac{d\sigma_{EW}^O}{d\theta d\phi} \left(1 + \left(P_- - P_+\right) A_{EW}^S + P_- P_+ A_{EW}^D\right). \tag{5}$$

A_{EW}^S and A_{EW}^D depend on the initial energy, while A_{EM}^D does not.

The various single and double asymmetries are plotted in Fig. 12 for the nominal beam energy of $E_{beam} = 250\,\text{GeV}$. These asymmetries affect the total Bhabha scattering cross-
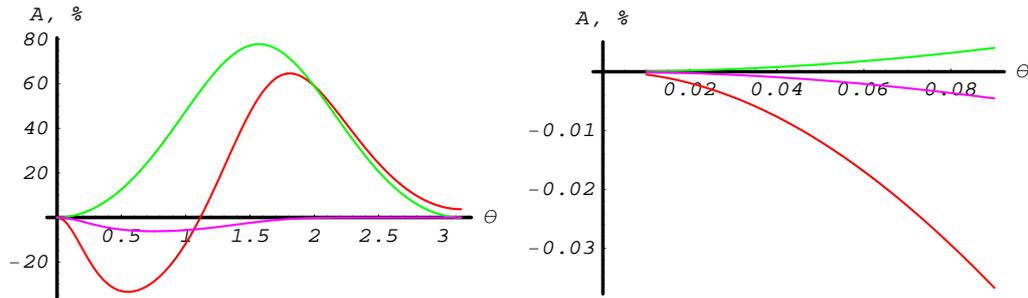
Figure 12: The spin asymmetries as a function of the polar angle θ. The left plot shows the full polar angle range, the right plot covers the range of the forward calorimeters. The green line is the result for A_{EM}^D, the red line for A_{EW}^D and the violet line for A_{EW}^S.

section. In case of purely electromagnetic interactions, the integrated Bhabha scattering cross-section is

$$\sigma^{EM} = \sigma_0^{EM} \left(1 + P_{e^-} P_{e^+} f_D^{EM}\right), \tag{6}$$

14

where f_D^{EM} is the total electromagnetic cross-section asymmetry. Neglecting the electron mass we obtain

$$f_D^{EM} = 0.093\% \tag{7}$$

independent of the energy of the incoming beams. In the electroweak case, the total cross-section is given by

$$\sigma^{EW} = \sigma_0^{EW} \left(1 + (P_{e^-} - P_{e^+})f_S^{EW} + P_{e^-}P_{e^+}f_D^{EW}\right). \tag{8}$$

The energy dependence of the single and double asymmetries, f_S and f_D, respectively, integrated over the angular range of LumiCal, is shown in Fig. 13. As can be seen, for
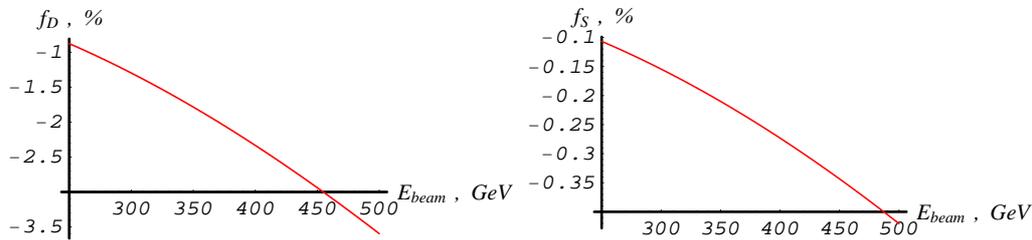

Figure 13: Double (f_D) and single (f_S) spin asymmetries as a function of the initial energy.

beam energies of hundreds of GeV, the polarizations of the beams change the Bhabha cross-section, integrated over the polar range of the LumiCal, by several per cent. Hence the polarization of the beams has to be taken into account in the measurement of the luminosity. In addition, it seems useful also to control polarization dependent higher order corrections.

3   Design of LumiCal

LumiCal is designed as a compact, highly granulated silicon-tungsten sandwich calorimeter. It will consist of two identical calorimeters. Each calorimeter has a cylindrical shape. In the LDC concept, as an example, the position of each calorimeter is 227 cm from the IP. The inner radius is assumed to be 8 cm and the outer radius 35 cm. Each detector arm will be around 20 cm in depth ($Z_{min} = 227$cm and $Z_{max} = 247$cm). A similar design with an adapted geometry is foreseen for the SiD concept.

Longitudinally, the LumiCal consist of 0.34 cm thick tungsten layers separated by silicon sensors planes. The silicon sensors thickness will be 300 μm (a 500 μm is also investigated). Each detector layer corresponds to about one radiation length. A preliminary mechanical design is shown in Fig. 14.

Systematics studies showed that it is best to position the LumiCal around the outgoing beams (see next sections).

The two half barrels can be clamped on the closed beam pipe. The position of the two parts of the detector with respect to each other will be fixed by the help of precise
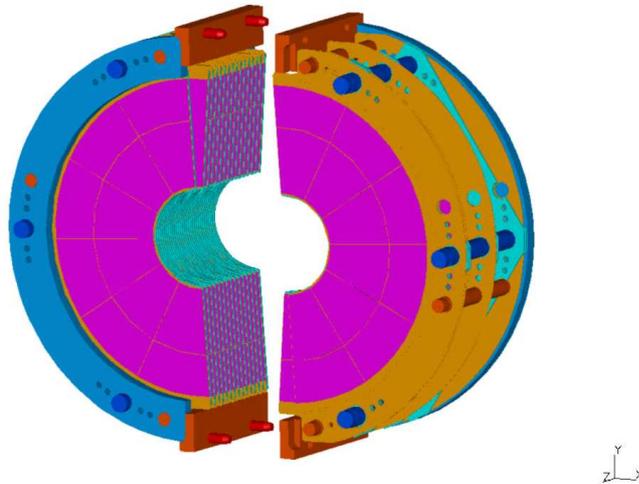
Figure 14: Mechanical design of LumiCal.

pins placed at the top and bottom of each C shaped steel frame. The latter stabilizes the structure and carries the heavy tungsten disks by the blue bolts. The light silicon sensors are glued to the ceramics support and positioned by the red bolts. The frame for the sensors is decoupled from the tungsten disk support; hence it does not suffer from a gravitational sag due to the tungsten disks. Optionally, we are investigating the possibility to glue the silicon sensors directly to the tungsten absorber surface with some insulation [34, 35]. More details of such a design are given in Sec. 3.6. The silicon sensors of 300 μm thickness are glued to a 1 mm thick ceramic support or directly to the tungsten surface and a 0.7 mm space is left for bonding. Thin glass with aluminum readout traces is foreseen to fan out the signals from pads to the charge sensitive preamplifiers. The place for readout electronics, connectors and cooling is foreseen at the outer radius of the calorimeter as shown in Fig. 15.

A final recommendation for the detector granularity and number of layers was not yet made. The studies done so far established only lower boundaries.

The simulation results for a LumiCal for the TESLA collider consisted of 30 layers in depth (equal to 30 radiation length). For the new ILC baseline with the option of going for 1 TeV center-of-mass energy, a 40 layer design is more likely. With 40 layers the detector energy resolution performance will be kept for the whole energy reach.

To reach a luminosity measurement with a precision of 10^{-4}, a minimal pitch of 1.1 mrad in the concentric granulation (θ) is required.

The background studies done so far show that a pitch of 0.26 rad ($= 15^o$) in the azimuthal plane is enough to separate a Bhabha signal from background. More comprehensive background studies will probably lead to a recommendation for a more azimuthally granulated design (the most common design being investigated is a 0.13 rad ($= 7.5^o$) pitch in ϕ).
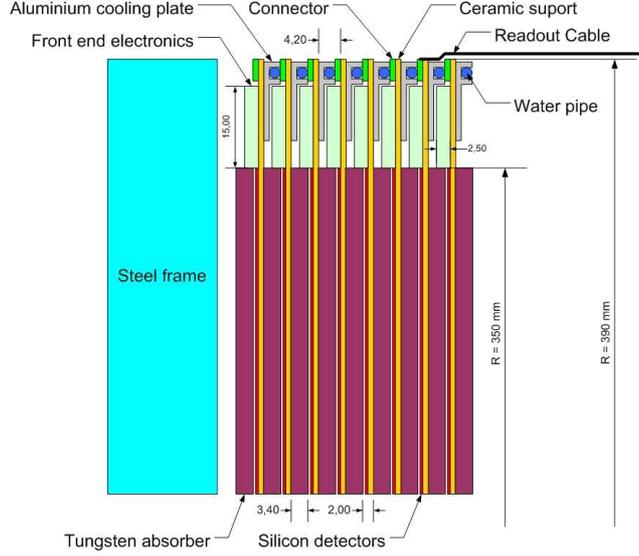
16

Figure 15: Mechanical design of LumiCal.

Following the pad design option, every readout plane is subdivided simultaneously concentrically and azimuthally to form individual pads.

3.1 LumiCal Placement Accuracy

The luminosity measurement at the ILC is done by counting Bhabha scattering events. The integrated Bhabha cross section is a strong function of the lower angular limit of the integration, θ_{min},

$$\sigma_{\mathrm{B}} \sim \theta_{\min}^{-2} \,. \tag{9}$$

Any misalignment of the components of LumiCal or biases in the reconstruction of the scattering angle will induce a systematic shift on the luminosity measurement.

To study constraints on the allowed misalignment of LumiCal, events were generated with BHLUMI 4.04 [36]. In the first step, the position of the e^+ and the e^- on the front face of LumiCal is calculated. The scattering angle is then deduced from these positions. The scattering angle constraint is applied to only one of the leptons, to e^+ for even events and to the e^- for odd events. Note that for any lepton to pass the energy cut, its scattering angle θ has to be in the range of the LumiCal acceptance.

In subsequent steps, the position and energy are subjected to systematic mis-reconstructions and the selection is reapplied. The change in the number of accepted events with respect to the number of originally selected events is a measure of the systematic effect induced by the particular mis-reconstruction. The size of the effects are varied in order to determine the required level of precision to achieve a goal of 10^{-4} uncertainty on the luminosity

$\Delta L/L$	$0.2 * 10^{-4}$	$1.0 * 10^{-4}$
inner radius	0.8 μm	4.2 μm
radial offset	290 μm	640 μm
distance of calorimeters	76 μm	300 μm
longitudinal offset	8 mm	18 mm
tilt of calorimeters	6 mrad	14 mrad
beam tilt	0.28 mrad	0.63 mrad
beam size	negligible	negligible

Table 3: Parameter requirements to achieve the required precision on luminosity measurement [19].

measurement. The same event sample is used for all steps so that statistical fluctuations largely cancel. A selection of requirements thus obtained are presented in Table 3.

3.2 Constraints on Angular Bias and Resolution

To achieve sensitivity to systematic effects comparable to the required relative precision on luminosity of 10^{-4}, large statistics MC samples are necessary. This cannot be achieved in a conventional manner by processing events through a full GEANT simulation. Instead, a fast MC was developed, with smearing effects implemented through parameterization of the performance established on smaller samples. The fast MC was coupled to the BHWIDE event generator. This MC allows detailed studies of various systematic effects.

The relative error on luminosity is proportional to the relative error of the Bhabha cross section

$$\frac{\Delta L}{L} = \frac{\Delta \sigma}{\sigma} \approx 2 \frac{\Delta \theta}{\theta_{min}}\,. \tag{10}$$

The luminosity measurement is based on counting Bhabha scattering events in a well defined acceptance region. The error on the measurement is caused by miscounting events. The relative error on luminosity can then be written as

$$\frac{\Delta L}{L} = \frac{\Delta N}{N} = \frac{N_{rec} - N_{gen}}{N_{gen}}\bigg|_{\theta_{min}}^{\theta_{max}}\,, \tag{11}$$

where N_{gen} is the number of generated events in a given angular range, and N_{rec} is the number of events reconstructed in the same angular range.

Two parameters describe the quality of the position reconstruction. One is the bias, $\Delta \theta$, and the other is the detector resolution, $\sigma(\theta)$. The limitation of $\Delta \theta$ can be easily obtained from the analytical formula and leads to a constraint of $\Delta \theta < 1.6 \cdot 10^{-3}$mrad.

For the constraints on $\sigma(\theta)$, we used the fast MC. We smeared the generated events assuming a range of detector resolutions with zero bias. The influence of the detector θ
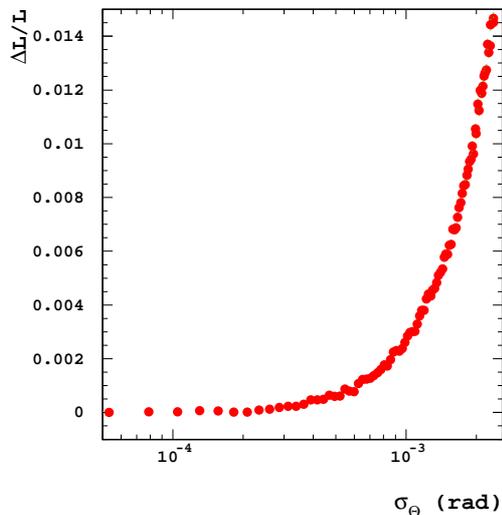
Figure 16: The relative error on luminosity, $\Delta L/L$, as a function of θ resolution, σ_θ, calculated using five million Bhabha scattering events for each point.

resolution on the luminosity error is shown in Fig. 16. $\Delta L/L$ is found to be a parabolic function of $\sigma(\theta)$ [37].

From this parabolic dependence, one may derive the precision with which $\sigma(\theta)$ has to be known to preserve the 10^{-4} precision on luminosity. For example for $\sigma(\theta) = 1.6 \cdot 10^{-4}$mrad, an error of $\pm 20\%$ would lead to an error on $\Delta L/L \simeq 0.4 \cdot 10^{-4}$. In conclusion, the most important issue is to able to control the angular bias to below $1.6 \cdot 10^{-3}$mrad.

3.3   Systematics Effects at Small and Large Beam-crossing Angles

In the head-on collision collider the position of LumiCal was naturally aligned with the beam-line. Studies are done on the requirements of the control of the inner acceptance radius, the distance between the two calorimeters, the radial beam position, the longitudinal offset of the interaction point and of the tilt and twist of the calorimeters [19]. As the most critical parameter the control of the inner acceptance radius was identified. To maintain the systematic uncertainty of the luminosity measurement on the level of 10^{-4} this quantity must be controlled with an accuracy of a few μm.

With a beam crossing angle the detector axis usually has an angle of half the crossing angle with incoming and outgoing beams. We repeated the study on position accuracy requirements for two cases: the LumiCal is centered around the detector axis or centered around the outgoing beam axis. When the LumiCal is centered around the detector axis, the ϕ symmetry of the Bhabha cross section is lost. The Bhabha cross section in the laboratory frame depends then on the polar angle θ and on the azimuthal angle ϕ (due to the boost, see Fig. 17), hence the systematic uncertainties become ϕ dependent.

Bhabha scattering is simulated for crossing angles of 2 mrad, 14mrad and 20mrad using the BHWIDE and the BHLUMI generators. Selection cuts, as described in section 2.6,

are applied on the generated events and the number of Bhabha events is counted in the LumiCal acceptance region. Then the position or the geometry of the calorimeters are
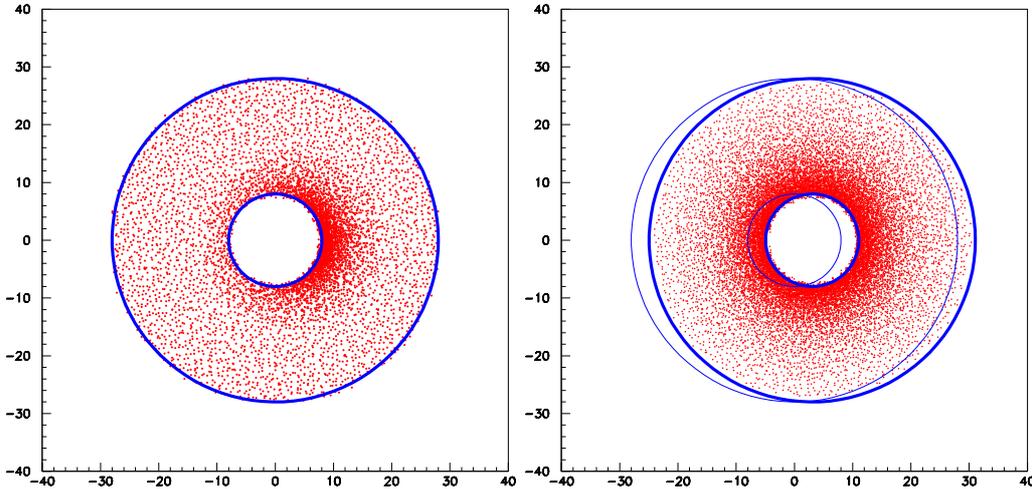

Figure 17: Distribution of Bhabha scattering events for a 20mrad crossing angle ILC. Two cases are shown: the detector is positioned on the detector axis (left) and along the outgoing beam (right).

shifted in reasonable steps and the event selection is reapplied. The change of the number of accepted events with respect to the ideal geometry gives the systematic shift of the luminosity. The slope of the luminosity shift as a function of the shift of the parameter is denoted as systematic sensitivity.

No significant difference in the systematic sensitivity between the two possible alignments of LumiCal is observed for shifts in the inner acceptance radius and Z positions of the calorimeters. However, a dramatic change of the systematic sensitivity is found in case of larger crossing angles for radial beam axis shifts and tilts of the calorimeter axes. Examples are shown in Fig. 18 . Allowing a tilt of 0.1 mrad, the relative shift of the luminosity, $\Delta L/L$, is strongly dependent on the angle ϕ and would change the measured luminosity for $\phi \approx \pi/2$ by almost 1 % in the case of a 20 mrad beam crossing angle. An even larger systematic sensitivity is observed for radial displacements of the beam axis as a function of the azimuthal angle ϕ. Note, that the systematic shifts for small changes in the tilt or the radial beam position are, for certain values of ϕ, by more than an order of magnitude larger the the anticipated precision of the luminosity measurement. Hence, in order to control the systematic uncertainty of the luminosity measurement, the LumiCal must be centered around the outgoing beam axis.

3.4   Background from Pairs for Non-zero Crossing Angle

A large beam crossing angle in the interaction region complicates the luminosity measurement. The beam particles and backscattered particles will have a bigger transverse momentum in the region of the magnetic field and the total background will increase. One
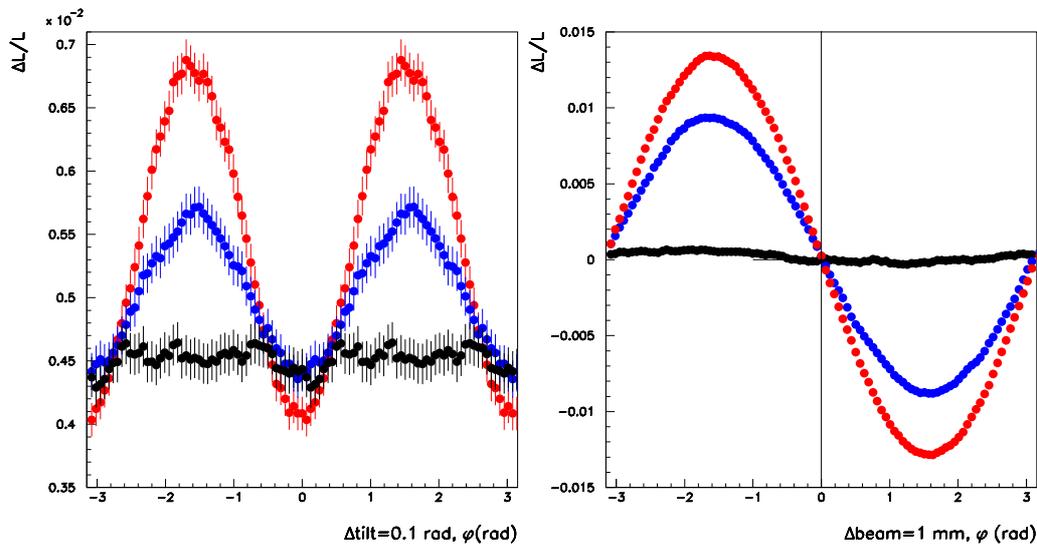
20

Figure 18: The relative shift on the luminosity as a function of the angle of tilts (left) and the angle of beam shifts (right) for three cases: the detector is aligned on the outgoing beam (black dots); for a 14mrad crossing angle with the alignment on the detector axis (blue dots); the detector is aligned on the detector axis for a 20mrad crossing angle (red dots).

of the challenges of this study will be to deal with the inhomogeneity and asymmetry in the ϕ angle of this background.

The recommended design for the head-on collision has a big acceptance region which offers the possibility to increase its inner radius and to get away from background close to the beam. For larger beam crossing angle this is necessary as can be seen in Fig. 19. The energy deposition per bunch, originating from beamstrahlung pairs, is shown as a function of the LumiCal inner radius. This figure shows also the 'cost' in terms of statistics if the inner radius is increased. For this particular geometry (LumiCal at z = 305 cm) above an inner radius of 13 cm there is no background and there is enough statistics to keep the statistical error on luminosity at the required level.

Similar studies are being done on the different crossing angle ILC versions. First results for the new baseline ILC design of 14mrad, with an anti-DID[1] magnetic field indicate that above an inner radius of 10 cm this background is negligible.

3.5   Simulation of Signal Digitization

The signature of a Bhabha event in the LumiCal is an e^+e^- pair, where the leptons are back to back and carry almost all the of the initial energy. 250 GeV electrons were used in order to find the maximum signal collected by a pad. In order to determine the lower bound, the

---

[1]Detector integrated dipole (DID). A magnetic field directed along outgoing beamlines with a kink at the IP-plane is called anti-DID.
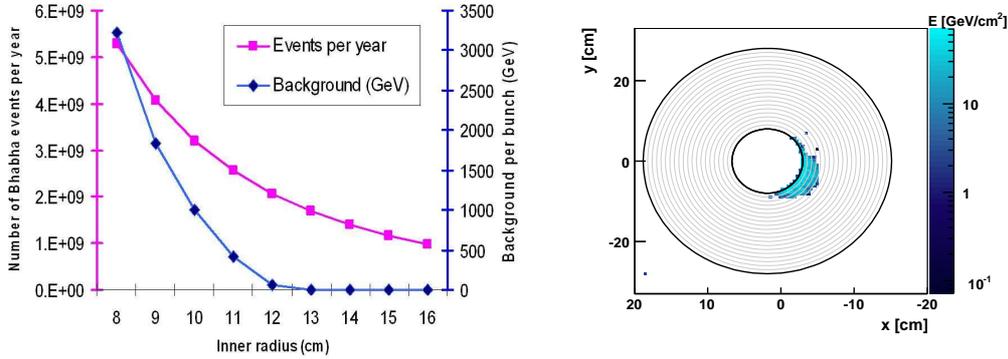
Figure 19: On the left, the background originating from beamstrahlung pairs (blue) and the number of expected Bhabha events per year (pink) as a function of the inner radius. On the right, beamstrahlung pairs hitting the LumiCal. The total amount of beamstrahlung depositions is several TeV. This simulation was done for 20 mrad crossing angle, DID field configuration and a LumiCal position at z = 305 cm. Nominal beam parameters are assumed at a centre-of-mass energy of 500GeV.

passage of muons through the detector was simulated. In the present conceptional approach, muons, which do not shower, will be used to intercalibrate the LumiCal pad signals. Muons may also be used to check the alignment of the detector. The electronics of LumiCal should allow the identification and measurement of minimum ionizing particles (MIPs) as well as of high energy electrons from Bhabha scattering. The most commonly used ADCs, and therefore the cheapest, are 8-bit ADCs. As a consequence, to accommodate the constraints imposed by physics, the signal output of the detector will have to be digitized using two separate gain amplifiers. The simulation results for $500\,\mu$m thick silicon sensors are that one would be able to measure 82% of the signal with an accuracy of 2.2 fC (0.2 MIPs) and the rest with an accuracy of 45.5 fC (6.9 MIPs). The simulation confirms earlier results [38], that using a 10-bit ADC does not change the performance of the detector and a similar energy resolution is obtained compared to pure analogue information [39].

3.6 Alternative Mechanical LumiCal Design

In the simulation of an alternative mechanical design we considered an envelope for the LumiCal as described in the following. In the radial direction, the minimal radius is 100 mm and the maximal one is 320 mm. Along the beam, it will be positioned between z = 2300 mm and z = 2500 mm. This follows the mechanical design as it is shown in the LDC layout in Fig 1.

On both sides of the interaction point there will be one LumiCal detector. Each calorimeter is in a form of a barrel which is divided into two parts along the vertical plane. It is assumed that there are two support points for the half of the barrel in an equal distance from the gravity center in the horizontal direction.

The plane of the division into two parts of the tungsten plates is not along the vertical plane but rotated around the central axis of the barrel by +3.75 deg or -3.75 deg. It has to be pointed out that the tungsten plate at +3.75 deg has the same shape as the tungsten plate at -3.75 deg. In that way the LumiCal is composed of only one type of tungsten plates. To assemble the calorimeter we need two types of rings. These rings are used as inserts and therefore after connecting them with the tungsten plate the inner ring hole is very precisely drilled. By using special bolts (M12), the barrel can be assembled and placed on the support. What is important is that the tension in the bolts should be about 15 MPa. The half barrel is composed of fifteen tungsten plates to which silicon detectors have been glued on both sides. Between these tungsten plates there are fourteen tungsten plates without detectors.

The main advantage of the new design is its simplicity. The structure is composed of a very limited number of elements. We have one type of tungsten plates, two types of the rings, the special M12 bolts and two supporting elements as shown in Fig. 20. Note that the silicon sensors are glued on the both sides of the fifteen tungsten plates. In addition, the structure fulfills the symmetry condition which is very important from the point of view of thermal deformations. Calculations of the deformation of one tungsten plate subjected to the dead load show that the maximal value of the vertical displacement is 0.00024 mm. This suggests that the tungsten plates are stiff enough and should be used to support the silicon planes.

For the case that the half barrel is supported at four points, values of vertical displacements are at most about 0.04 mm. We can use such a support when the detector is transported. The deformation of the structure can be reduced nearly six times using six supporting points or more than one hundred times using the full length support as shown in Fig. 21.

The calculations presented above show that the proposed structure can be accepted from the point of view of its stiffness. Moreover, the mechanical design is very simple and has many advantages. It fulfills the condition of symmetry and the number of the silicon planes with which the positions have to be monitored is reduced by a factor of two.
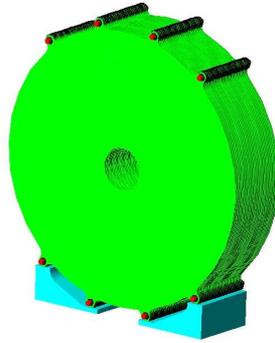
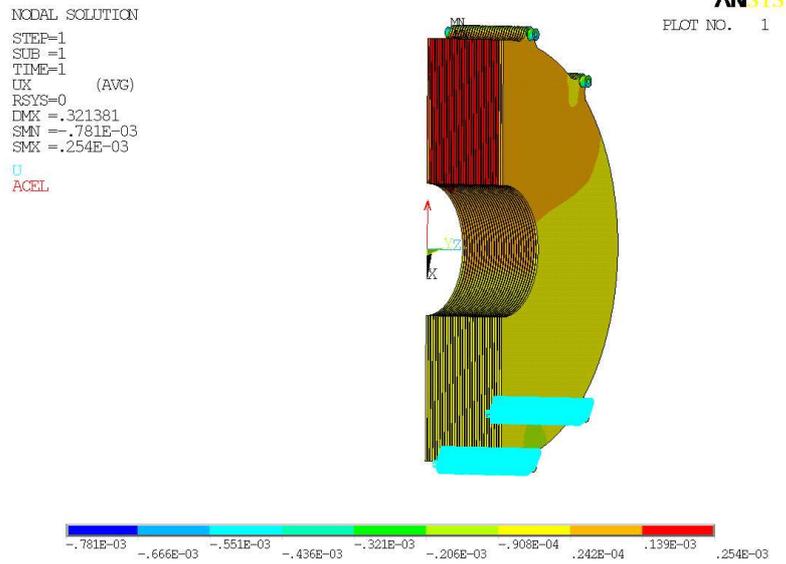Figure 20: The two parts of the LumiCal joined together.

Figure 21: The result of the calculation of the LumiCal deformation when supported over the full length.
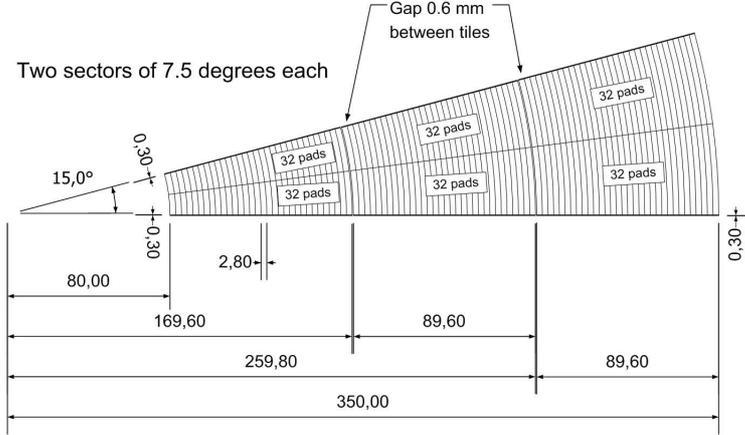
Figure 22: Two azimuthal sectors consist of three silicon tiles.

3.7 Silicon Sensor Layout for LumiCal

The proposed LumiCal detector will consist of 30 to 40 layers of tungsten of one radiation length thickness and $300\,\mu$m thick silicon sensors layers. The sensitive region extends from $80\,\text{mm}$ to $350\,\text{mm}$ in radius in this particular geometry. Each such layer will include 48 azimuthal sectors. The sector will be segmented into 96 radial strips with a constant pitch. The sensor plane will be built from a few tiles because the current technology is based on 6-inch wafers.

Reference marks are foreseen on the detector surface for precise positioning. The layout of the sensors and the mechanical design of the calorimeter do not allow sensors to overlap. To reduce the impact of the gaps odd and even planes are rotated by $3.75°$ with respect to each other. Radial gaps of the sensors will overlap in depth in that particular design.

The design of two azimuthal sectors with details on the sensor segmentation is shown in Fig. 22. The gap between radial tiles and between every two sectors is $0.6\,\text{mm}$. With the guard rings of $0.2\,\text{mm}$ width the inactive area around the tiles will have a width of $\approx$ $1\,\text{mm}$.

The capacitance of the pads varies from $10\,\text{pF}$ for the pads close to the beam pipe to $45\,\text{pF}$ for the outer pads. Two tiles of sensor sectors fit onto a one single 6-inch wafer. The new geometry and segmentation have to be implemented in MC simulations. The influence of the proposed design to the precision of the luminosity measurement has to be studied finally, especially the problem of the overlapping radial gaps between sensor tiles.

3.8 Detector Laser Alignment

The luminosity measurement requires extremely precise alignment of the two LumiCal detectors, each with respect to the other and very precise positioning with respect to the beam line and the interaction point. From Monte Carlo simulations we derived the precision requirements on the inner radius, on the distance between the calorimeters along the beam axis and on the radial position with respect to the beam as summarized in Tab. 3. The initial inner radius of the detector can be measured in the lab using optical methods and precision movable table with the cross check of an interferometer. The beam pipe is proposed as a suitable reference for the distance along the beam and transversal displacement and can be precisely surveyed before installing. The Beam Position Monitors are mounted at well known position inside the vacuum pipe also and that would allow determining the actual position of LumiCal with respect to the beam position.

The position monitoring of the detector should not interfere with the beam pipe, hence a non contact system is preferred. We have chosen an optical laser system with a CCD matrix sensor to measure the transversal (x, y) and longitudinal (z) displacement of the LumiCal with respect to the beam pipe flange. The position sensors will be placed between the rear side of the detector and the beam pipe flange. The radiation dose in that area seems to be small because of shielding, but the radiation hardness of the sensor has to be studied. In case the radiation dose is not acceptable, we can use radiation hard CMOS matrix sensors. The use of a few position sensors per calorimeter would allow to determine also the angle between the detector axis and the beam direction and assure better reliability in case of position sensor failure.

3.8.1 Measurement Setup

We have set up an experiment [40] using the semiconductor laser module LDM635/1LT from Roithner Lasertechnik with a wavelength of 660 nm and the BW camera DX1-1394a from Kappa company 640 x 480 with a Sony ICX424AL sensor 7.4 μm x 7.4 μm unit cell size.

The laser was mounted on a special precision alignment holder on the optical bank. The camera was placed on the XYZ ThorLabs 1/2" travel translation stage MT3 with micrometers (smallest div. 10 μm). To control independently the camera displacement, we were using the Renishaw optical head linear encoder RG24 with a resolution of 0.1 μm. We had to reduce the amount of laser light using 3 neutral density filers with the attenuation factor of 2 each because the sensor saturates.

The camera was translated in one direction in 50 μm steps and a picture was taken. To measure the longitudinal (z) displacement we used a second laser beam illuminating the sensor with an angle of 45 degrees (Fig. 23).

For the present setup we have used a half transparent mirror to split the laser beam and another mirror to direct it to the sensor with the proper angle. First measurements of z displacement show that calibration of the mirror angle is crucial for the final accuracy.
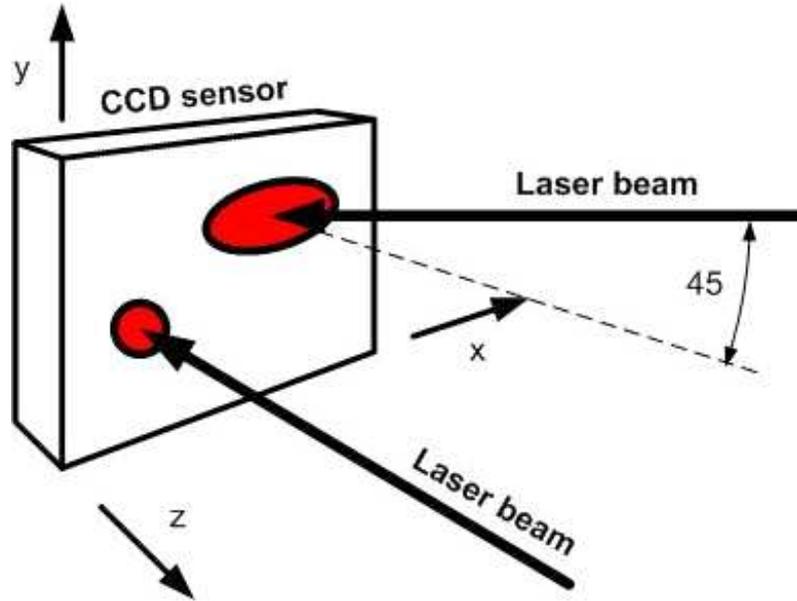
Figure 23: Simplified diagram of two laser beams setup.

3.8.2 X,Y,Z Displacement Measurement Results

The CCD camera was moved across the laser beam in $50\,\mu$m steps and pictures were taken at every step. Two algorithms to calculate the centre of the beam spot was developed and both are in agreement. The development of algorithms to determine the center of beam spots is still in progress because there is an area to achieve better accuracy. The results using the last developed algorithm shown in Fig. 24, are very promising, with the difference between real and calculated position being less than $\pm\,1\,\mu$m.

We have made a few series of measurements and the results vary slightly. Previous results of displacement measurements in transversal direction using a low cost web camera can be found in [41]. The progress of the measurement method development was presented at a few workshops i.e. [42, 43, 44, 45]. The results of displacement measurement in z direction are similar, but show a slightly stronger dependence on the different background cuts on the light intensity. This effect will be further investigated.

3.8.3 Stability Measurement

We have studied the long term stability of the laser positioning system prototype. First results show that the main problem is the temperature stability of the supports for lasers and camera. We have found, that the crucial point in our setup is the XYZ movable table which, due to temperature changes, gives a meaningful error of a few micrometers in a 24 hours period. For the stability tests, we have mounted the lasers and camera on one piece of aluminum and placed the setup in a thermal insulated chamber (passive thermostat). The results for perpendicular beam and 45 degrees angle are shown in Fig. 25(a) and 25(b),
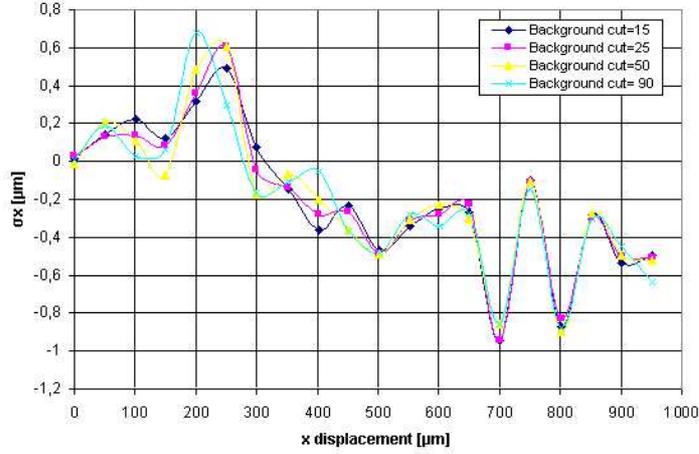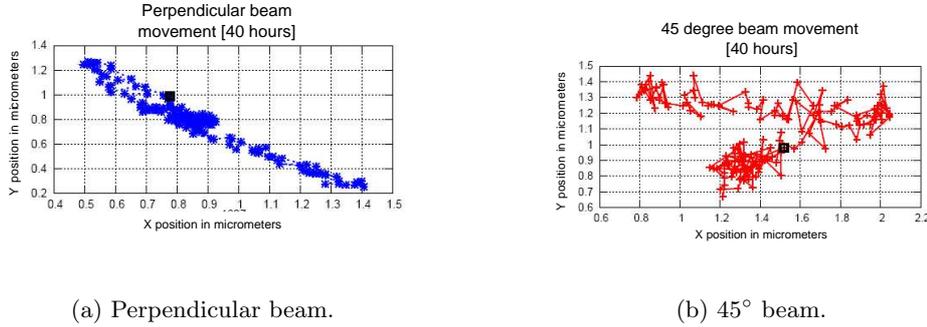
27

Figure 24: Difference between calculated and real position in x direction.

respectively.

(a) Perpendicular beam.

(b) 45° beam.

Figure 25: Laser beam spot stability over 40 hours.

It is clearly seen that both spots move around $1\,\mu$m over 40 hours of measurements. The reason is probably the temperature expansion of aluminum support and the CCD sensor movement inside the camera case (is not well fixed). Also the micro pointing of the laser diode beam ($\approx 0.5\,$mrad) has to be considered. Stability of the laser beam spots has to be investigated more carefully; for further experiments we are preparing a thermally stabilized chamber and more stable support. A newly designed camera with a better fixed CMOS sensor will also be used.

We have shown that using the above described method for measuring the detector displacement we can achieve an accuracy better than the required one. With the outlined refinements to the set-up, a better picture analysis algorithm can be developed. A two-laser system will give us higher reliability and a better beam spot shape. The calibration
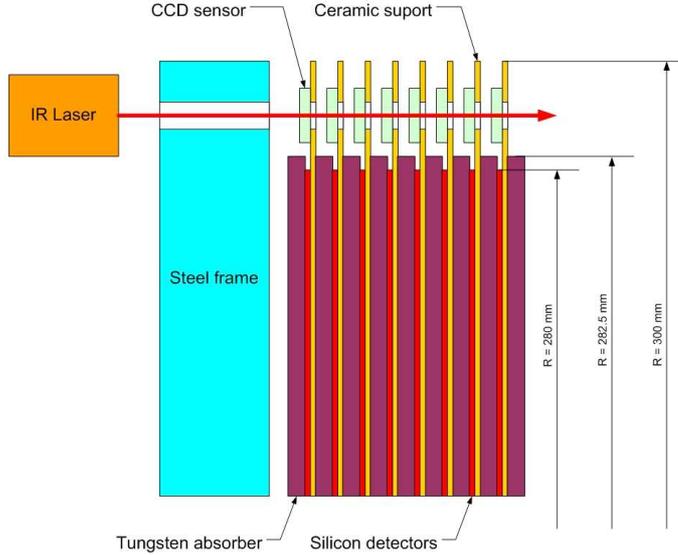
Figure 26: Sensors planes laser alignment using transparent light sensors.

procedure has to be developed to calibrate the angle between beams to 45 degrees. This calibration is essential to achieve better accuracy in the longitudinal (z) displacement measurement.

A work on displacement sensor miniaturization has started. We have chosen a CMOS fine pixel sensor and the readout electronics has been designed. The PCB is under design.

3.8.4 Sensor Planes Alignment

Not only a full detector has to be aligned precisely, but also the position of the sensors planes has to be known within a few μm. We foresee an optical system to control the sensors planes displacement on-line, shown in Fig. 26.

A laser beam from a semiconductor laser module placed in the hole in a C-shape steel frame goes through the semitransparent CMOS position sensors (similar to sensors used at CMS).

Another possibility is to use a wire tensed between front and rear C shape steel frame passing through the holes in all detector planes. Quite simple capacitive sensors can measure the transversal displacement of the sensor planes with respect to the wire with the accuracy of $\approx 1\,\mu$m.

4 Motivation for a Small Polar Angle Calorimeter - BeamCal

4.1 The Impact of Low Angle Electron Identification on Physics

The forward calorimeters are an important tool to identify two photon events by detecting either one electron or positron with an energy near to the beam energy. Two photon events constitute the most serious background for many search channels which are characterized by missing energy and missing momentum. Lets consider e.g. the search for the slepton and neutralino particles with quasi-degenerate masses which are predicted in some interesting realizations of the super-symmetric model. It has been shown, in the context of the co-annihilation scenario, that staus and neutralinos could combine to provide a plausible, quantitative, explanation for the amount of dark matter in the universe [46]. In the phenomenological analysis which was carried out, the framework of super-gravity was used for definiteness in the predictions. Given constraints from recent WMAP measurements, such scenarios appear to be favoured.

It is assumed that the sleptons are the heavier particles. They are pair-produced and then decay into the lighter neutralinos, which escape undetected, and regular leptons. If the masses are very close, the produced leptons are soft, with a momentum range which can be directly related to the difference of masses between the slepton and neutralino. Since the relative orientation of the slepton decays is arbitrary, the two leptons are usually very acoplanar. Lepton pairs produced in photon-photon processes have in most cases a significant different topology and kinematics and can be rejected by simple cuts. However, since the two photon cross-section is typically five orders of magnitudes larger, events in the tails of the kinematic distributions become important. When the spectator electron is in the acceptance of the BeamCal, the produced lepton pair can be acoplanar enough to look like the searched signal events. Such events must be vetoed by explicit detection of the spectator electron in the BeamCal. The range of angles where such a veto is needed can be estimated from simple kinematic arguments in relation to the slepton-neutralino mass difference. For a 5 GeV mass difference, rejection is needed down to 10 mrad in the case of smuons and down to roughly 5 mrad for staus. The requirement is more stringent for staus because of the additional loss of energy and momentum due to the neutrinos in the tau lepton decay. The level of rejection required has been estimated in [47] for the case of a stau search analysis optimized for a 5 GeV mass difference. It was found that spectator electron suppression factors ranging between 10^{-1} and 5×10^{-4} were needed in the BeamCal, when going from the innermost part of the acceptance (at about 4 mrad) towards its largest values. With such rejection factors, signal to background values of order one could be achieved. This requirement was estimated for the particular bench-mark scenario in [46]. It should be taken as indicative and will in general depend on the exact mass difference and cross-sections involved.

To obtain such values of the suppression factor, a very good separation must be achieved between high-energy electrons with momenta close to that of the beam and the pile-up of low-energy beamstrahlung pairs. The most difficult region is the innermost part of the acceptance, where most of the beamstrahlung pairs are stopped. Our studies have shown that an electron veto inefficiency between 10^{-3} and 10^{-4} could be achieved in most of the

BeamCal area, beyond the innermost ring. It has also been shown that for geometries involving a large crossing-angle, the distortion in the beamstrahlung pair profile in the BeamCal, from the transverse components of the solenoidal field, can seriously reduce the capability to veto high-energy electrons. ILC beam parameter sets where the luminosity is achieved with increased beamstrahlung, e.g. the Low Power and High Luminosity sets [48], are also less favourable in this respect.

Another aspect of the requirement comes from the need to avoid excessive veto due to Bhabha scattering events superimposed on signal events. The probability for this to occur is not negligible in the lower part of the acceptance. To minimize the impact, Bhabha events must be identified in the BeamCal with good efficiency, by exploiting as much as possible the coincidence, back-to-back topology and energy balance with both sides of the BeamCal. To match the requirements on background suppression efficiency and Bhabha event identification high granularity and compactness is required in the BeamCal.

4.2 BeamCal as a Beam Monitor

The BeamCal allows a bunch-to-bunch measurement of low-energy beamstrahlung pairs produced in the collisions. The deposited energy and its distribution depend on the actual beam parameters. The information can be used for a fast luminosity optimization by providing it to the beam delivery feedback system. The fraction of electrons and positrons from beamstrahlung hitting the BeamCal is about 5-10 % of the total and amounts to about 10-20 TeV of energy per bunch crossing. Using the total energy deposits and several spatial asymmetries, information can be extracted not only on the overall luminosity achieved in each bunch collision, but also on the relative offsets between the bunches and on their sizes. Such information is essential to compute corrections then used by the beam delivery system, BDS, to optimize and maintain a high luminosity over a long time.

While the total amount of beamstrahlung pairs is not directly proportional to the luminosity, the relative information provided can be efficiently used for optimization following the "dithering" feedback approach pioneered at the SLC at SLAC [49]. With a more detailed analysis of the deposited energy profile, it has also been shown that both transverse and longitudinal beam sizes and transverse offsets can be reconstructed. A complete reconstruction of all these parameters simultaneously seems possible, however some of the parameters are highly correlated [50]. In this case the best results are achieved by combining the analysis with that of other diagnostic tools. For example, if the longitudinal beam sizes are known from measurements further upstream in the system, and if the measurements of the transverse offsets from beam-beam deflections are used, then the reconstruction of transverse beam sizes can be very precise. Another interesting method is based on constructing suitable ratios of energies measured in different regions of the BeamCal. An example is provided in the method studied at KEK [51], which showed that excellent precision could be obtained on the vertical beam size by analyzing the azimuthal distribution of the energy profile.

Although it has not been fully demonstrated yet, it is expected that the amount of information which can be extracted from the BeamCal energy profiles will not depend significantly on the particular geometry chosen for the interaction region. Different detector

magnetic field maps, denoted as DID (Detector Integrated Dipole) and anti-DID, in the case of larger beam crossing angles [52] will however have impact on the distribution of the energy depositions on the BeamCal, hence the algorithms to extract beam parameters must be tuned for each configuration separately.

5 Design of the BeamCal

BeamCal is designed similar to LumiCal. However, since it will be positioned closer to the beam-pipe as shown in Figure 1, it will be hit by the electrons and positrons originating from beamstrahlung photon conversions, carrying several 10 TeV of energy per bunch crossing for nominal beam parameters. The distribution of this energy is shown in Figure 27. The energy density is largest at small calorimeter radii and strongly dependent on the azimuthal angle. The latter is the result of the flat beam and the helical trajectory of electrons and positrons in the magnetic field inside the ILC detector. With growing radius the energy density drops showing a sharp border of the affected area, though a small number of particles can be found at larger radii.
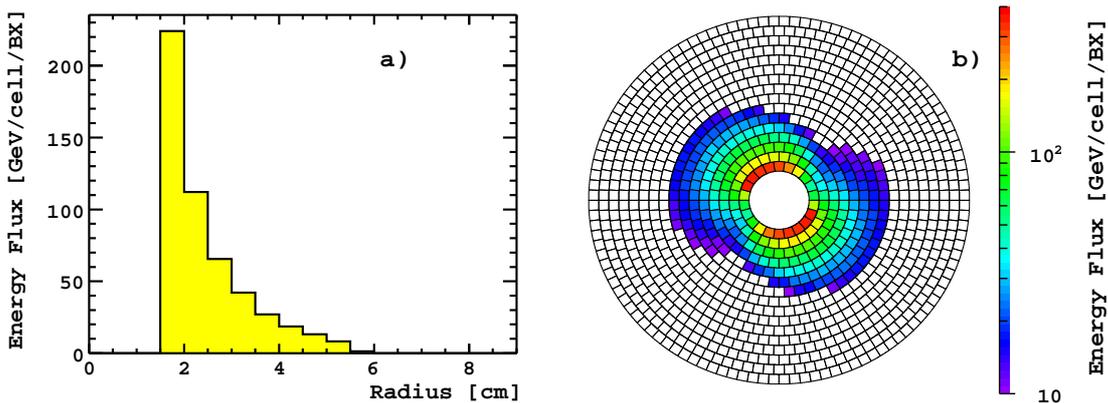

Figure 27: The energy density of beamstrahlung remnants per bunch crossing as a function of a) radius and b) position in the $r - \varphi$ plane. The centre-of-mass energy is 500 GeV. The maximal value of the density is 350 GeV per cell.

The total dose absorbed by a sensor pad per year is obtained from the energy deposited in its volume per bunch crossing multiplied by the number of bunch crossings expected per year. The simulation is done for all beam parameter sets as given in Table 4 for 500 GeV centre-of-mass energy [48]. The distributions for the two extreme cases, LowQ and LowP, are shown in Figure 28. The Nominal and LargeY parameter sets result in doses in between them. There is a large difference in the dose itself and in the size of the affected area for LowQ and LowP parameters. The maximum doses are 0.44 MGy/year and 4.3 MGy/year for LowQ and LowP parameter sets, respectively. To operate BeamCal sensors which withstand these doses are needed.

Fine granularity is necessary to identify the localized depositions from high energy electrons and photons on top of the energy depositions from beamstrahlung pairs. Sharing

	Nominal	LowQ	LargeY	LowP
Bunch charge [10^{10}]	2	1	2	2
Number of bunches	2820	5640	2820	1330
Gradient [MeV/m]	30			
$\gamma\epsilon_x/\gamma\epsilon_y$ [10^{-6} mrad]	10 / 0.04	10 /0.03	12 / 0.08	10 / 0.035
β_x / β_y [mm]	21 / 0.4	12 / 0.2	10 / 0.4	10 / 0.2
σ_x / σ_y [nm]	655 / 5.7	495 / 3.5	495 / 8.1	452 / 3.8
σ_z [μm]	300	150	500	200
Luminosity [10^{34} cm^{-2}s^{-1}]	2.03	2.01	2.00	2.05

Table 4: Beam parameters for the different accelerator designs at $\sqrt{s} = 500$ GeV.
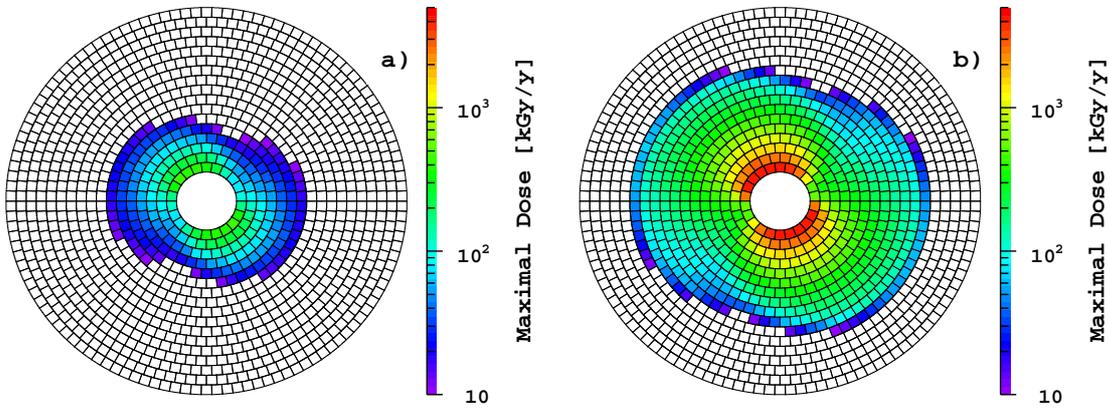

Figure 28: The expected dose in the most exposed longitudinal plane as function of position in the $r - \varphi$ plane at a) LowQ and b) LowP beam parameter configuration.

the shower signal between neighboring segments will improve the position resolution. Since the beamstrahlung energy deposition varies considerably with R and φ, and fluctuates from bunch to bunch, a dynamic range of $\mathcal{O}(10^3)$ is required for an efficient electron shower reconstruction [1].

We simulate a sampling calorimeter longitudinally divided into 30 disks of tungsten, each 1 X_0 thick interleaved by active sensor layers of 0.5 mm thickness. The Molière radius is about 1 cm. The sensitive planes are divided into pads with a size of about half a Molière radius in both dimensions, as shown in Figure 27b.

Head-on and 2 mrad beam crossing angle schemes, hereafter denoted as small crossing angles, foresee one beam-pipe at the position of BeamCal as shown in Figure 1. In the case of a larger crossing angles, 14 or 20 mrad, incoming and outgoing beams need two separate beam pipe openings. We center BeamCal on the outgoing beam. The instrumentation of the small region between the beam pipes is technically difficult and we assume that a sector containing the incoming beam-pipe will not be instrumented. Table 5 summarizes the BeamCal geometries we assumed for the various beam crossing angle schemes.

scheme	R_{in} [mm]	R_{out} [mm]	blind area
head-on	15	100	no
2 mrad	20	100	no
14 mrad	15/20	165	40°
20 mrad	15/20	165	30°

Table 5: Geometries of the BeamCal for various crossing angle schemes. For large beam crossing angles the two given inner radii specify the opening for the incoming/outgoing beam.

5.1 Single Electron Detection Efficiency

We study the efficiency to detect single high energy electrons on top of the widely spread deposition from pair background. First background events are generated using the GUINEA-PIG program [24] for the generation of the e^+e^- pairs originating from a bunch crossing. A full BeamCal simulation is done with a GEANT4 [53] based software and the deposition on each pad is stored. The depositions in each pad for about 10 background events are averaged defining the average background deposition and the rms for each pad. In the second step single high energy electrons or positrons are generated and their shower is simulated. Again the depostions per pad are stored. Then a random background event is
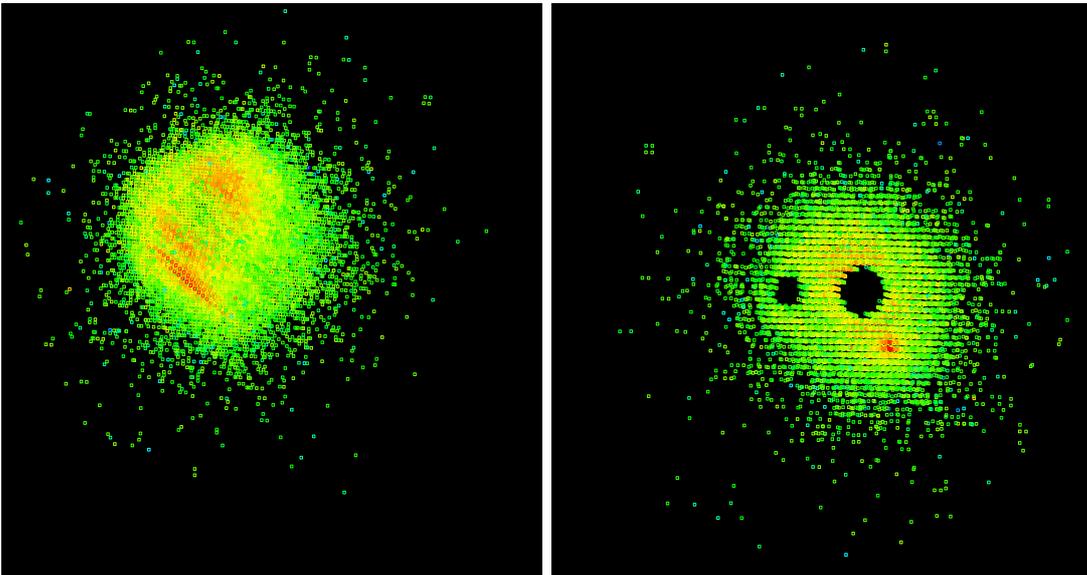

Figure 29: The shower due to the electron from a two photon event of nearly 250 GeV shown overlayed with the beamstrahlung pairs from a random bunch crossing. The figure on the left is the sideview and on the right is the head-on view. The presence of the electron beam exit beam pipe at 7 mrad to the forward direction and the entrance beam hole of the positron beam at -7 mrad are also visible.

overlayd with an electron shower to form a signal event as shown in Figure 29. From this signal event the averaged background deposition is subtracted in each pad. For comparison we also subtract the averaged background depositions from a random background event. The result is shown in Figure 30 where the depositions after subtraction are plotted as a function of the calorimeter depth. We see the clearly the excess of signals originating from
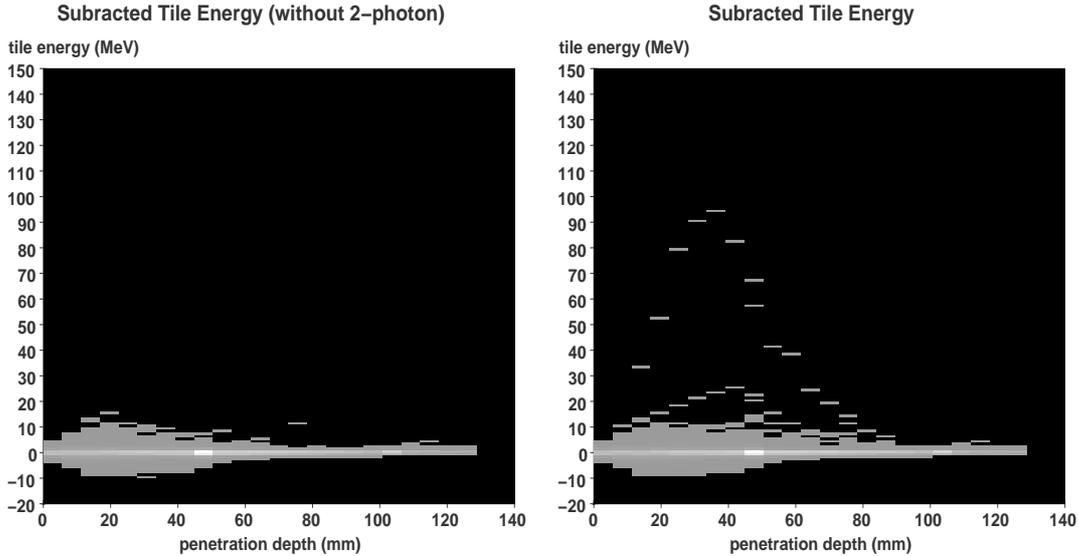

Figure 30: The Figure on the left shows the energy depositions of beamstrahlung pairs originating from one bunch crossing alone when subtracted by the average energy deposited from the average of 10 buch crossings. The distribution about a mean of zero shows that our determination of the average is reasonable. The Figure on the right shows the left over signal when we overlayed the shower from the electron of a two-photon process. The contribution to the signal from this energy deposition is evident.

the electron shower with the expected longitudinal shape.

The average efficiency to veto electrons with energies in the range of 75 to 250 GeV as a function of the calorimater radius is shown in Figure 31 for small crossing angles and nominal beam parameters. An electron of 250 GeV is vetoed even in regions with high background with almost 100% efficiency. The efficiency drops near the innermost radius, partly due to shower leakage. Electrons of 75 GeV are identified with high efficiency only at larger radii.

Performing the reconstruction, fake electrons can be found. This can be either a high energetic particle originating from beamstrahlung pairs or background fluctuations which mimic the electron signal. In this study the electron reconstruction algorithm is tuned such that the rate of fake electrons is below of 10% [1].

5.2 The Impact of the Pad Size on the Electron Detection

The efficiency to identify high energy single electrons as shown in Figure 31, is the essential performance parameter of BeamCal. In particular in the inner part of the BeamCal the efficiency decreases due to beamstrahlung depositions. We studied this efficiency for sensor pad sizes between 4×4 and 10×10 mm^2. The result is shown in Figure 32 for the inner part of BeamCal. The inefficiency for the identification of 200 GeV electrons, plotted as a function of the pad size, has a shallow minimum around 5×5 mm^2, corresponding to about half a Molière radius.
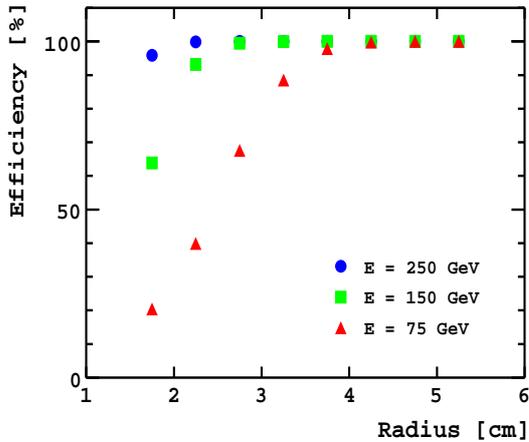
Figure 31: The efficiency to identify an electron of energy 75, 150, 250 GeV as a function of the radius in the BeamCal.
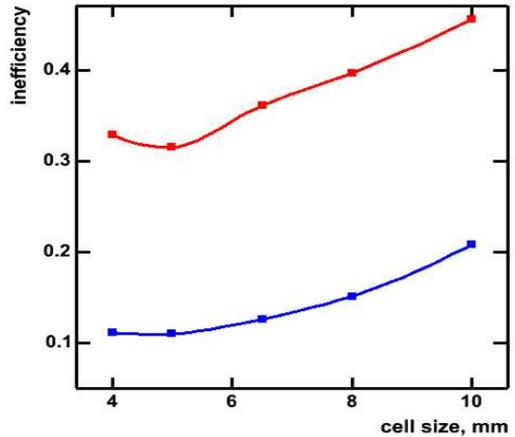

Figure 32: The inefficiency to detect electrons of 200 GeV as a function of the size of the sensor pads. The blue and read curves are obtained for regions of low and high background, respectively.

5.3 Two-photon Background and Stau Search for Different Beam Parameter Configurations and Detector Fields

Using the efficiencies shown in Figure 31 we simulate the process $e^+e^- \rightarrow \tilde{\tau}^+\tilde{\tau}^- \rightarrow \tau^+\chi_0\tau^-\chi_0$ for SUSY parameter settings as described above. After applying all selection cuts except the electron veto 20 stau events are left, while the number of surviving 2-photon background events is about 2.7×10^5. Figure 33 shows the energy and spatial distribution of the electrons originating from the two photon events. Most of these electrons have nearly the beam energy and hit the BeamCal outside the area affected by pairs, though the distribution has tails down to the smallest angles and energies. It is important to notice that the distribution depends on the mass difference between the stau and the neutralino, e.g. if it is larger than 5 GeV the distribution is broader and shifted to larger angles. For each beam parameter set in Table 4 veto efficiencies as shown in Figure 31 are estimated from simulations. These efficiencies were included into the stau search analysis. The number
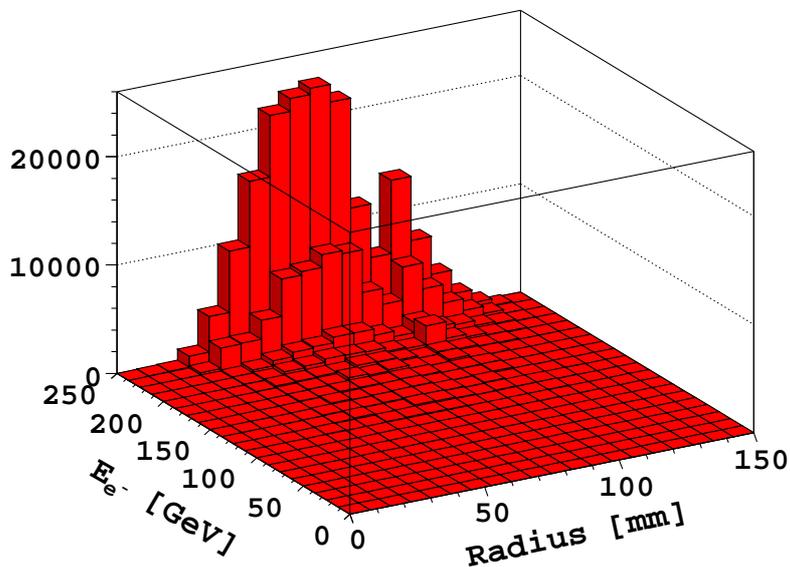
Figure 33: Electron energy and spatial distribution of the 2-photon background events passing all cuts except the electron veto.

of unvetoed 2-photon events for each beam parameter set is listed in Table 6. Results are given for thresholds of 50 and 75 GeV to veto an electron in BeamCal, showing that a relatively low energy cut of 50 GeV improves the signal-to-noise ratio considerably. For the chosen benchmark physics scenario the chances to see stau particles are very good for most of the accelerator designs. Only for the LowP scheme the remnant background dominates the selected event sample. By far the best situation is given for the LowQ scheme.

Energy cut [GeV]	75	50
Nominal	45	5
LowQ	40	0.1
LargeY	50	9
LowP	364	321

Table 6: The number of background events after applying the veto for high energy electrons in the BeamCal. The number of expected stau events is for all cases 20.

The same study was repeated to compare the results for small and large crossing angles. The distribution of depositions from beamstrahlung pairs on the BeamCal is very similar for low and large beam crossing angles provided in the latter case the anti-DID field is used in the detector. For a large beam crossing angle with a DID field the deposited energy, for each of the accelerator parameter sets, is much larger and the shape of the distribution, shown in Figure 34b, is different. Hence we can assume that the BeamCal performance

for small and large crossing angles with anti-DID field are similar. Repeating the study of
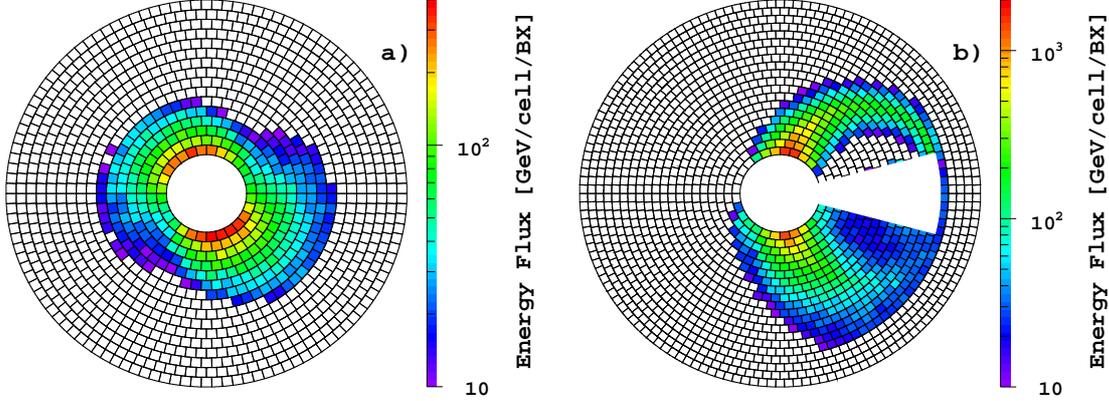

Figure 34: The energy density of beamstrahlung remnants per bunch crossing as a function of position in the $r - \varphi$ plane at the a) 2 mrad and b) 20 mrad with DID field crossing angles.

stau production for a large crossing angle and DID field we found the number of unvetoed 2-photon events remaining in the analysis is 349 compared to 5 events in the case of a small crossing angle. The number of stau events is again 20 in both cases. Hence, for this particular benchmark scenario we would have no chance to see stau production at large crossing angle and a DID field.

5.4   Effective Luminosity Reduction Due to Unidentified Bhabha Events

The Bhabha rate grows very rapidly for decreasing polar angles and becomes large in the BeamCal range. As it is shown above, the identification of high energy electrons becomes inefficient near the beam-pipe. Hence it may happen that only one electron is reconstructed for a Bhabha event. In addition, radiative Bhabha events may have one electron inside and the second outside the BeamCal acceptance region. These Bhabha events fake the signature of a two-photon events, and we would suppress them in the analysis to search e.g for staus, dropping effectively the luminosity available for a certain search experiment.

To estimate this effect, a simulation is done for the crossing angle schemes head-on, 2 mrad and 20 mrad with DID field. The Monte Carlo programs BHLUMI and TEEGG [55] are used for Bhabha event generation[2]

The generated Bhabha events are fully simulated on top of the beamstrahlung depositions and then the reconstruction algorithm for single electron showers is applied.

The number of identified Bhabha events and single electron Bhabha events per bunch crossing in the BeamCal acceptance range is shown as a a function of the calorimeter

---

[2]At very small polar angles BHLUMI is not prepared to simulate radiative Bhabha events properly. We therefore used BHLUMI above a certain polar angle threshold and the TEEGG generator below this threshold.

radius[3] in Figures 35a) and 35b), respectively, for different beam crossing angles. The veto rate due to Bhabha scattering is about 5% for small beam crossing angles and roughly 15% for large crossing angles.
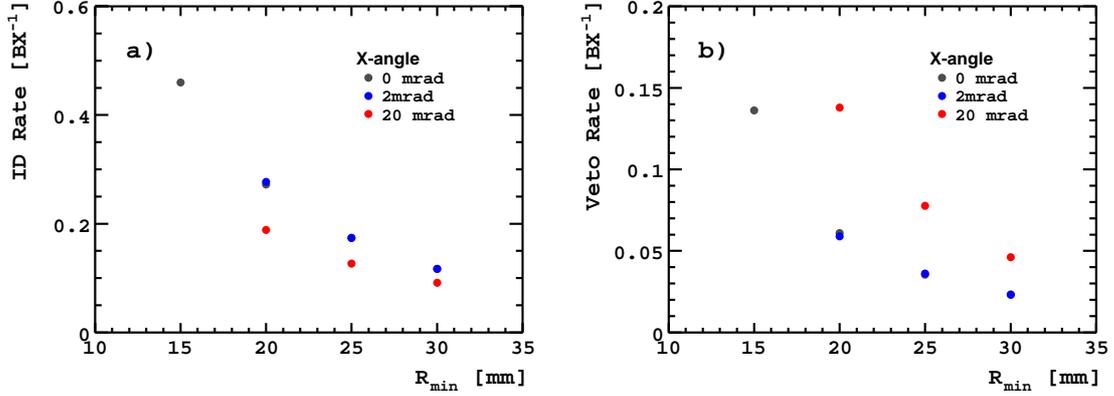

Figure 35: a) Bhabha identification rate and b) Bhabha induced veto rate in the BeamCal as function of the minimal acceptance radius for various crossing angle schemes.

---

[3]These are cumulative distributions, the number of events per bunch-crossing for a certain radius contains all events hitting the calorimeter above this radius.

6   The Gamma Detector - GamCal

The ILC RDR [25] discusses the luminosity feedback system:

2.7.4.2.3 **Luminosity feedback** *Because the luminosity may be extremely sensitive to bunch shape, the maximum luminosity may be achieved when the beams are slightly offset from one another vertically, or with a slight non-zero beam-beam deflection. After the IP position and angle feedbacks have converged, the luminosity feedback varies the position and angle of one beam with respect to the other in small steps to maximize the measured luminosity.*

The luminosity feedback detectors are the BeamCal, which has been described in the previous section in detail, and the GamCal. Both are important systems for the beam diagnosis. The particle bunches in the ILC experience very large electro-magnetic fields shortly before and during the collision, up to $1\,\mathrm{KT}$ effective magnetic field. This causes a large amount of radiation called beamstrahlung. A small fraction of the beamstrahlung gammas convert to an electron-positron pair by the Bethe-Heitler interaction $\gamma e \to eee$. These pairs have an average energy of $\approx 2\,\mathrm{GeV}$ and spiral in the detector magnetic field. About half of the pairs hit the BeamCal detector located just in front of the first quadrupole magnet. The instantaneous production of Bethe-Heitler pairs is given by

$$N_{ee}^{BH} \propto \frac{N_\gamma^0 N^0}{\sigma_x^0 \sigma_y^0},\tag{12}$$

where N^0 denotes the number of electrons for the electron beam and the number positrons for the positron beam, and the o superscript denotes that only the overlapping portion of the beam is to be used in eq. (12). The instantaneous luminosity is given by

$$\mathcal{L} \propto \frac{N_-^0 N_+^0}{\sigma_x^0 \sigma_y^0}\tag{13}$$

The ratio of Bethe-Heitler pairs to beamstrahlung gammas from eq. (12) is

$$\frac{N_{ee}^{BH}}{N_\gamma^0} \propto \frac{N^0}{\sigma_x^0 \sigma_y^0}\tag{14}$$

Eq. (14) is satisfied separately for the left and right beamstrahlung pair (BeamCal) and gamma (GamCal) detectors. Thus we have the information required to evaluate Eq. (13). The LumiCal detector will provide integrated luminosity information from the measurement of Bhabha pairs with statistical accuracy of several percent every minute at the peak luminosity. The BeamCal and GamCal detectors will provide instantaneous luminosity information with a statistical accuracy of several percent for every beam crossing at the peak luminosity. The GamCal detector is located about $10^2\,\mathrm{m}$ downstream of the IP in the extraction beamline. The GamCal team is evaluating several locations: at the end of the E chicane, at the beginning of the P chicane, after the P chicane between the BVEX1G and BVEX2G magnets. The latter looks the most promising as it will not give any in-time background to the E and P detectors.

The above equations do not take into account the smaller cross-section Landau-Lifshitz $ee \rightarrow eeee$ process, etc. We discuss the physics involved and the simulation efforts in much greater detail in [56]. However, our basic conclusion is that the ratio of the produced beamstrahlung pairs to gammas does indeed track luminosity (see Fig. 36 and Fig. 37). One can see that measuring both the beamstrahlung gammas and pairs provides robust, complementary information (see also Fig. 38 and Fig. 39)), which we believe will be very useful in understanding what is actually happening at the IP.
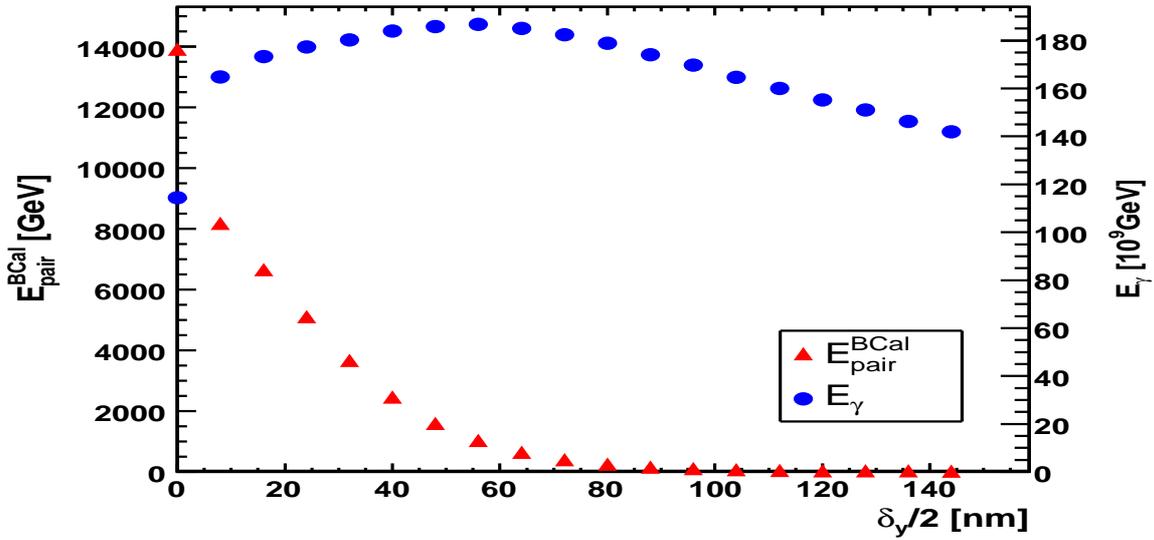
Figure 36: Energy of the gammas (right scale) and the pairs hitting the BeamCal (left scale) per beam crossing as a function of the bunch vertical offset.

As can be seen, the BeamCal and GamCal give complementary and robust information.

At present the FCAL [57] Beam Diagnostics [58, 59] team activities include the following: realistic BeamCal simulations including Bhabha pairs; further studies of tracking the luminosity by varying bunch characteristics such as the horizontal angle, etc.; GamCal detector design and BeamCal readout design.
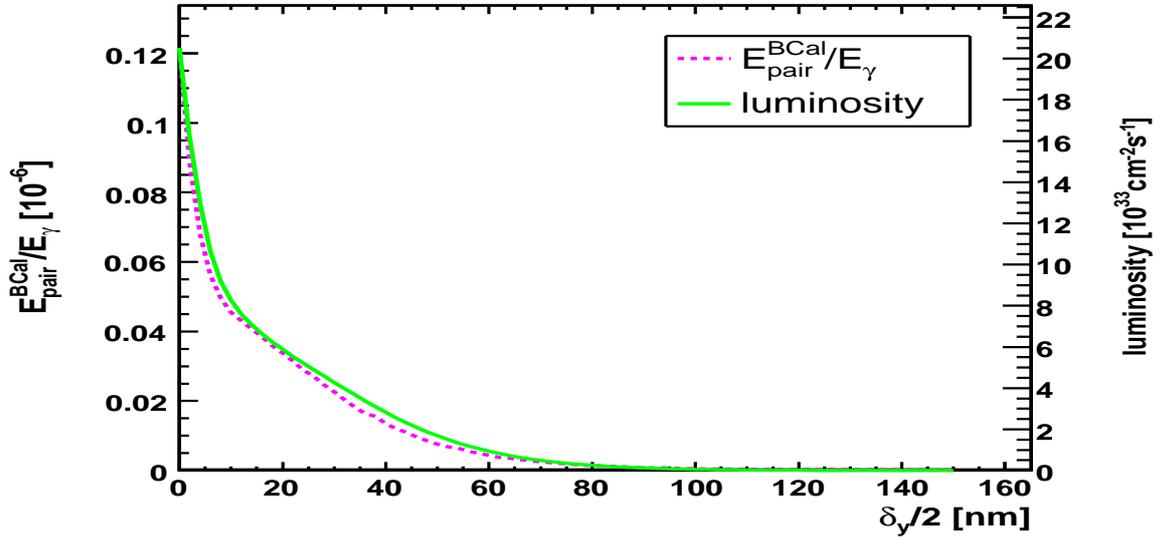
Figure 37: Luminosity (right scale) and the ratio of the pair to gamma energy (left scale) as a function of the bunch vertical offset.
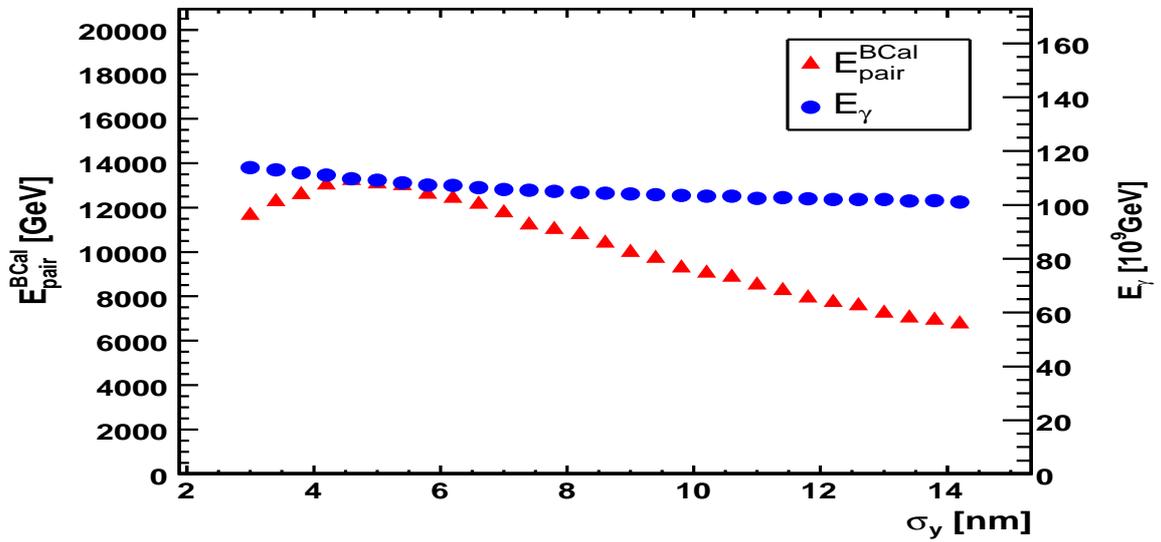

Figure 38: Energy of the gammas (right scale) and the pairs hitting the BeamCal (left scale) per beam crossing as a function of the bunch height (nm).
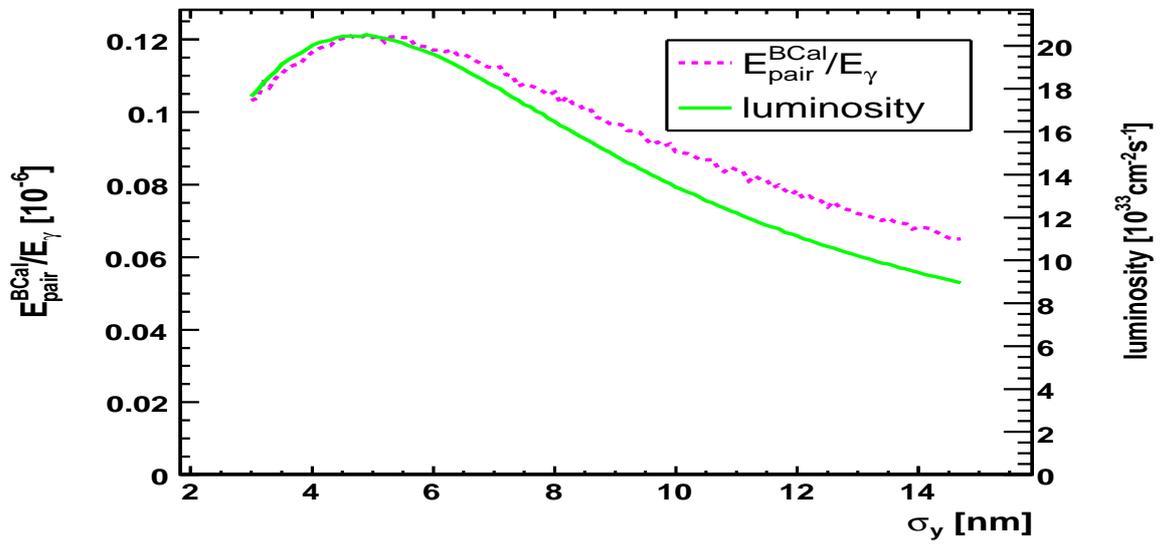
Figure 39: Luminosity (right scale) and the ratio of the pair to gamma energy (left scale) as a function of the bunch bunch height(nm).

6.1 Beamstrahlung Studies at the ILC

With the first observation of beamstrahlung radiation at SLAC [60] a new tool for studying the properties of e^+e^- colliding beams was realized. This tool will be useful in optimizing the beam intersections and in monitoring the status of the beam collisions at the ILC. The ILC will have many more beamstrahlung photons than lower energy colliders - a few times 10^{10}/crossing. Thus, an ambitious program of beam diagnostics via beamstrahlung might be imagined for this accelerator. We are proposing to investigate the gamma calorimeter, GamCal, which will measure the energy, intensity, and spatial distributions of beamstrahlung photons.

The GamCal has two components, both of which utilize the positrons which are pair produced from the beamstrahlung photons hitting a thin foil ($\approx 10^{-4}$ radiation lengths) placed at the entrance to the BVEX2G magnet. This magnet is approximately 180 m from the interaction point (IP) in the beam dump line, and acts as analyzing magnet for the IBS. The apparatus is shown schematically in Fig. 40. The two components, which are described below, are the "Integrated Beamstrahlung Spectrometer" (IBS) Calorimeter and the IBS Camera.

6.2 The IBS Calorimeter

As mentioned above, a thin foil ($\approx 10^{-4}$ radiation lengths) placed at the entrance of BVEX2G will convert a fraction of the beamstrahlung photons to electron positron pairs. The trajectories of these charged particles are deflected by the magnet with the positrons going into a row of detectors as shown in Fig. 40

The detector we envisage is a row of heavy-metal-quartz-plate calorimeter modules, viewed by photo-tubes with quartz windows. They will be radiation hard, which is necessary for detectors in the ILC beam environment, and will be arrayed roughly parallel to the beamstrahlung beam. The configuration of quartz and metal is under study. The principle, however, is that the products of electromagnetic showers in the metal will cause Cerenkov radiation in the quartz which will be observed by the module's photo-tube. Since each module sees a different positron energy, it will be adjusted to have an optimum response for its particular energy.

The signal from a module will be the amount of light above a threshold for that module, recorded by a flash ADC. Since each module is associated with a particular energy positron, the amplitude of light from multiple positrons in a module from an individual machine pulse will reflect the number of positrons in that module at the module's nominal energy. The ambient background is expected to be small since the lowest energy module will be set to respond to positrons with at least 1 GeV of energy. This is also under study.

Preliminary analysis of simulated data indicates that such a device is sensitive to the total beamstrahlung energy and intensity with minimal disturbance of either the beamstrahlung beam or the primary electron beam.

6.3 IBS Camera

Looking at lower energy positrons from the same foil is a device we term an IBS camera. The purpose of this camera is to obtain a two-dimensional image of the beamstrahlung transverse to the beam. Since the camera is about 180 m downstream from the interaction point, the size of the beamstrahlung beam is relatively large. The periphery of beamstrahlung distribution is most sensitive to the parameters describing the interacting beam, so the converting foil is also large, $\pm$ 15 cm horizontally by ±10 cm vertically.

A cartoon of the camera is shown in Fig. 41. The physical camera is a collimator, about 1 m long, penetrated by a square matrix of 1.5 mm holes on 4 mm centers. The holes are filled with quartz rods at the end of the collimator for its last 10 cm. Photodetectors view the rods.

Low energy positrons from the foil are directed to the camera by the magnetic field of the BVEX2G magnet. Each hole in the camera selects particles in a very small momentum range ($\Delta p/p \approx 10^{-3}$) around the central momentum of 615 MeV emanating from a small region of the foil. Those positrons that penetrate the holes over their full length pass through the quartz rods, and their Cerenkov light is observed by the photodetectors. A discrimination level is placed on the light from the rods to insure that the positrons pass through a significant length of the rods. The purpose is to verify that the particles which made the light were the desired 615 MeV positrons, and to discriminate against low energy background.

We have simulated the observed distributions in the camera resulting from beamstrahlung at the 180 m point in the beam line. The photons were generated by the GUINEA PIG simulation program, and were converted to e^+e^- pairs and analyzed by GEANT. We display in Fig. 42 various distributions as seen by the camera for head-on e^+e^- collisions at the IP. In Fig. 43 we show the same plots but for a vertical offset of the beams of 3 std. (≈ 20 nm). As on can see, the effect on the distribution is quite pronounced.

In spite of the restricted phase space acceptance of the camera, having a rate of about 2×10^{10} photons per bunch and 3000 bunches per train allows us to accumulate the data shown in Fig. 42 or Fig. 43 in about one train.

6.4 Backgrounds

One might ask if putting a foil in the electron and beamstrahlung beam might not produce a prohibitive background. The first source of such background might be the bremsstrahlung that occurs from the electron beam passing through the foil. The beamstrahlung beam power is of the order of MW, and the bremsstrahlung power from the foil is of the order of KW. These extra photons also have angular distributions that keep their trajectories within the envelope of the beamstrahlung beam. Thus, the background from the extra photons is orders of magnitude smaller than that which might be expected from the beam itself.

What about Landau-Lifshitz positrons produced when the electron beam passes through the foil? As pointed out by Morse [61], the number of positrons so produced is about 6% of those produced per photon from beamstrahlung conversion. Since there are about 1.5

times as many beamstrahlung photons as electrons in the beam, the fraction of positrons from beam electrons is $\approx 4\%$. But these positrons will be concentrated at the center of the beam, and as was pointed out above, the sensitivity to variations of collision parameters occurs at the periphery of the beamstrahlung beam. Therefore we see no problem with this background.

The photoproduction and electroproduction of hadrons [61] by the beam passing through the foil was also minimal compared with pair production.

The one background that we have yet to address is the ambient background due to synchrotron radiation and other beamline causes. It is expected that this will produce rather low energy photons, and the design of the IBS is to respond to higher energy particles. Due to the time structure and intensity of the beam, however, this background may be problematical.
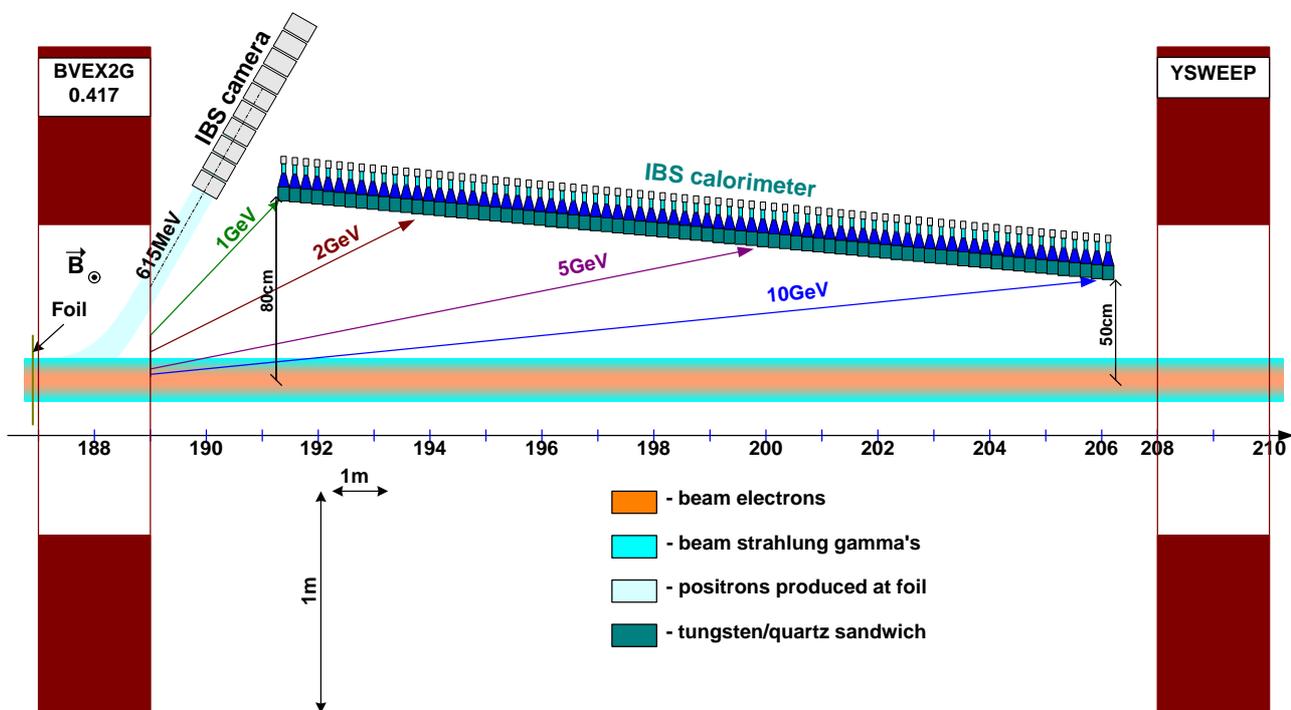
Figure 40: Schematic concept drawing of the Integrated Beamstrahlung Spectrometer (IBS)

Beam strahlung camera

1m

2m

A

- Beam strahlung Gammas

- positrons produced at foil

- Magnet BVEX2G

- tungsten collimator

View A
(the part of detector)
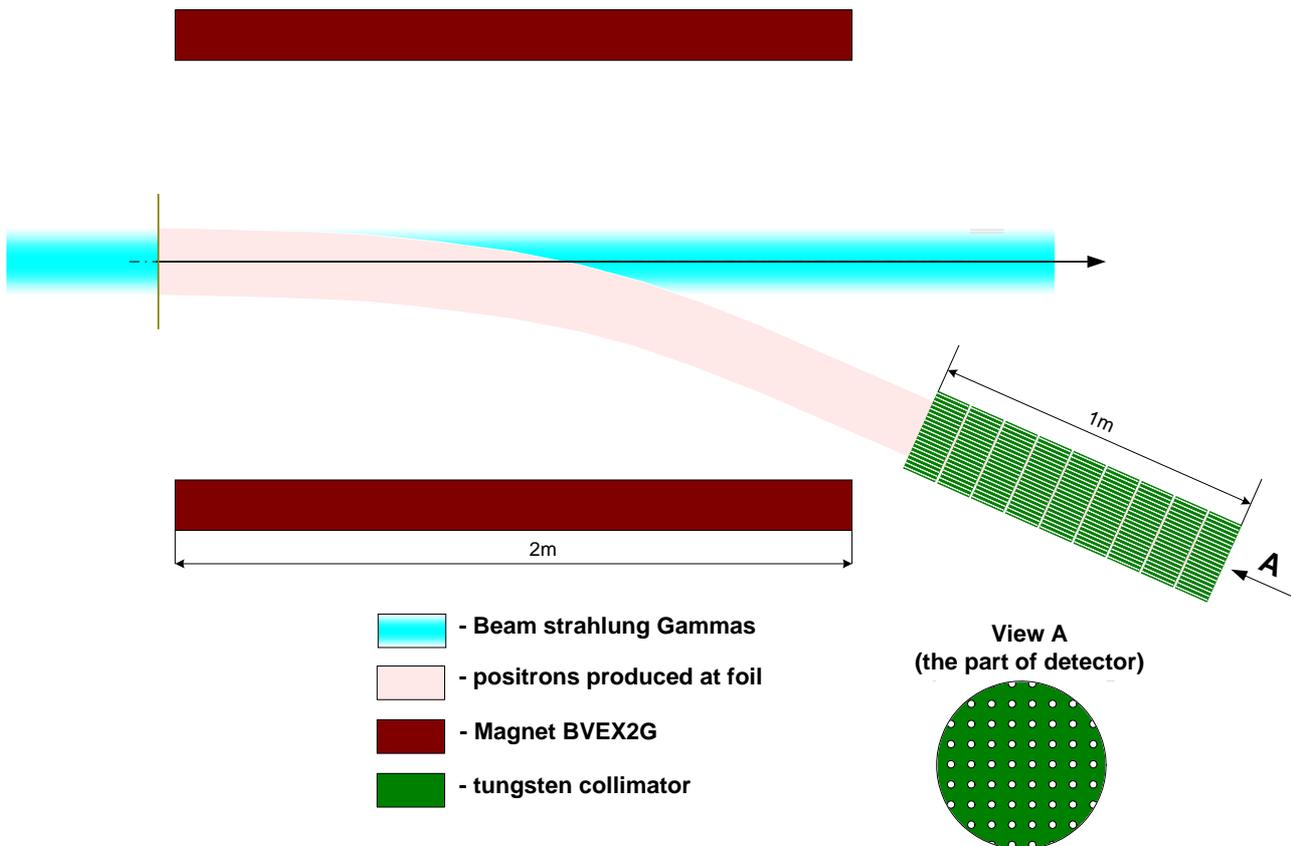
Figure 41: Schematic concept drawing of the IBS camera. The inset shows a sample of the matrix of holes.

48

photon_00.dat
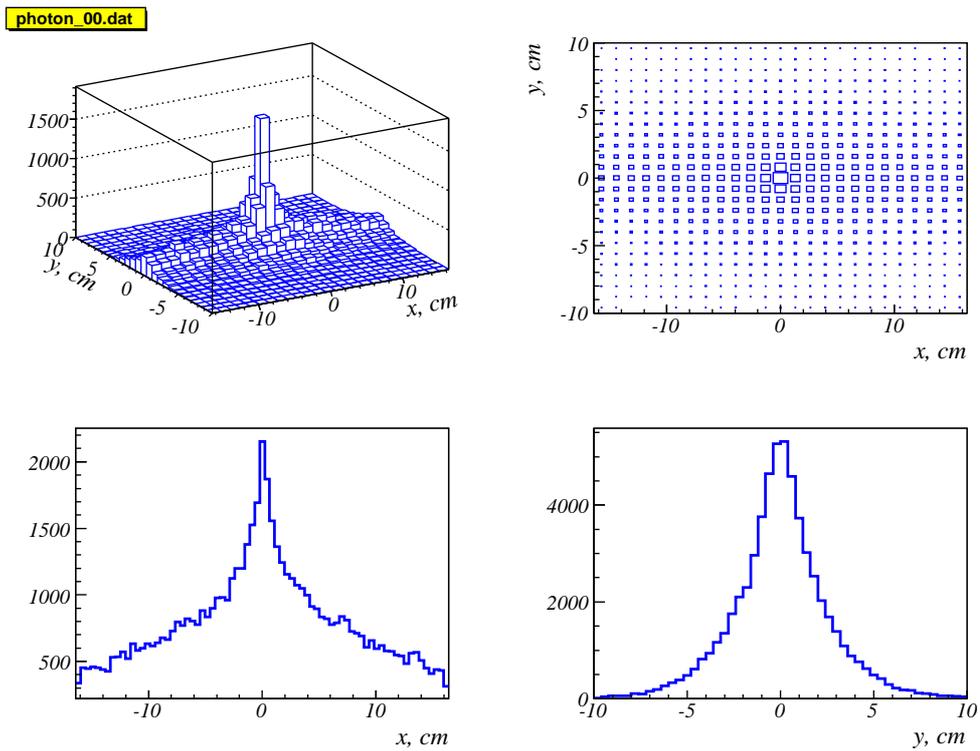
Figure 42: Distributions as seen by the IBS camera from head-on collisions at the IP. Upper left is a plot of positron intensity versus horizontal (x) and vertical (y) directions transverse to the beamstrahlung beam. Upper right is the the same as seen in the $x - y$ plane. Lower left and right are projected intensity distributions in x and y, respectively.
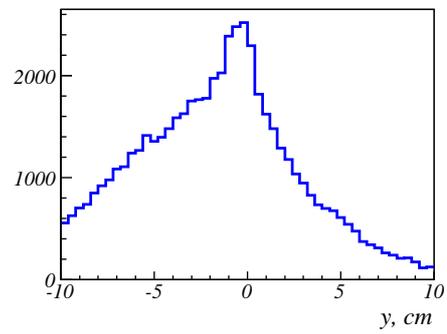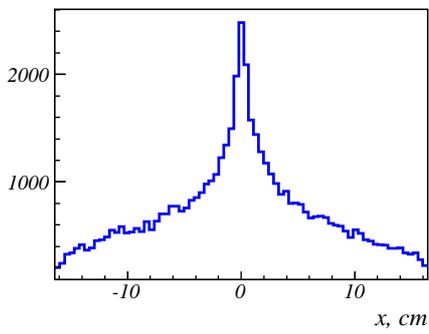
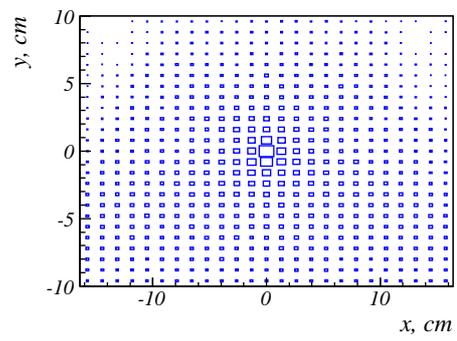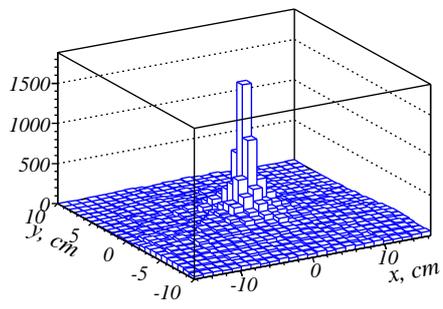Figure 43: Same as Fig. 42 but for a vertical offset of the colliding beams of 35 nm.

50

7 Sensor Development

The forward electromagnetic sampling calorimeters (BeamCal and LumiCal) consist of several layers of absorber material (tungsten) interleaved with sensor planes taking a 'sample' of the developing electromagnetic shower at their actual position. This section of the report deals with the development of sensor materials which have to fulfill the demanding requirements.

7.1 Requirements

Sensors for calorimeters must give a stable and homogeneous response over their full area and lifetime. Otherwise calibration / recalibration becomes complicated. The luminosity calorimeter will not suffer from high irradiation. The sensors of the LumiCal must have precise and stable mechanical positions as shown in Sec. 2. Their segmentation should be fine enough to provide for the needed spatial resolution.

As mentioned in Sec. 4, the BeamCal will be hit by an enormous amount of electrons from beamstrahlung. This will sum up to an irradiation dose at inner radii of several MGy per year (see Fig. 44(a)). Those electrons introduce a permanent background with a relatively low energy per particle (see Fig. 44(b)). The sensors must be able to detect high energetic electrons on top of this background. The response should be fast enough to distinguish between subsequent bunches because we want to derive steering signals for the control of the accelerator itself.
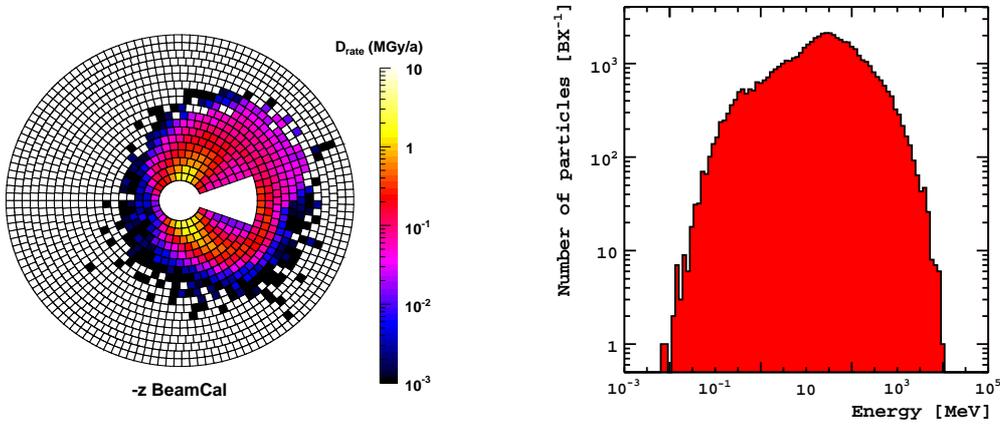
(a) Radiation load as simulated for LDC for 14 mrad, DID field and 100 % running time per year.

(b) Energy spectrum of particles contributing to the energy deposition in BeamCal in a depth of $2\,X_0$.

Figure 44: Radiation load (a) and energy distribution (b) of beamstrahlung hitting the BeamCal.

7.2 Different Materials under Investigation

For the LumiCal, planar single-sided silicon is the material of choice. It can be structured in the desired way, and it also allows for a high mechanical precision at large areas. Radiation damage will not be an issue. For details on the design see also Sec. 3.7.

For the BeamCal, a radiation-hard sensor material must be found. Currently so-called radiation hard silicon is able to withstand irradiation up to a level of less than one tenth of the expected value. The developments of the near future will probably still improve this value. Therefore we will carefully observe the development and investigate the material. Additionally, silicon will serve as reference for all our measurements.

Polycrystalline diamonds (grown in chemical vapor deposition - CVD) are already in use as sensor material in environments with high irradiation doses. All known applications use only small area sensors (a few cm^2). We investigate such sensors as well. The goal is to develop sensors with a sufficiently large area while maintaining the necessary homogeneity.

Single crystal diamonds avoid disadvantages of the polycrystalline material. Currently they can be produced only with small dimensions since they are grown on a single crystal substrate. They are very expensive. We follow the development and investigate small samples to understand material properties.

Gallium arsenide (GaAs) is investigated as another alternative material. Its band gap is much larger compared to silicon, thus it is promising to be more radiation tolerant.

Out of a collaboration with the Technical University Cottbus we are able to measure samples of silicon carbide material which is widely used in applications in power electronics. Similar to GaAs it features a wide band gap.

7.3 Static Measurements

For all samples, measurements of current and capacitance as a function of voltage are performed. Thus changes of material properties can be monitored.

7.4 Measurement of Charge Collection Efficiency

For all samples the charge collection efficiency is determined. A Sr-90 source with collimator and filter is used to generate electrons behaving as minimal ionizing particles (MIPs). A scintillator below the sample triggers the measurement. Only electrons passing the sample and the scintillator are used for the spectroscopic measurement.

The amplitude spectra gained with this setup are used to determine the ratio of charge generated and expected charge: charge collection efficiency CCE (if normalized to the thickness of the sample: charge collection distance CCD).

7.5 Linearity Measurements

We investigated the linearity of (especially) pCVD sensors in a hadron beam of $5\,GeV$ (at CERN, Proton Synchrotron PS). The sensors were placed in a light-tight box which was followed downstream the beamline by a scintillator (read out by two photomultipliers). The scintillator served as trigger and as reference detector for the beam intensity. Results are

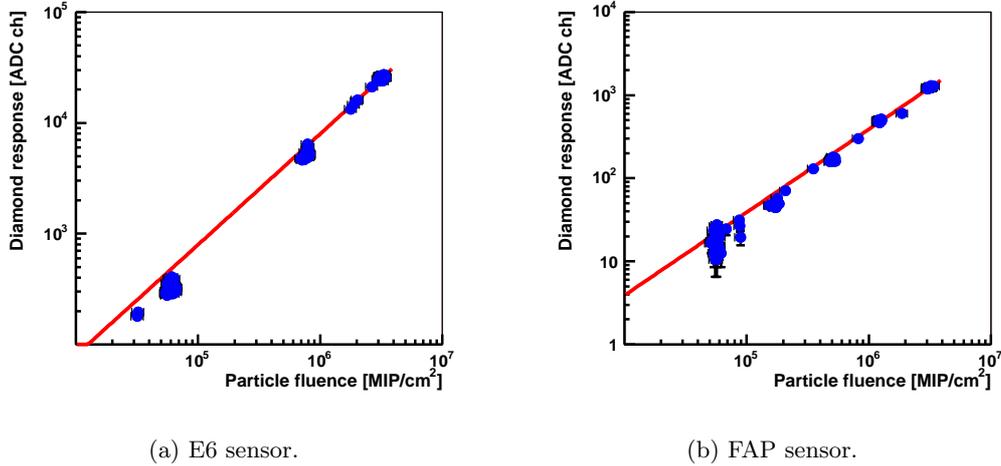shown in Fig. 45. The setup was calibrated with an absolute fluence calibration provided by CERN.

(a) E6 sensor.

(b) FAP sensor.

Figure 45: Signal versus fluence.

7.6 Electromagnetic Irradiation with High Doses

At a monochromatic electron beam (10 MeV) of the S-DALINAC (Technical University of Darmstadt) different samples were irradiated [S4]. The setup used is shown in Fig. 46. The electron beam (from the right side) is collimated to a shape that it irradiates the sample (inside the box) only. The electrons passing through the sample then hit a Faraday Cup (copper) used as beam stopper. The charge collected in the Faraday Cup exactly represents the current through the sample and thus the dose acquired. With currents varying between 10 nA and 100 nA we achieved dose rates from 59 kGy/h to 590 kGy/h.

7.7 Silicon

As a first step, we investigated silicon-pad sensors produced as test structures on the same wafer with silicon sensors for the H1 experiment (HERA, DESY). These pad structures had the same size compared to our pCVD material (1 cm^2). Due to the original purpose, their technology represents a level of 15 years ago.

Initially those sensors behaved absolutely predictable. Together with pCVD sensor samples they were irradiated (see above). It was found that silicon sensors made with such a "standard technology" withstand only a dose of a few ten kGy (10 MeV electrons). Results are shown in Fig. 47. Future investigations will concentrate on the dedicated radiation-hard material. The Brookhaven Lab promised to develop prototypes. Depending on the results we will design a prototype sensor for the BeamCal.
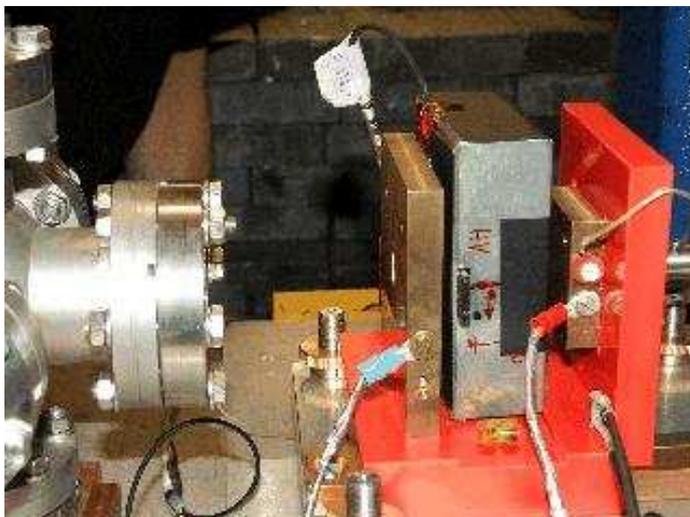
Figure 46: Setup for irradiation test beam.

Prototypes of sensors for the LumiCal are currently being designed and manufactured by our collaborators (Cracow, Prague).

7.8   PCVD Diamond

The development of appropriate pCVD diamond sensors follows two independent branches:

A) We bought samples from the company Element Six (leading manufacturer, delivers "detector grade" pCVD diamond sensors). Details of the production process are not communicated. The samples were metalized and structured (4 pads, see Fig. 48).

B) The Fraunhofer Institute for Applied Physics (FAP, Freiburg i. Breisgau) produced in collaboration with us sensors from their production line for optical grade pCVD material. The standard production is on 4" wafers (100 mm diameter), 6" are possible (150 mm diameter). The sensors were cut out of the wafer (laser cut). Then the surfaces of the samples were grinded and polished.

The surface treatment is especially important for the substrate side of the material because the growth starts with small crystallites still containing impurities (graphite, silicon from the substrate). Finally the sensors were metalized.

We measured the static behavior (current versus voltage - I/V, examples in Fig. 49) and the charge collection efficiency CCE of all sensors (examples in Fig. 49). Some sensors of both manufacturers were irradiated in a 10 MeV electron beam. Measurement of the current (particle flow) through the sensor allowed for a definition of the absorbed dose [62]. In-between several irradiation intervals, we determined the charge collection efficiency as a measure of a possible change in performance.

Most samples of the pCVD material investigated have very low leakage currents (few pA up to few nA). The charge collection efficiency strongly depends on the manufacturing process and differs from sample to sample, independent of whether they originated from
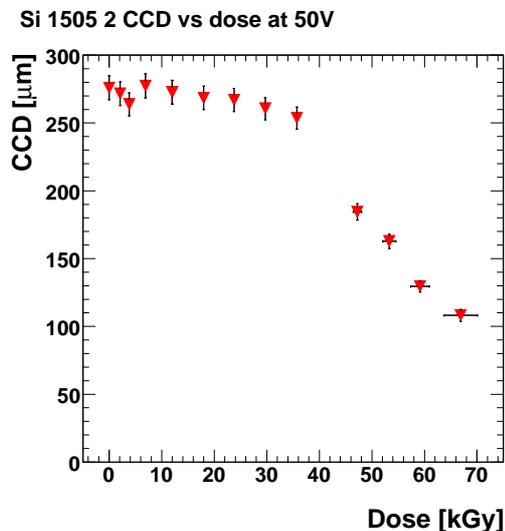
Figure 47: Degradation of silicon.

the same wafer or not. Samples from Element Six generally show higher charge collection efficiencies. This points to a better understanding and control of the manufacturing process. Our samples did not reach charge collection efficiencies higher than about 25 %. The sensors degrade with increasing irradiation doses. This degradation depends on the dose, dose rate and biasing. The behavior has to be studied in more detail. Measured curves for both types of pCVD sensors are shown in Fig. 50.

We studied different samples with methods used in solid state physics (Raman spectroscopy). From the Raman spectra we estimated the content of impurities, especially nitrogen. With our current level of understanding we could not correlate characteristic shapes of the Raman spectra with specific electrical properties of the sample. A high content of nitrogen seems to lower the charge collection efficiency.

The current material does not fulfill the requirements of an electromagnetic calorimeter (stability and degradation of signal (CCE), homogeneity in the plane). The radiation hardness will probably be sufficient. As long as there is no superior candidate for the sensor material we will continue with research on pCVD sensors.

7.9 SCVD Diamond

We investigated one sample of a single crystal diamond sensor (sCVD). It was produced by Element Six and has an active area of three millimeters in diameter. The leakage current is very low (below one nA). The charge collection efficiency reaches already 100 % at a rather low electric field applied (0.1 V/μm compared to about 1V/μm for the pCVD for saturation of CCE, see also Fig. 51). To avoid a possible destruction of this sensor during irradiation we did not yet investigate the radiation tolerance.
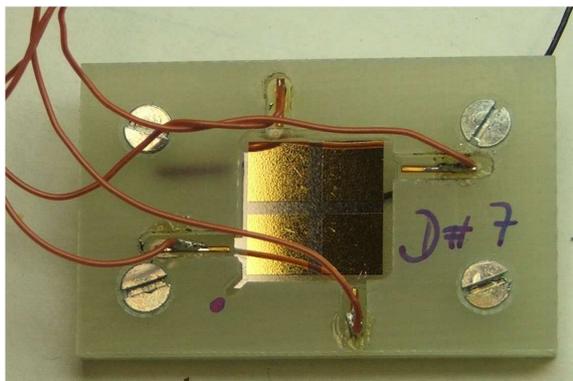
Figure 48: Sample of pCVD diamond with four pads.

The described sensor is currently used as a beam monitor in the ZEUS experiment (HERA, DESY). There we measure a clear correlation of the sCVD diamond signal to the beams in HERA (current, background etc., see also Fig. 52).

Depending on the result of the measurement of the radiation hardness, sCVD sensors seem to be ideal candidates for sensors in calorimeters. An economic production of such sensor material is currently not possible.

7.10 GaAs

A small piece of GaAs sensor material was investigated. The static behavior shows low leakage currents. The charge collection efficiency grows with rising electric field and does not reach 100 %. We stopped the measurement at about $1V/\mu m$ to avoid destruction due to increasing power dissipation (leakage current). One of our collaborators (JINR Dubna, Russia) produced a completely structured GaAs sensor (Fig. 53(a)). This sensor is currently under investigation. First results are shown in Fig. 53(b). The current versus voltage (I/V) measurements show a uniform behavior over the whole area of the sensor. As a next step we will measure charge collection efficiencies and radiation tolerance. For a calorimetric application it is problematic that during our measurements the CCE did not reach a saturation. This has to be investigated in more detail.

7.11 SiC

We investigated a piece of silicon carbide material delivered by the Technical University of Cottbus. It showed an asymmetric behavior already at very low voltages (Fig. 54). The high leakage current points to a large number of free charge carriers, which cause signal charge generated immediately to be compensated. We could not find a signal from particles. It was appointed that material with a much higher resistivity will be produced and then investigated.
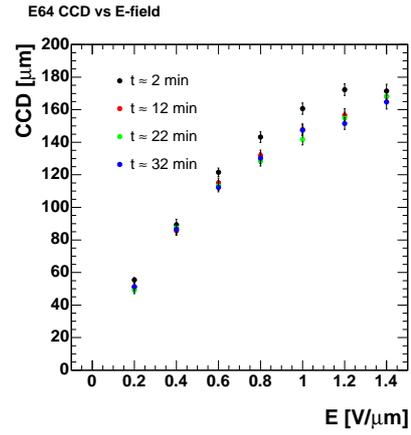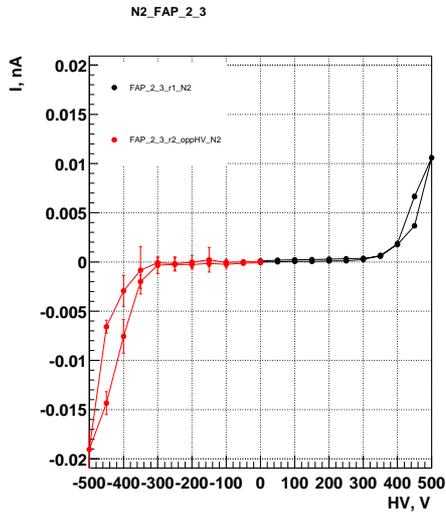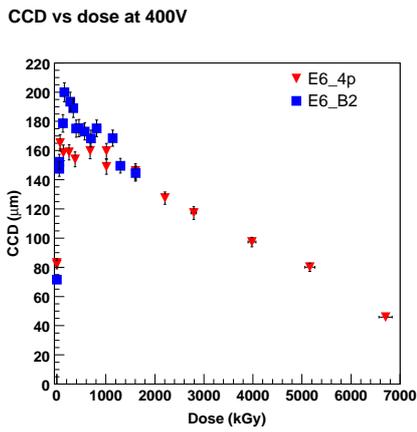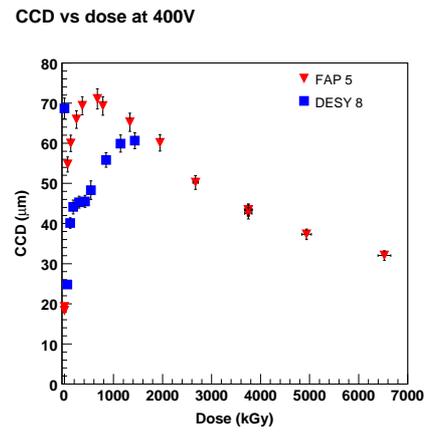
Figure 49: I/V and Charge collection efficiency versus electric field.

(a) E6 sensors.

(b) FAP sensors.

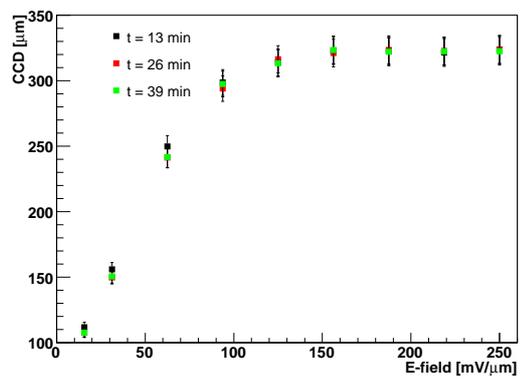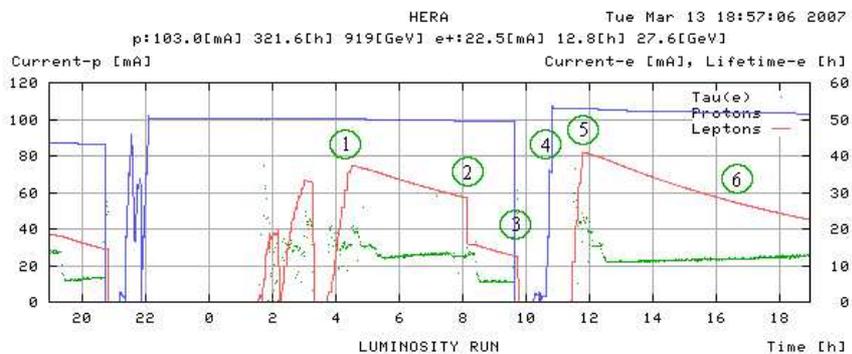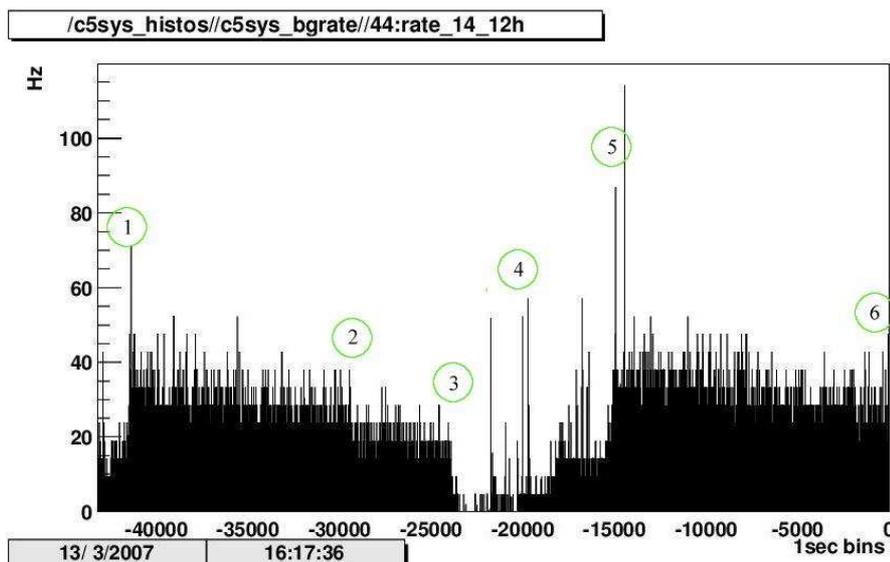Figure 50: Charge collection distance versus accumulated dose.

Figure 51: Charge collection distance of sCVD diamond versus electric field.

(a) HERA beam condition history of 24 h.

(b) SCVD Diamond beam monitor count rate during 12 h out of the period covered above.

Figure 52: Correlation between HERA beam conditions and beam monitor counts.
1: Positron injection and acceleration. Proton beam already present.
2: Positron beam current decrease.
3: Both beams dumped.
4: Proton injection and acceleration.
5: Positron injection and acceleration.
5-6: Luminosity run with usual slow decrease of the positron current. End of recording.
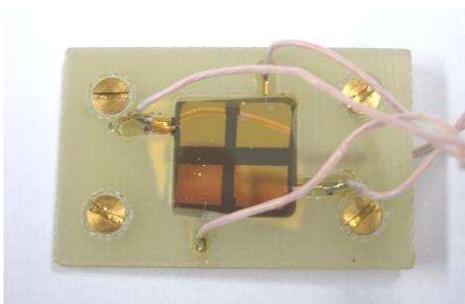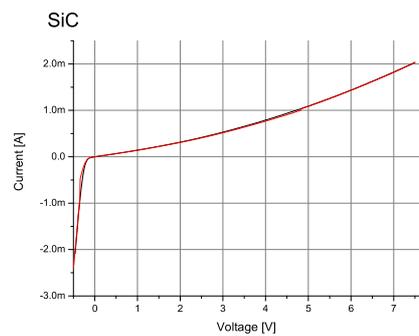
59

(a) Photograph of the prototype.
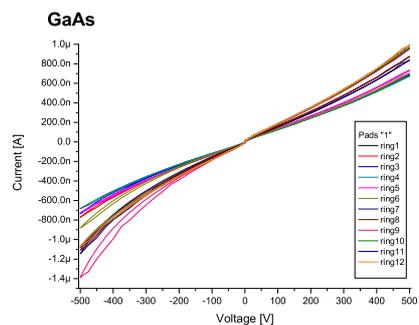
(b) Current versus voltage measurement of the prototype.

Figure 53: Prototype of a full scale GaAs sensor for the BeamCal.

(a) Photograph of the prototype.

(b) Current versus voltage measurement of the prototype.

Figure 54: Prototype of SiC sensor.

8 Readout Electronics for the FCAL Systems

8.1 Readout of the LumiCal

The project of LumiCal readout electronics depends on several assumptions concerning the detector architecture. At the present development stage it is assumed that the LumiCal detector is built of 30 layers of 300 μm thick DC-coupled silicon sensors and each layer is divided into 48 azimuthal sectors. Each sector, with the inner radius of 8 cm and the outer of 35 cm, is segmented into 96 radial strips with a constant pitch. The LumiCal should work in two modes: the physics mode and the test mode. In the physics mode, the detector should be sensitive to electromagnetic showers with high energy deposition (up to about 15 pC of charge) in a single sensor. In the test mode, it should detect the signals from relativistic muons, i.e. it should be able to register minimum ionizing particles (1 MIP$\sim$4 fC). Because of the very high expected occupancy, the front-end electronics should resolve signals from particles in subsequent beam bunches, i.e. within a time spacing of about 360 ns. The requirements on the power dissipation of this front-end electronics can be seen strongly relaxed: the power will be totally or partly switched off in the periods between the bunch trains.

From the specifications above, the general concept of the readout electronics was outlined as shown in Fig. 55. The main blocks of the signal chain are: front-end electronics, A/D conversion plus zero suppression and data concentrator with optical driver. For each layer of the LumiCal detector, 2 to 4 copies of the readout chain presented in Fig. 55 are needed. The actual number will depend on the optical link throughput. The first two readout blocks in Fig. 55, i.e. the front-end and ADC, need to be designed as a dedicated full custom ASIC. In the following, the designs of different blocks are discussed and results of simulations are presented. The data concentrator and optical driver block will be studied at a further development stage. The design work on the discussed ASICs is underway and the first prototypes will soon (August 2007) be produced in the AMS 0.35μm technology through the Europractice service.

8.1.1 Fan-out of the Sensors

To read out charge signals from the sensor pads we have designed a fan-out covering two sensor sectors, as described in Sec. 3.7. Aluminum traces of 75 μm width on a thin (200-300 μm) glass substrate will feed the signal to the outer radius of the detector where the charge sensitive preamplifiers will be placed. To avoid crosstalks between adjacent channels we foresee grounded lines between two signal lines. The distance between signal and ground traces is 125 μm. A simplified cross section of the fan-out structure is shown in Fig. 56.

The capacitance of the signal lines will be about 0.7 pF/cm. The capacitances of the different pads coupled to the inputs of the preamplifiers will be between 30 pF to 45 pF in total. In Fig. 57 all important dimensions of pads, traces and space between traces are shown.
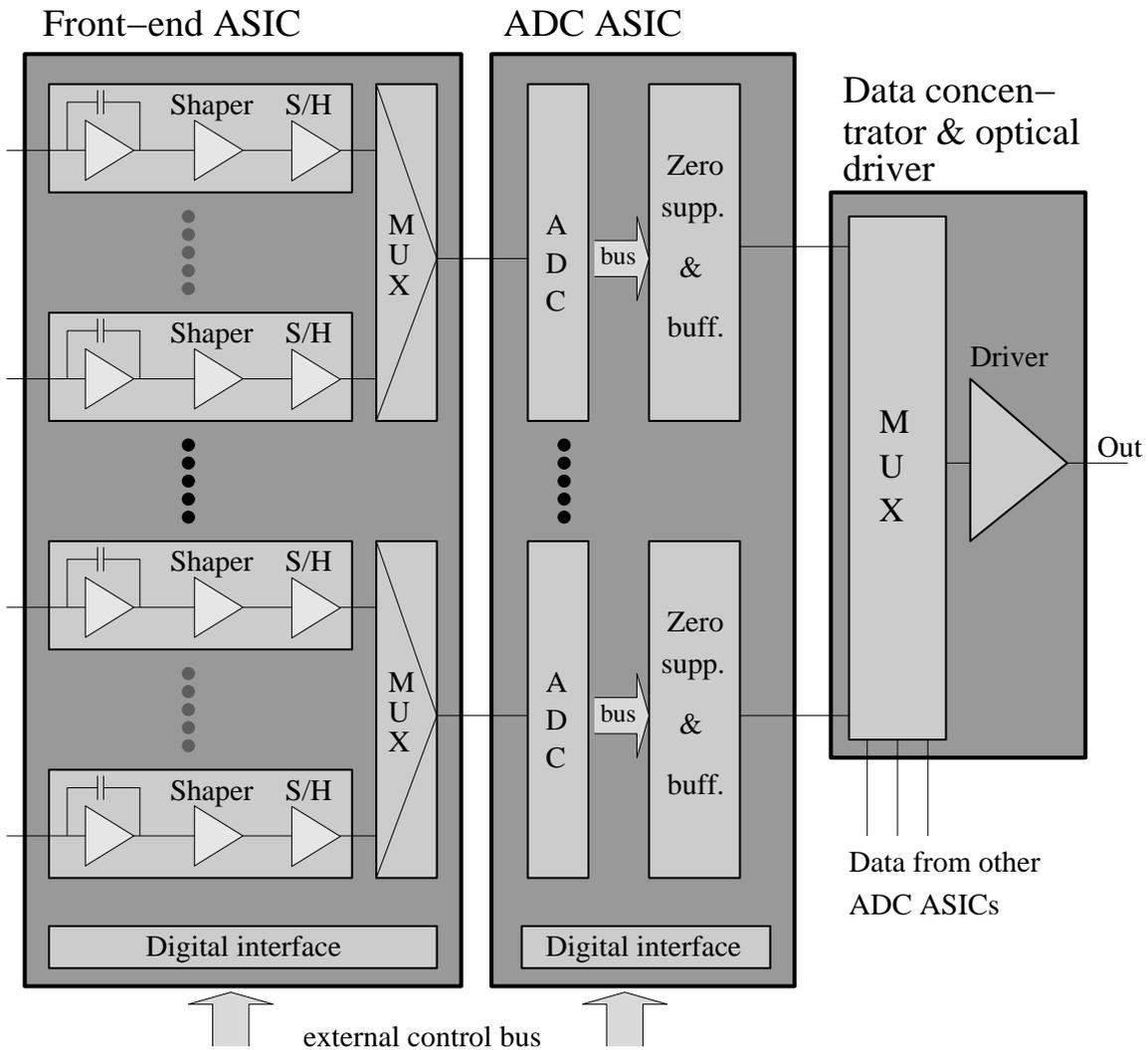
Figure 55: Block diagram of the LumiCal readout electronics.

8.1.2 Front-end Electronics for the LumiCal

The preamplifiers of the front-end electronics collect signals from the silicon detectors. The signals are amplified and shaped to obtain the desired signal to noise ratio. Finally their amplitudes are sampled and stored. These stored values are sent to the A/D conversion block. The described operations are performed in parallel for all channels of the front-end ASIC. The front-end electronics for the LumiCal needs to cope with a wide range of input capacitance (from 10 pF to 100 pF) and with a wide range of input charge (from 2 fC to 15 pC). The low noise requirements are driven by a test mode operation, where a signal to noise ratio of about 10 for MIPs, should be also reached for the largest sensor capacitances. At the present stage, the power dissipation per channel is restricted to 10 mW. In order to fulfill the requirements for low noise operation, wide dynamic range and
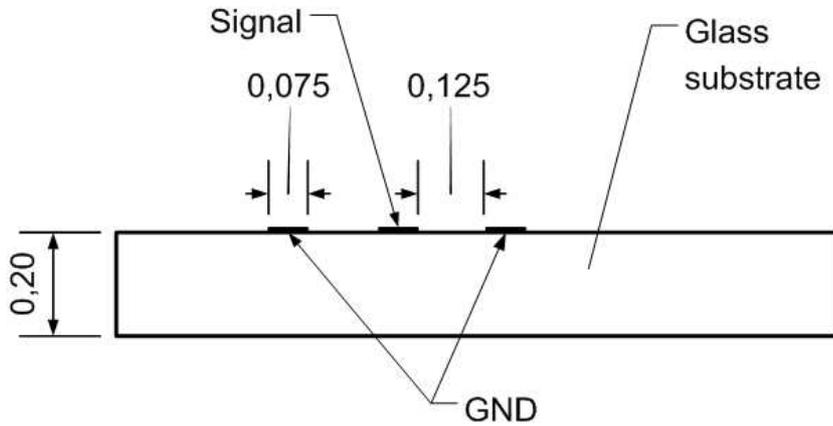
Figure 56: The cross section of the fan-out (all dimensions in mm).

a wide range of input capacitance, a charge sensitive preamplifier configuration was chosen. Two architectures of a front-end using this configuration are currently being studied: one with continuous pulse shaping and one based on a switched reset design. Both architectures and their simulation results are discussed below. The sample and hold circuit (S/H) and the following multiplexer circuit (MUX) are not discussed here since they will be implemented in the next design step.

Front-end with Continuous Pulse Shaping   Each front-end channel is built from the preamplifier, a pole-zero cancellation circuit (PZC) and a shaper, as shown in Fig. 58. The preamplifier integrates the signal charge from the sensor on the feedback capacitance. The PZC circuit is necessary to improve high input rate performance. To optimize the signal to noise ratio and the high speed performance, a pseudo-gaussian shaper follows. It features a peaking time of about 70 ns. Because of the large input signal range, a variable gain is implemented in the preamplifier as well as in the shaper circuit. The gain control is realized with switches in the feedback, allowing for switching between the low gain "physics" mode and the high gain "test" mode. The transfer function of the circuit in Fig. 58 is equivalent to a standard CR-RC first-order shaping. Both circuits are designed as folded cascodes with active loads followed by buffers, as shown in Fig. 59.

The front-end will be designed as a multichannel ASIC. In order to match the detector segmentation, a single ASIC will contain 32, 48 or 64 channels. Such segmentation will allow for either 3 (2) ASICs per 96 radial strips in a single sector or 3 ASICs per pair of sectors. The final choice of segmentation will depend mainly on the power dissipation of a single ASIC.
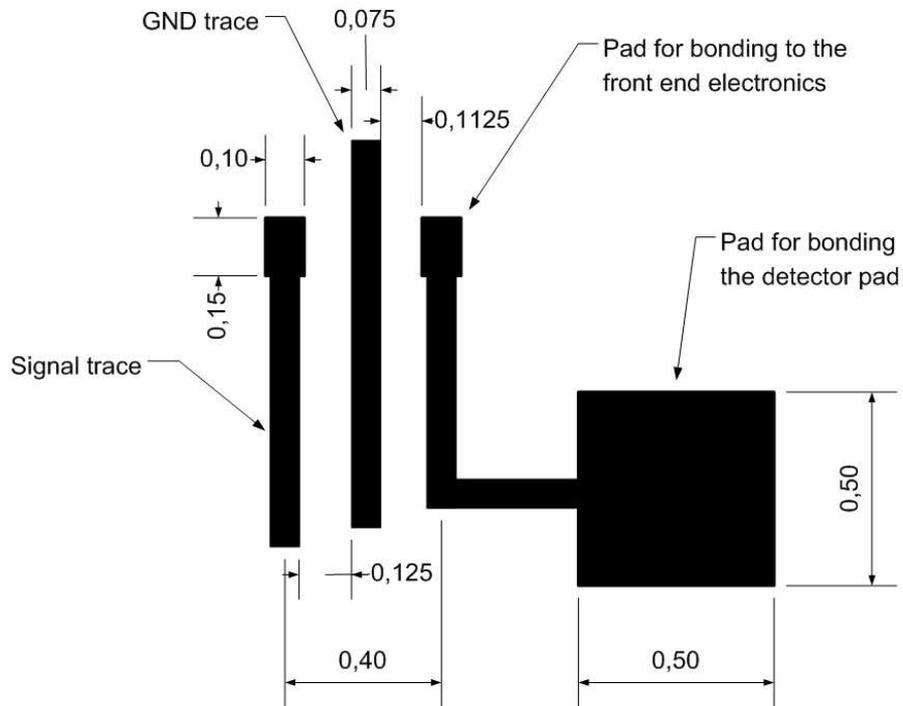
Figure 57: Detailed view of pads and signal traces of the fan-out (all dimensions in mm).
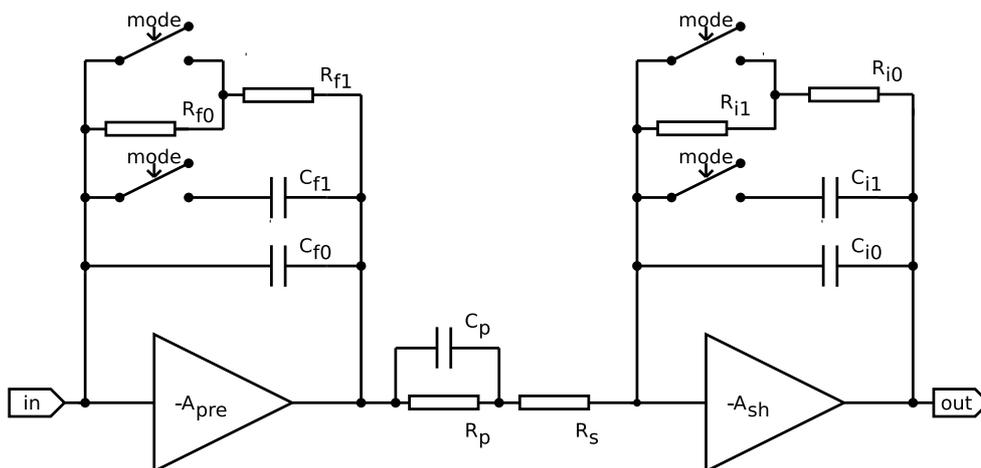

Figure 58: Schematic of preamplifier, PZC and shaper. Switches set to test mode.
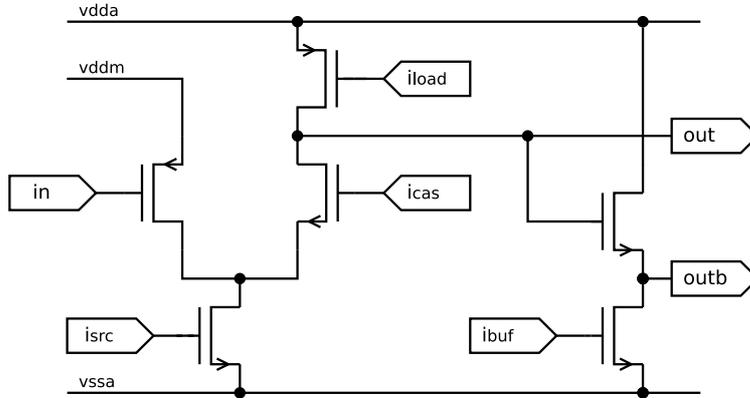
Figure 59: Schematic of folded cascode and buffer circuit.

The simulations of the front-end were done using the *Cadence* package with *Hspice* and *Spectre* simulators. Typical simulated responses for sensor capacitances in the range of 10 pF to 100 pF are shown in Fig. 60 for the test mode (mode0) and for the physics mode (mode1). In the test mode, amplitude and peaking time depend slightly on the
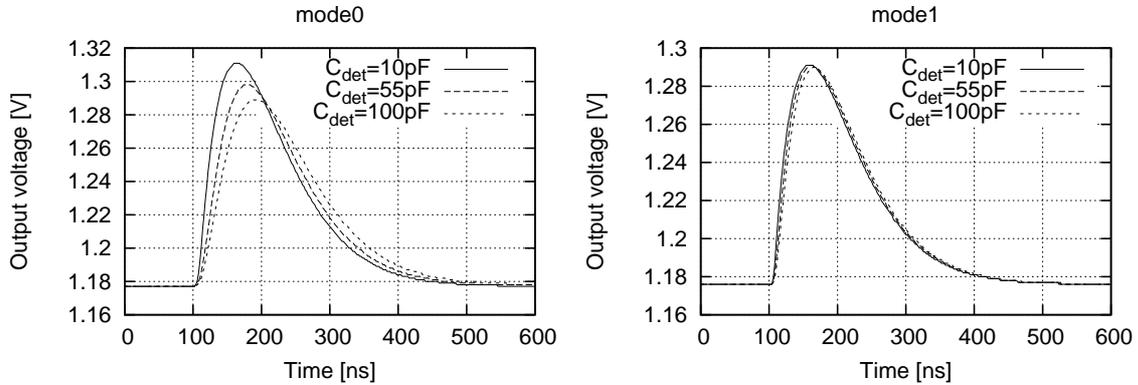

Figure 60: Example of shaper output in test mode for 10fC input charge (mode0) and in physics mode for 1pC input charge (mode1).

input capacitance. In test mode, where the preamplifier's feedback capacitance C_f is small ($\sim 400\,\text{fF}$), the ratio of the detector capacitance C_{det} to the effective input capacitance $C_{eff} \simeq A_{pre} \cdot C_f$ is not negligible anymore since the preamplifier gain is below 1000 while the detector capacitance reaches 100 pF. In this case a part of the charge is lost on the detector capacitance and the preamplifier cannot be considered as a purely charge-sensitive one. In physics mode, when the feedback capacitance is larger (~ 10 pF), the ratio mentioned above may be neglected and the preamplifier behaves charge-sensitive. Such a case is presented in Fig. 60 (mode1) where almost no dependence on the input capacitance can be
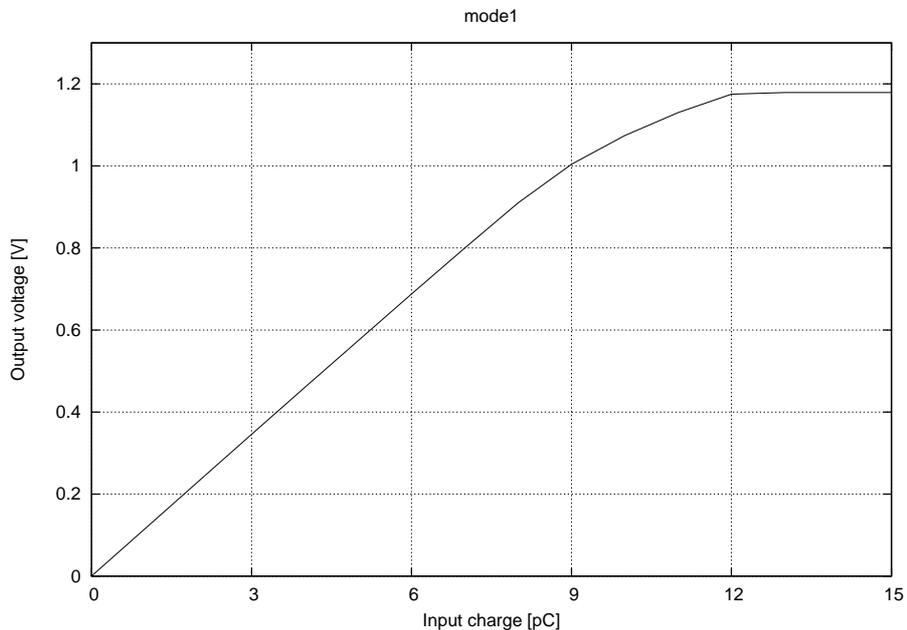
noticed.

Figure 61: Example of front-end output amplitude vs input charge.

In Fig. 61 the amplitude of front-end response versus input charge is shown for "physics" mode. The circuit is linear up to about 7 pC and saturates for higher input charges.

Switched-Reset Front-end   The preamplifier with a feedback reset is a very attractive configuration because it does not need a shaper and it has a large dynamic range. Therefore a charge-sensitive configuration equipped with a reset switch, as shown in Fig. 62, is also investigated. The preamplifier is designed as a folded cascode. To allow for a variable gain, different feedback capacitances are implemented. The test mode configuration is obtained using the smallest capacitance C_{f0}.

Typical front-end responses for different sensor capacitances are shown in Fig. 63 for the test mode (mode0) and for the physics mode (mode1). In all cases the signal risetime is below 300 ns. Since the simulated reset time of the preamplifier never exceeds 40 ns, the full cycle of pulse response and reset can be kept between two bunches. The preamplifier amplitude versus input charge is shown for different gain settings in Fig. 64. Mode0 corresponds to "test" mode while all other modes correspond to "physics" mode with different gains. In the test mode, the circuit is linear up to about 300 fC and it saturates for higher input charges. In the physics mode, the linearity range is extended to tens of pC by increasing the feedback capacitance.
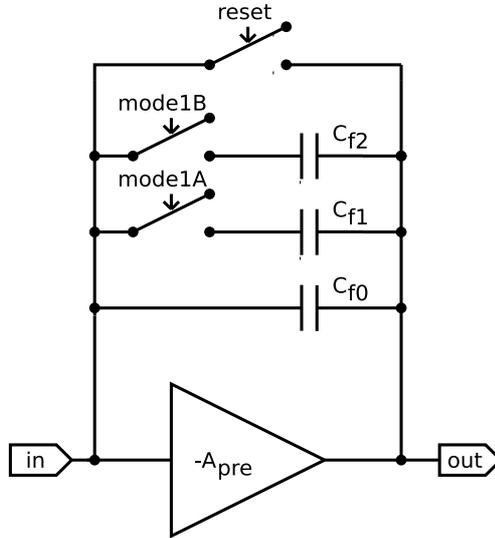
Figure 62: Schematic of preamplifier with reset switch.
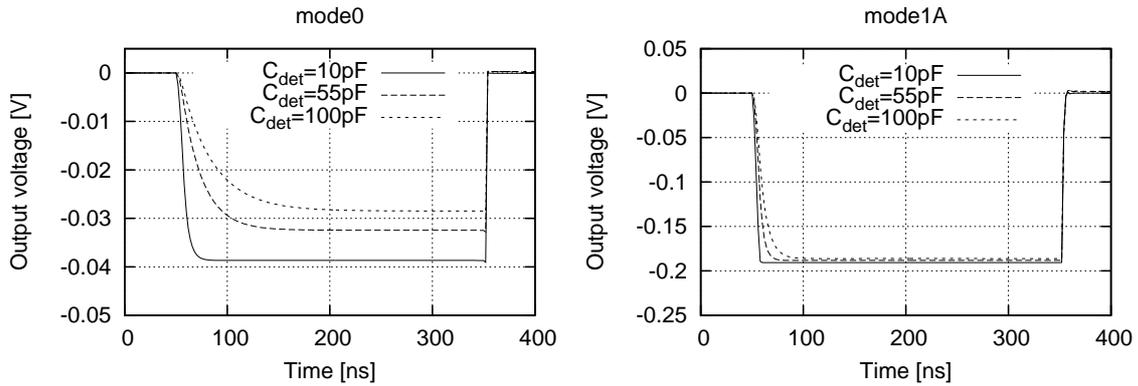
Figure 63: Example of Switched-Reset front-end output in the test mode for 10fC input charge (mode0) and in the physics mode for 1pC input charge (mode1).

8.1.3 Analog to Digital Conversion

Digitization of the signals is done in the ADC and zero suppression block. Simulations of the LumiCal performance indicated that the reconstruction procedure needs about 10 bit precision for the measurement of the deposited energy. Considering the number of needed detector channels and the limitations in area and power, the best choice for the analog to digital conversion seems to be a dedicated multichannel ADC. To save chip area it is useful to have one fast ADC for multiple analog channels. The LumiCal requires a sampling rate of about 3 MHz (per channel), therefore an ADC should sample the data

Figure 64: Example of front-end output amplitude versus input charge.

with at least 24 MHz. One of the most efficient architectures, featuring a good compromise between speed, area and power consumption, is the pipeline type ADC. This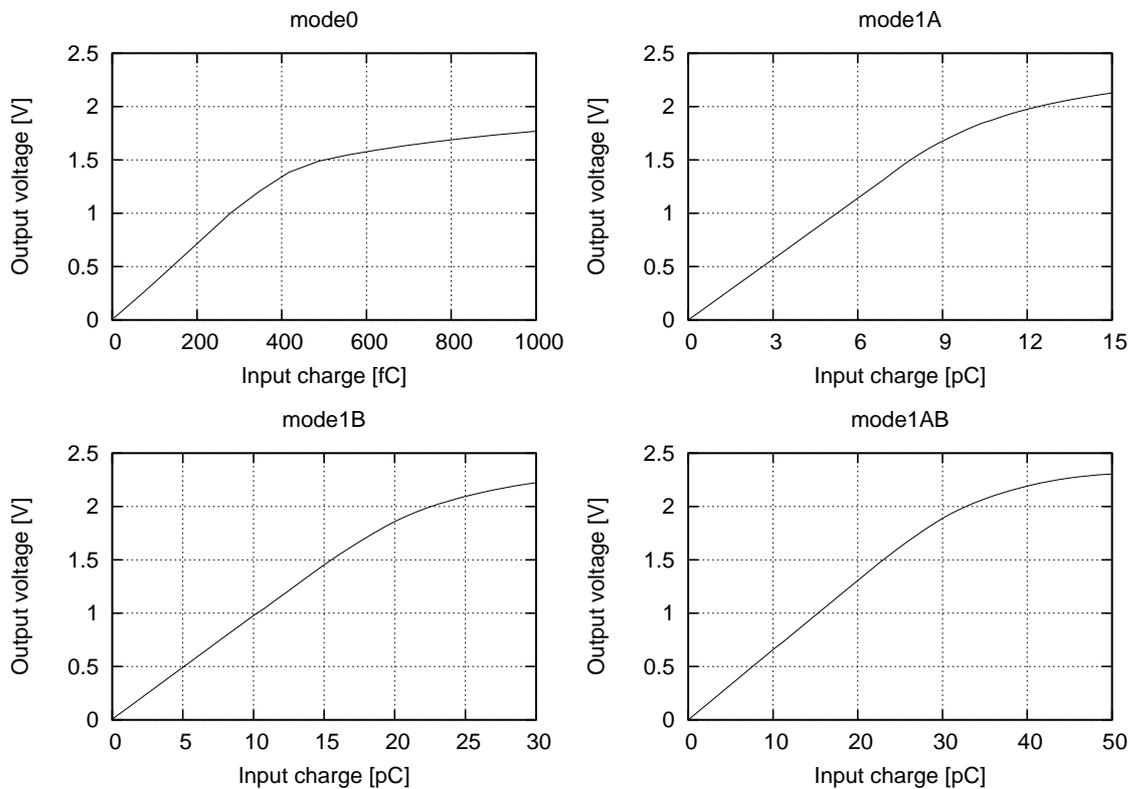 architecture was chosen for the LumiCal data conversion. The implementation of the proposed solution is described together with the simulations below. The part of ADC block responsible for zero suppression is not discussed here since it will be implemented in the next prototyping stage.

ADC Architecture A pipeline type ADC is built of several stages connected in series, as shown in Fig. 65. In the proposed solution, a 1.5 bit per stage architecture was chosen because of its simplicity and its immunity to offsets in the comparator and amplifier circuits. Because a single stage digitizes only three different values and codes them into 2 bits, it is called *1.5 bit stage*. Each stage from Fig. 65 generates 2 bits which are sent to the digital correction block. In the correction block, 18 output bits from 9 stages are combined together resulting in 10 bits of ADC output.

The block diagram of a single stage is shown in Fig. 66. Each 1.5 bit stage consist of two comparators, two capacitors C_s and C_f, an operational transconductance amplifier, several switches and a small digital logic circuit. To improve the ADC immunity to digital crosstalk and other disturbances, a fully differential architecture is used. The stage is operated in
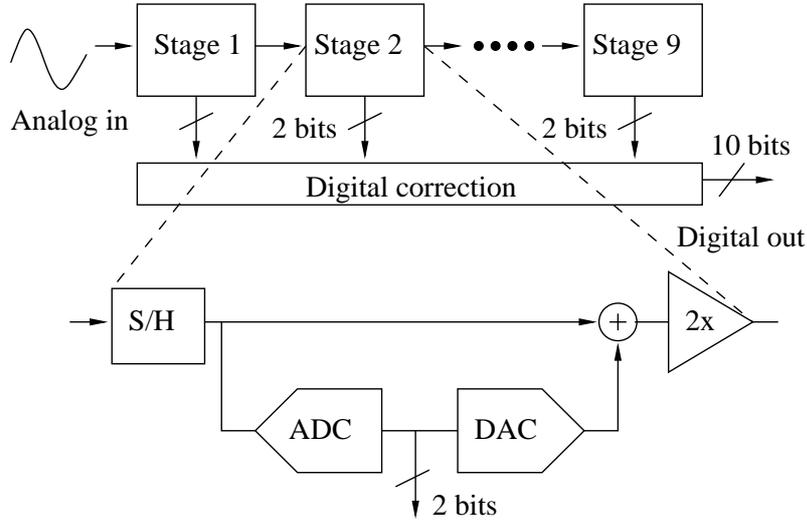
68

Figure 65: Pipeline ADC architecture.

two phases. In phase φ_1, capacitors connected to ground (in reality to a common voltage, ground is used in this description only for simplicity) are charged to the voltages $V_{i\pm}$. In phase φ_2, the switches S_2 and S_3 change their positions and S_1 is open. The capacitors C_f are now in the amplifier feedback loop while the capacitors C_s are connected to the DAC reference voltages ($\pm V_{ref}$ or 0, depending on the comparators decision). In this 1.5 bit/stage architecture, $C_f = C_s$ is chosen to obtain a gain of two in the transfer function.

Simulation Results   The critical block of a pipeline ADC is the fully differential amplifier. A telescopic cascode amplifier configuration is used to fulfill the requirements (speed versus power). To obtain a high enough gain (about 80 dB required for 10 bit resolution), gain boosting amplifiers are used in both, upper and lower cascode branches. Since a 1.5 bit architecture leaves very relaxed requirements on the comparators ($\sim$100mV threshold precision), a simple dynamic latch architecture was chosen. For the present prototype all reference voltages are applied externally. An example of the simulated output of a single 1.5 bit stage for a staircase input is shown in Fig. 67. The output value corresponds to the sum of the input signal and the DAC voltage multiplied by two.

8.1.4   Summary on LumiCal Readout Electronics

The work on the LumiCal readout electronics has just started. The configuration of the principal readout circuits, i.e. the front-end and the ADC, are being simulated and first prototypes are expected soon. In the next iteration, the sub-circuits not yet designed like sample and hold (S/H) or multiplexer (MUX) will be integrated and prototyped as well. Then the integration of multichannel ASICs with all channels and full functionality comprising all necessary controls, DACs, zero suppression etc., will be added. More studies are needed to design the detailed architecture and the implementation of the Data Concentrator
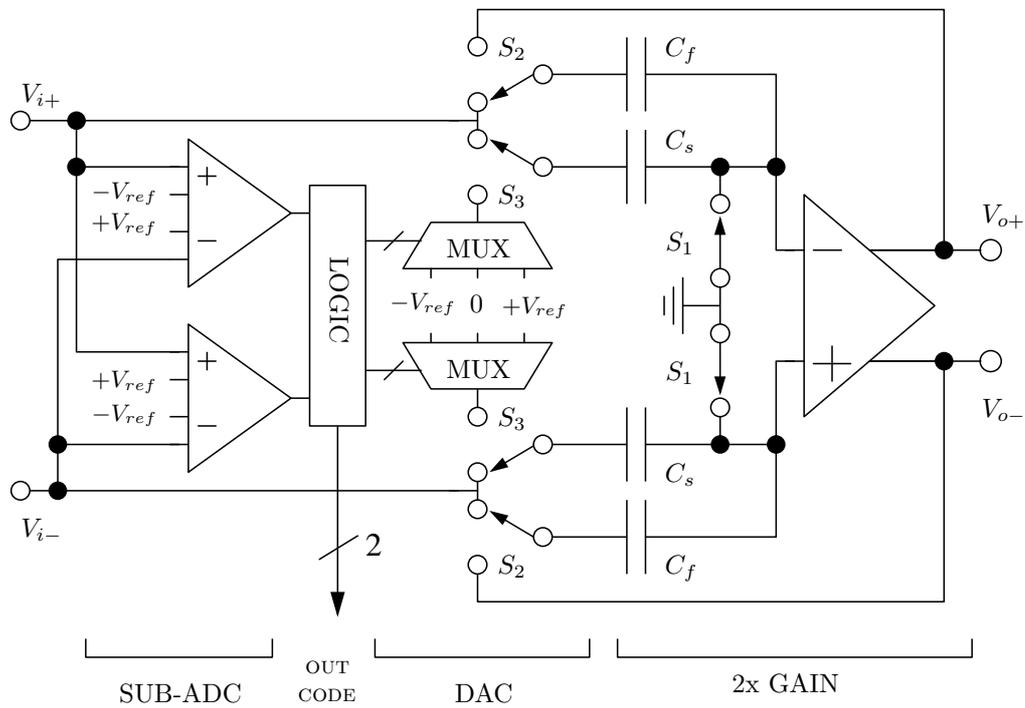
Figure 66: Simplified schematic of a 1.5 bit stage. Switches set to the φ_1 phase.
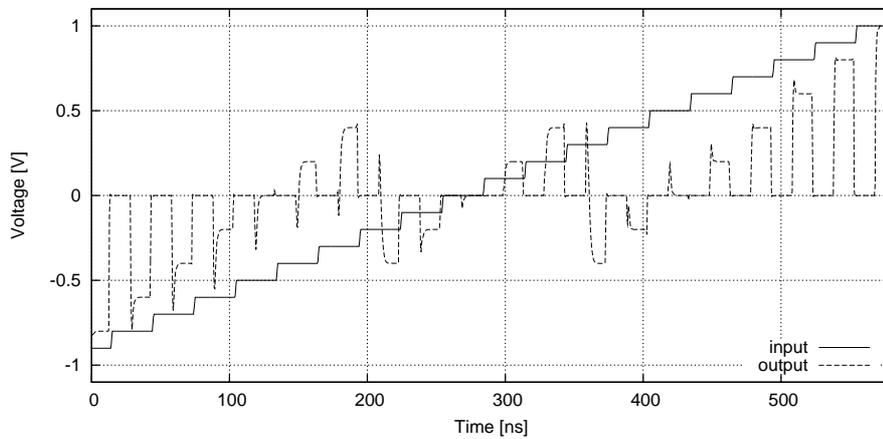

Figure 67: Example of a single 1.5 bit stage output for a staircase function.

and Optical Driver blocks.

8.2 Design of an Architecture for the BeamCal Front-end

The BeamCal has two main functions: physics measurements and beam diagnostics. For physics purposes, signals are captured during each bunch train and then read out between

subsequent trains.

For diagnostics purposes, the BeamCal must provide a fast (maybe low resolution) signal that will help to tune the beams and produce more effective collisions. This signal must be available after every single pulse. The BeamCal instrumentation chip provides the link between the detector pads and the digital output for both, the physics measurement and beam diagnostics. Physics signals must be digitized with 10 bit resolution. They are then read out during the 199 ms period between the bunch trains at 25 Mb/s using LVDS drivers. A total of 855440 10-bit numbers must be read out from each chip between two bunch trains, organized in 32 channels (or 10-bit numbers) for each chip.

The signal for beam diagnostics is a single 8-bit number. It consists of the sum of all signals from the 32 channels in one chip. An enable/disable capability for each channel, as well as gain selection, should be forseen. The signal must be read out after each pulse, with an appropriate short latency.

The BeamCal detector will work in harsh radiation conditions of 2-10 MGy per year, due to the deposition of beamstrahlung remnants. Ideally, the readout chips should be directly connected to the detectors, in order to simplify the electronic design and improve its performance by reducing parasitic capacitances. However, the chips would not survive such a harsh environment. Therefore the chips will be located in a safer position outside the inner radii. In that position, the chips must be able to tolerate a radiation of 1 Mrad (SiO_2) to have an expected lifetime of 10 years. There are different options to design radiation-tolerant chips. Performance tradeoffs connected to the specific design will be included in our study.

Possible BeamCal sensor pads could be 0.55 cm^2 rad-hard silicon photodiodes. Other alternatives based on pCVD diamond or GaAs are currently being studied.

If fully depleted, each silicon sensor will have an approximate capacitance of 20 pF. The charge deposited in each sensor cell by radiation and particles is the sum of background particles and signals from high energetic electrons. The maximum charge will be 40 pC (250 million electrons in Si). This determines the front-end gain for normal operation. The preamplifier must have two important features for calibration purposes: electronics calibration and physics calibration (see above for LumiCal). The electronics calibration uses test pulses. The physics calibration uses known particle signals from the sensors, for example Bhabha pairs collected during physics runs and muons collected during special runs without collisions.

Although the electronic path for both types of calibration is identical, the muon signals have smaller amplitudes than the signals originating from the accelerator operation. Thus the front-end gain for the muon calibration mode must be a factor of 50 larger than for the normal operation mode. This implies a selectable gain and more stringent requirements for the front-end equivalent noise charge (ENC). The power consumption of the readout chip must be minimized and must not exceed 70 mW. Because power consumption depends on the operation mode, the maximum energy per cycle is a better specification, as long as the peak power is kept to a reasonable value. In this case, the energy per cycle is 70 mW × 0.2 s = 14 mJ per 200-millisecond cycle. It is possible that the specification for the number of pulses during the pulse train may be doubled in the future, so the consequences of such a change to the circuit design will be explored.

71

9 Summary

BeamCal and LumiCal are designed as sandwich calorimeters with tungsten disks as absorbers interspersed with pad-structured sensor planes. Detailed Monte-Carlo simulations are done to optimize the structure of the calorimeters and derive requirements on the mechanics and electronics to match the needs from physics. Several topics need more detailed studies to understand the impact on the performance. Examples are a more realistic simulation of the front-end electronics, the impact of Bhabha events on the BeamCal performance or uncertainties in the shower reconstruction of LumiCal.

For GamCal simulation studies need to be completed to develop a mature design. A precise mechanical frame and a sensor position control on the μm level are necessary for LumiCal to match the precision goal for the luminosity measurement. For the mechanics we follow two concepts, one with decoupled sensor and absorber frames and the other with sensor planes glued on the precisely manufactured tungsten disks. In addition, a laser-beam based position monitoring system is developed.

BeamCal and GamCal will be used for beam-tuning and luminosity optimisation. Monte Carlo simulations are ongoing to explore the full potential combining both devices.

Critical issues are radiation-hard sensors for BeamCal and a specialised readout electronics for BeamCal and LumiCal. So far we studied pCVD diamond sensors in an electron beam and measured the response for doses up to 7 MGy. The sensors are still operational after irradiation. The performance degrades smoothly as a function of the absorbed dose. However, there are effects we do not understand, e.g. large sample to sample fluctuations and dependence of the performance on the dose rate. As long as these effects are not controlled we cannot conclude that pCVD diamond is an appropriate sensor material. Hence we extended our studies to sensors made of GaAs and we will also study radiation-hard silicon.

The design of the readout electronics has just started. From simulations, the dynamic range is estimated. Due to the high occupancy of LumiCal and the bunch-by-bunch readout of BeamCal, the front-end chip, including digitisation, must be sufficiently fast. Since the space available is small we would like to avoid cooling, hence the power dissipation must be small. This can be reached only by a pulsed power supply.

The first submission of a front-end chip for LumiCal is just done. The development of a front-end chip for BeamCal based on the KPiX[4] concept is under way.

The milestones for the next three year are:

- more realistic simulation of LumiCal and the study of the impact of Bhabha selection criteria on the luminosity measurement;
- completing the performance studies for BeamCal including additional effects and a realistic readout chain;
- detailed simulations for the design of the GamCal system;
- processing of the first layout of the front-end electronics and performance tests;

---

[4]KPiX is a readout chip developed for the SiD concept.

- design and construction of a full sensor plane for LumiCal and BeamCal for beam tests;

- continuation of the radiation hardness studies of CVD diamond, GaAs and Si sensors in low energy electron beams.

The goal is to be ready for the construction of calorimeter prototypes in 2010.

References

[1] H. Abramowicz et al., *Instrumentation of the Very Forward Region of a Linear Collider Detector*, IEEE transactions of Nuclear Science **51** (2004) 2983.

[2] LDC Working Group,*The LDC Outline Document*, in the current version of v1.3.

[3] *TESLA Technical Design Report*, DESY 2001-011, ECFA 2001-209, March 2001.

[4] SiD Working Group,*The SiD Detector Outline Document*.

[5] S. Riemann, private communication.

[6] G. Altarelli et al., Phys. Lett. **B 349** (1995) 145.

[7] R. Hawkings, K. Mönig, EPJdirect **C 8** (1999) 1.

[8] G. Abbiendi et al., OPAL Collaboration, *Precision luminosity for Z0 lineshape measurements with a silicon-tungsten calorimeter*, Eur. Phys. J. **C 14** (2000) 373.

[9] R. Bonciani, A. Ferroglia, P. Mastrolia, E. Remiddi and J. J. van der Bij, *Two-loop N(F) = 1 QED Bhabha scattering differential cross section*, Nucl. Phys. **B 701** (2004) 121 [arXiv:hep-ph/0405275].

[10] T. Becher and K. Melnikov, *Two-loop QED corrections to Bhabha scattering*, arXiv:0704.3582 [hep-ph].

[11] S. Actis, M. Czakon, J. Gluza and T. Riemann, *Two-Loop Fermionic Corrections to Massive Bhabha Scattering*, arXiv:0704.2400 [hep-ph].

[12] A. A. Penin, *Two-loop photonic corrections to massive Bhabha scattering*, Nucl. Phys. **B 734** (2006) 185 [arXiv:hep-ph/0508127].

[13] M. Czakon, J. Gluza and T. Riemann, *The planar four-point master integrals for massive two-loop Bhabha scattering*, Nucl. Phys. **B 751** (2006) 1 [arXiv:hep-ph/0604101].

[14] S. Jadach, talk given on the FCAL workshop, Cracow 2006, http://xtzeus3.ifj.edu.pl/ galas/fcal/index.html.

[15] L. Suszycki, *LumiCal background studies*, talk given at FCAL Research Workshop of the Israel Science Foundation, Tel Aviv, Israel, 18-22 September, 2005.

[16] J.A.M Vermaseren , Nucl. Phys. **B 229** (1983) 347.

[17] W. Kilian, WHIZARD 1.40, *A Generic Monte Carlo integration and event generation pa ckage for multi-particle processes*, (LC-tool 2002-039).

[18] R. Ingbir, *Luminosity detector design recommendation, talk given at the 4th International Linear Collider Workshop 2005 ECFA Study*, Vienna, Austria, 14-17 November, 2005.

[19] W. Lohmann et al., *Instrumentation of the Very Forward region*, PRC R&D 02/01. Update as of April 18th 2006.

[20] B.Pawlik, *BARBIE Version 4.1, Simulation package of the TESLA luminosity calorimeter*, private communication.

[21] C. Rimbault, *Limitation on precision luminosity measurement from beam-beam effects*, talk given at the European LC Workshop, Daresbury, United Kingdom, January, 2007.

[22] C. Rimbault, P. Bambade, K. Mönig, D. Schulte, EUROTeV-report-2007-017, submitted for publication.

[23] S. Jadach, W. Placzek, E. Richter-Was, B.F.L. Ward, Z. Was, CERN-TH/96-158. UTHEP-96-0601.

[24] D. Schulte, Ph. D. Thesis, University of Hamburg 1996. TESLA-97-08.

[25] International Linear Collider Reference Design Report, first draft, February 2007. http://media.linearcollider.org/rdr_draft_v1.pdf.

[26] G. Abbiendi et al., Eur. Phys. J. **C 14** (2000) 51.

[27] R. Barate et al., Eur. Phys. J. **C 14** (2000) 1.

[28] P. Abreu et al. Eur. Phys J. **C 16** (2000) 371.

[29] M. Acciarri et al. Eur. Phys J. **C 16** (2000) 1.

[30] A. Stahl, *Luminosity Measurement via Bhabha Scattering: Precision Requirements for the Luminosity Calorimeter.*, LC-DET-2005-004, Apr 2005.

[31] K. Mönig, LC-PHSM-2000-60-TESLA.

[32] K. Yokoya, User's Manual of CAIN - Version 2.3, October 2001., http://www-acc-theory.kek.jp/members/cain/default.html.

[33] http://flc.web.lal.in2p3.fr/mdi/BBSIM/bbsim.html.

[34] J. Blocki et al., *A proposal for the mechanical design of the LumiCal detector*, Report No. 1990/PH,IFJ PAN, Cracow,2006, EUDET-Memo-2006-08.

[35] J. Blocki et al., *Silicon sensors for the Lumical for the Very Forward Region*, Report No. 1993/PH, IFJ PAN, Cracow, 2006, EUDET-Memo-2007-09.

[36] S.Jadach, W. Placzek, E. Richter-Was, B.F.L. Ward and Z.Was, BHLUMI, *A Monte Carlo Event Generator for BhaBha Scattering at Small Angles*, Version 4.04.

[37] H. Abramowicz, R. Ingbir, S. Kananov, A. Levy, *A Luminosity detector for the ILC*, ILC note, PREL-LC-DET-2007-003.

[38] B. Pawlik, private communication.

[39] H. Abramowicz, R. Ingbir, S. Kananov, A. Levy, I. Sadeh, *Constraints on the electronics readout for the luminosity detector of the international linear collider*, ILC note in preperation.

[40] J. Blocki et al., *Laser measurement of the LumiCal detector displacement*, Report No. 1983/PH, IFJ PAN, Cracow 2006, EUDET-Memo-2006-05.

[41] W. Wierba, J. Zachorowski, K. Oliwa, *Laser measurement of the LAT detector displacement*, Report No. 1391/PH, IFJ PAN, Cracow, 2003.

[42] W. Wierba, J. Zachorowski, *LAT detector alignment*, talk given at the Collaboration Meeting "R&D for the TESLA-Detector: Instrumentation of the Very Forward Region", ECFA/DESY workshop, Amsterdam, April, 2003, Holland.

[43] W. Wierba, W. Slominski, J. Zachorowski, *Laser measurement of the LAT detector displacement*, FCAL Workshop, Prague, April, 2004, Czech Rep.

[44] W. Wierba, K. Oliwa, W. Slominski, J. Zachorowski, L. Zawiejski, *LumiCal displacement measurement-present status*, FCAL Workshop, Tel-Aviv, September, 2005, Israel.

[45] W. Wierba, M. Karbowiak, K. Oliwa, W. Slominski, J. Zachorowski, L. Zawiejski, *LumiCal displacement measurement - present status*, FCAL Collaboration meeting, IFJ PAN, Cracow, February, 2006, Poland.

[46] M. Battaglia et al., Eur.Phys.J **C 33** (2004) 273.

[47] P. Bambade et al., *Experimental implications for a linear collider of the SUSY dark matter scenario*, talk given at International Conference on Linear Colliders (LCWS04), Paris France, April 2004.

[48] T. Raubenheimer et al., *Suggested ILC Beam Parameter Ranged*, available at http://www-project.slac.stanford.edu/ilc/acceldev/beamparameters.html.

[49] L. Hendrikson et al., *Luminosity Optimization Feedback in the SLC*, ICALEPCS Conf. (1997).

[50] A. Stahl, *Diagnostics of Colliding Bunches from Pair Production and Beam Strahlung at the IP*, LC-DET-2005-003.

[51] T. Tauchi and K. Yokoya, *Nanometer-beam-size measurement during collisions at linear colliders*, Phys. Rev. E 51, 6119-6126 (1995).

[52] B. Parker and A. Seryi, *Compensation of the effects of a detector solenoid on the vertical beam orbit in a linear collider*, Phys. Rev. ST Accel. Beams 8, 041001 (2005).

[53] S. Agostinelli et al. [GEANT4 Collaboration],*GEANT4: A SIMULATION TOOLKIT*, Nucl. Instrum. Meth. **A 506** (2003) 250.

[54] F.A. Berends, P.H. Daverveldt, R. Kleiss, Comp. Phys. Comm **40** (1986) 271, 285, 309.

[55] D. Karlen e al., Phys. Rev. **D 39** (1989) 1861.

[56] M. Ohlerich et al., to be submitted to Phys. Rev. Special Topics Acc. and Beams.

[57] http://www-zeuthen.desy.de/ILC/fcal/.

[58] C. Grah, BeamCal talk, ILC Workshop Valencia, Spain, November, 2006.

[59] W. Morse, GamCal talk, ILC Workshop Vancouver, Canada, July, 2006.

[60] G. Bonivicini et al., *First Observation of Beamstrahlung*, Phys. Rev. Lett.**62** (1989) 2381.

[61] W.Morse, *Gamma Beam-strahlung Spectrometer Backgrounds*, FCAL internal note (2007).

[62] C. Grah *et al.*, *Polycrystalline CVD Diamonds for the Beam Calorimeter of the ILC*, Proceedings of the Nuclear Science Symposium 2006, Oct-Nov 2006, San Diego, California.